NATIONAL UNIVERSITY OF IRELAND, CORK

Radiative Signatures of the Jet Launching Region in Astronomical Objects

by

Michael O' Riordan

A thesis submitted in partial fulfillment for the degree of Doctor of Philosophy

in the Department of Physics, Faculty of Science

Supervisor: Dr. Asaf Pe'er

Head of Department: Prof. John McInerney

January 2018

Contents

Declaration of Authorship

This is to certify that the work I am submitting is my own and has not been submitted for another degree, either at University College Cork or elsewhere. All external references and sources are clearly acknowledged and identified within the contents. I have read and understood the regulations of University College Cork concerning plagiarism.

Signed: _____

Date: _____

Abstract

Relativistic jets are observed in a wide range of accreting black hole systems, from stellar-mass black holes in X-ray binaries (XRBs), to supermassive black holes in active galactic nuclei (AGN). However, despite decades of observational and theoretical research, the mechanism by which relativistic jets are launched in nature remains one of the most important unanswered questions in high-energy astrophysics. In this thesis, we investigate various aspects of jet launching by calculating the radiative properties of the inner accretion flow and jet launching region in a range of low-luminosity accreting black hole systems. We treat the plasma dynamics using sophisticated general-relativistic magnetohydrodynamic simulations, and calculate the resulting spectral and temporal radiative signatures using a general-relativistic radiative transport code. In chapter 3, we investigate the high-energy signatures of jets from the inner regions of XRBs, a question which remains an issue when interpreting X-ray observations. We calculate the observational effects of black hole spin in chapter 4, since it is widely expected that black hole spin plays a key role in the process of jet launching. An important unsolved problem in high-energy astrophysics is the origin of variability in blazars (AGN with jets pointing towards us). In chapter 5, we investigate the source of this variability in terms of turbulence in the jet launching region. Finally, in chapter 6 we investigate the observational effects of the mass-loading of jets. Understanding the mass-loading process is crucial for comparing models of jet launching with observations, since the properties of the jet plasma determine the radiative signatures.

Acknowledgements

First and foremost, I would like to thank my supervisor Asaf Pe'er for his guidance, insight, patience, and advice over the past four years, and for sparking my interest in general relativity and high-energy astrophysics. Thanks also to Jonathan McKinney for his mentorship, and for sharing his vast knowledge of GRMHD and numerical simulations. I would like to thank Frank Peters, Paul Callanan, Denise Gabuzda, and David Rea for their help and support throughout my undergraduate and postgraduate studies in UCC. Special thanks also to my examiners Paul Callanan, and Nick Kylafis. Huge thanks to the physics post-grads: Anthony, Mark, Danny, Bryan, Joe, and Declan, for both physics and non-physics fun. Thank you to my parents, Majella and John, whose love, support, and encouragement have seen me through the past 4 years, as well as the 23 before that. And to the rest of my family: Aisling, Johnny, Orla, Lily, and Justin, thanks for everything. Finally, to Jess, thank you so much for being with me through all of this. I couldn't have done it without you.

List of Publications

This thesis is based on the following publications, which are ordered by appearance.

- **O' Riordan, M.**, Pe'er, A., & McKinney, J. C., "*Jet Signatures in the Spectra of Accreting Black Holes*", 2016, ApJ, 819, 95

- **O' Riordan, M.**, Pe'er, A., & McKinney, J. C., "*Effects of Spin on High-Energy Radiation from Accreting Black Holes*", 2016, ApJ, 831, 62

- **O' Riordan, M.**, Pe'er, A., & McKinney, J. C., "*Blazar Variability From Turbulence in Jets Launched by Magnetically Arrested Accretion Flows*", 2017, ApJ, 843, 81

- **O' Riordan, M.**, Pe'er, A., & McKinney, J. C., "*Observational Signatures of Mass-Loading in Jets Launched by Rotating Black Holes*", 2018, ApJ, 853, 44

Chapter 1

Introduction

Relativistic jets are collimated outflows of plasma, associated with accretion onto compact objects such as neutron stars and black holes. They are among the most fundamental and yet mysterious phenomena in astrophysics today. Jets are ubiquitous in accreting black hole systems, spanning more than 8 orders of magnitude in mass, from stellar-mass systems such as X-ray binaries (XRBs), gamma-ray bursts (GRBs), and tidal-disruption events (TDEs) to supermassive black holes in active galactic nuclei (AGN). In this chapter, we briefly review the observational properties of a range of accreting black hole systems considered in this thesis. We also outline various approaches and limitations of the theoretical modelling of these systems. Finally, we describe the structure of the thesis and mention our main findings.

1.1 Phenomenology of Jets and Accreting Black Hole Systems

Observationally, radio emission has been the primary radiative signature associated with the existence of relativistic jets from accreting black hole systems (see e.g., Romero et al., 2017, for a recent review). In particular, jet-dominated AGN are classified as "radio-loud" while jets are weak or absent in "radio-quiet"

AGN. Furthermore, XRBs show distinct radio-load and radio-quiet states which are believed to be associated with the launching and quenching of jets (see e.g., Remillard & McClintock, 2006; Fender, 2010; Corbel, 2011; Fender & Gallo, 2014, and references therein).

1.1.1 X-ray Binaries

In XRBs, these jet- and disk-dominated states are more commonly classified by their X-ray luminosity and X-ray spectral hardness (often defined to be the ratio of the flux at 6.3–10.5 keV to the flux at 3.8–6.3 keV; Fender et al., 2004; Belloni et al., 2005). XRBs spend most of their time in the so-called low/hard state, with an X-ray spectral hardness of order unity (Remillard & McClintock, 2006). At very low luminosities, this state is also referred to as the quiescent state. The weakest observed sources have an X-ray luminosity of $L_X \sim 10^{-8} L_{\rm Edd}$ in quiescence (e.g., Romero et al., 2017), where $L_{\rm Edd}$ is the Eddington luminosity given by

$$L_{\rm Edd} = 1.26 \times 10^{38} \left(\frac{M}{M_\odot} \right) \text{erg s}^{-1} \tag{1.1}$$

Here, M is the mass of the black hole and $M_\odot$ is the mass of the Sun. The low/hard state is associated with the existence of compact, quasi-steady jets. The radio synchrotron emission from the jet is self-absorbed, with a flat/inverted spectrum also observed in the cores of AGN (Blandford & Konigl, 1979).

XRBs exhibit outbursts in which they transition from the low/hard state to the so-called high/soft state and back again. Typical cycles last from months to roughly a year. Although the precise mechanism remains unknown, this transition is believed to be associated with changes in the accretion rate of the flow. In particular, it is expected that the X-ray luminosity tracks the accretion rate (e.g., Fender, 2010). During outburst, the X-ray luminosity increases and the system rises out of quiescence. Once the luminosity reaches approximately $L_X \sim 0.5\, L_{\rm Edd}$, the X-ray spectrum softens and the system transitions to the high/soft state (e.g., Romero et al., 2017). During this transition (the so-called intermediate state), the

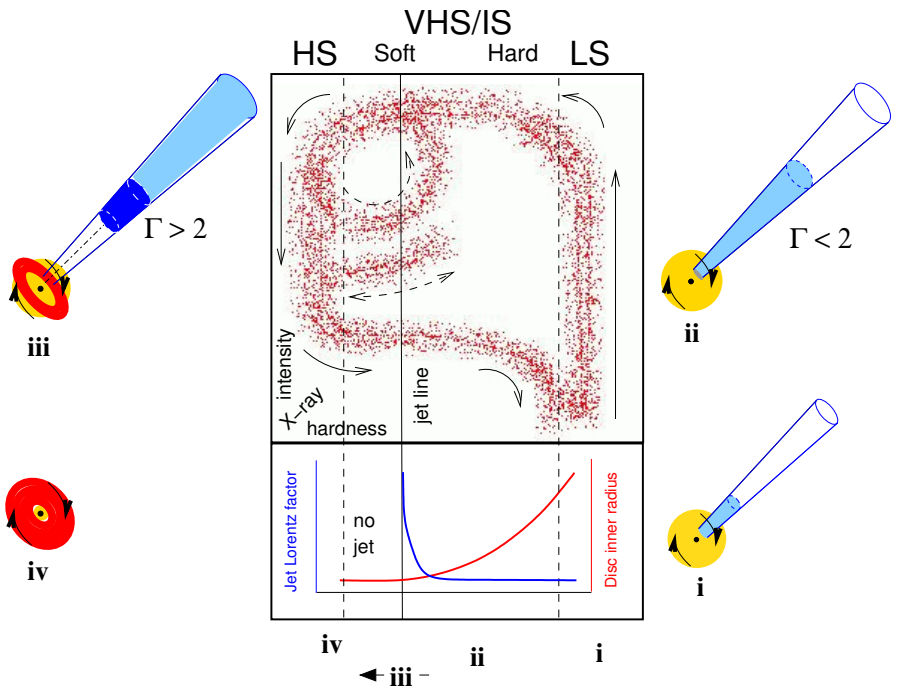

FIGURE 1.1: A schematic representation of the XRB states presented by Fender et al. (2004). The central panel shows a hardness-intensity diagram (HID), where the x-axis represents the X-ray spectral hardness, and the y-axis is the X-ray luminosity. "HS" labels the high/soft state, "VHS/IS" labels the very high/intermediate state, and "LS" labels the low/hard state. The arrows show the track taken during a typical outburst, however note that other more complicated tracks are also observed. The bottom panel shows the jet bulk Lorentz factor as a function of the X-ray hardness. The diagrams around the plot represent the behaviour of the jet in the different states. There is an increase in luminosity from states (i) to (ii). In state (iii) the jet is composed of discrete, relativistic blobs, while in state (iv) the jet is absent and the emission is dominated by the disk.

jet changes from a compact steady flow, to a series of discrete/transient, optically thin blobs which often undergo superluminal motion. Once in the high/soft state, the jet is essentially absent. The radio synchrotron emission vanishes and the spectrum is well described as a multi-colour blackbody, dominated by thermal emission from the accretion disk. As the luminosity decreases once again, the X-ray spectrum becomes harder and the system returns to the low/hard state. In Figure 1.1 we show a schematic representation of this process (from Fender et al., 2004).

Although it is widely accepted that jets are responsible for the radio emission observed both in AGN and during the low/hard state in XRBs, the role of jets in

producing the high-energy emission in these systems is still debated. In particular, there is no consensus regarding the origin of the X-ray component in the low/hard state. It has long been argued that inverse Compton emission from a corona of hot electrons surrounding the inner accretion disk can produce the observed X-ray spectrum (e.g., Titarchuk, 1994; Magdziarz & Zdziarski, 1995; Gierlinski et al., 1997; Esin et al., 1997, 2001; Poutanen, 1998; Cadolle Bel et al., 2006; Yuan et al., 2007; Narayan & McClintock, 2008; Niedźwiecki et al., 2012, 2014; Qiao & Liu, 2015). While X-rays are expected from the inner disk/corona, it is also possible that a significant fraction of the X-ray emission originates in jets (e.g., Mirabel & Rodríguez, 1994; Markoff et al., 2001, 2003, 2005; Falcke et al., 2004; Bosch-Ramon et al., 2006; Kaiser, 2006; Gupta et al., 2006; Kylafis et al., 2008; Maitra et al., 2009; Pe'er & Casella, 2009; Pe'er & Markoff, 2012; Markoff et al., 2015; O' Riordan et al., 2016a). This latter view has largely been motivated by the observed correlation between the radio and X-rays in the low/hard state (Corbel et al., 2000, 2003; Gallo et al., 2003). The relative importance of the disk and jet in generating the X-rays is still the subject of active research. Breaking this degeneracy is important for developing an understanding of jets and of the disk-jet connection in XRBs and other sources. We return to this issue in chapter 3.

1.1.2 Sgr A*

Sgr A* is an extremely low-luminosity, compact source of radio, infra-red (IR), and X-rays associated with a $4 \times 10^6 M_\odot$ (Gillessen et al., 2009) accreting supermassive black hole at the centre of our Galaxy. There is a clear similarity with the quiescent state in XRBs; the luminosity at millimeter (mm) wavelengths is $\lesssim 10^{-8} L_{\rm Edd}$, with a flat/inverted, self-absorbed radio spectrum. Although there is no unambiguous evidence for the existence of jets in Sgr A*, the radio spectrum has been well-fit by emission from a compact jet "sheath" (e.g., Mościbrodzka et al., 2009; Mościbrodzka & Falcke, 2013; Mościbrodzka et al., 2014). We investigate the contribution of jets to the emission in Sgr A* in chapter 6.

The emission from Sgr A* in the optical and UV bands is heavily obscured due to absorption by Galactic dust. The X-ray luminosity in the 2–8 keV band was measured by *Chandra* to be approximately $\sim 10^{33}\,\mathrm{erg\ s^{-1}}$ (Baganoff et al., 2003). However, the X-ray emission is only resolved on spatial scales of roughly $10^5\,r_g$, where $r_g = GM/c^2$ is the gravitational radius. The contribution from the inner accretion flow is unresolved, and is estimated to be up to $\sim 10\%$ of the resolved emission (Neilsen et al., 2013).

Although Sgr A* is relativity small for a supermassive black hole, it has the largest angular size ($\sim 10\,\mu$as) among all black holes discovered to date. Because of this, it is a very promising target for very-long baseline interferometric (VLBI) observations with the Event Horizon Telescope (EHT; Doeleman et al., 2009a). The EHT is expected to resolve structure in Sgr A* on spatial scales comparable to the Schwarzschild radius $r_S = 2\,r_g$ next year. Furthermore, it will be able to resolve small-scale polarized structure, which carries information about the near-horizon magnetic field. Therefore, despite its low-luminosity and small black hole mass, Sgr A* offers an unprecedented opportunity to test theories of accretion and jet-launching, and possibly even general relativity itself via measurements of the black hole shadow (e.g., Psaltis et al., 2015, and references therein).

1.1.3 Blazars

In contrast to Sgr A*, blazars are extremely luminous AGN. It is generally accepted that blazars have relativistic jets aligned close to our line of sight (e.g., Urry & Padovani, 1995). Broadly speaking, blazars can be classified into two main categories: low-luminosity BL Lacs and high-luminosity flat-spectrum radio quasars (FSRQs), forming the so-called "blazar sequence" (Fossati et al., 1998; Ghisellini et al., 2017). These objects are variable at all observed wavelengths from radio to γ-rays (e.g., Ulrich et al., 1997). In particular, the γ-ray lightcurves show variability on timescales ranging from minutes to years. This variability can be characterized as having a power density spectrum (PDS) of power-law shape, spanning the entire observed frequency range. The power law index is remarkably

similar for both BL Lacs and FSRQs. Abdo et al. (2010) report a PDS slope of 1.4 ± 0.1 for 9 bright FSRQs, as well as slopes of 1.7 ± 0.3 and 1.5 ± 0.2 for 6 BL Lacs and 13 faint FSRQs, respectively. Recently, Ackermann et al. (2016) report a slope of 1.24 ± 0.15 in the case of the FSRQ 3C 279, and Goyal et al. (2017) report a slope of 1.1 ± 0.2 for the BL Lac object PKS 0735+178. Max-Moerbeck et al. (2014) provide estimates of the γ-ray PDS slopes for 29 blazars, using simulated lightcurves to properly account for noise processes. Their findings are largely consistent with the results of Abdo et al. (2010). A similar analysis was performed by Ramakrishnan et al. (2015) for a sample of 55 blazars from the first 5 years of *Fermi*/LAT data. They find average slopes of 1.3 and 1.1 obtained from 35 FSRQs and 12 BL Lacs, respectively. These slopes are somewhat smaller than those reported by Abdo et al. (2010), however, the slopes reported for 3C 279 are consistent in both cases.

The radio emission, resolved at large radii, clearly originates in jets. Apparent superluminal motion provides compelling evidence that the radio emitting matter propagates with relativistic velocities (e.g., Urry & Padovani, 1995). Since the γ-rays are unresolved, however, the source of high-energy emission is uncertain and could potentially be located much closer to the central supermassive black hole (e.g., Pe'er & Markoff, 2012). Generally speaking, the observed short timescale variability implies a compact emission region. While such a compact region close to the black hole might be responsible for variability in low-luminosity systems, high-luminosity systems (such as 3C 279) require a significant Lorentz factor to overcome the pair opacity which would otherwise prevent γ-rays from escaping to infinity (see e.g., appendix A and Dondi & Ghisellini, 1995). The location of the γ-ray emission zone remains a topic of active research (e.g., Madejski & Sikora, 2016, for a recent review).

The shortest variability timescales are comparable to, and in some cases shorter than, the light-crossing time of the black hole (Aharonian et al., 2007; Albert et al., 2007; Aleksić et al., 2011; Ackermann et al., 2016). For example, Aharonian et al. (2007) observed variability on a timescale of $t_{\rm var} \approx 200s$ during a flare in PKS 2155–304. This is more than an order of magnitude shorter than

the corresponding light-crossing time, inferred by the empirical relation between galactic bulge luminosity and black hole mass (Bettoni et al., 2003; Aharonian et al., 2007). The mechanism responsible for this fast variability is poorly understood. Popular models include the "jets in a jet" model (Giannios et al., 2009), in which magnetic reconnection in highly-magnetized regions of the jet accelerates compact blobs of plasma to relativistic velocities in the bulk jet frame; the magnetospheric acceleration model (Levinson & Rieger, 2011), in which charged particles are accelerated by unscreened electric fields in a charge starved vacuum gap of the black hole magnetosphere; the relativistic turbulence model (Narayan & Piran, 2012), in which magnetohydrodynamic turbulence in the jet produces compact blobs on scales smaller than the horizon radius, similar to those in the "jets in a jet" scenario; and the jet-star interaction model (Barkov et al., 2012) in which stars cross the jet close to the black hole. We investigate the question of blazar variability in chapter 5.

1.2 Theoretical Modelling of Jets and Accreting Black Hole Systems

While radio observations provide a wealth of evidence for the existence of jets in AGN and XRBs, there is little direct evidence of the conditions required for jets to form at all.

1.2.1 Jet Launching

The fact that jets exist in such a wide range of systems has led to the suggestion that their creation and dynamics should be governed by ingredients common to these systems. In this thesis, we restrict our attention to jets from black hole systems, although jets have also been observed from other accreting sources such as neutron stars and proto-stellar objects. In the black hole case, models of jet

launching involve accreting plasma, magnetic fields, and the extraction of rotational energy either from a black hole (Blandford & Znajek, 1977), or from the accretion disk itself (Blandford & Payne, 1982). The basic idea is that magnetic field lines, anchored in the accretion flow, are twisted either by rotation of the disk or by frame dragging in the vicinity of a rotating black hole. These field lines expand under their own pressure, transporting energy outwards and accelerating any "frozen-in" plasma into jets aligned with the axis of rotation.

Narayan & McClintock (2012) aimed to test if the transient jets launched during state transitions in XRBs are powered by black holes. As mentioned previously, state transitions occur at a well defined value of the X-ray luminosity $L_X/L_{\rm Edd} \approx 0.5$. Since L_X is expected to track properties of the accretion flow such as the mass accretion rate, this makes transient jets better "standard candles" than the steady jets in the low/hard state, which occur over a wide range of luminosities. Then, assuming that some source-independent fraction of the jet power is radiated at 5GHz, Narayan & McClintock (2012) argued that this flux can be used as a proxy for the transient jet power. They found a correlation between the 5GHz radio emission during state transitions in XRBs and black hole spin, and interpreted this as evidence for a relationship between jet power and spin (but see Fender et al., 2010; Russell et al., 2013). Interestingly, their results were consistent with $P_{\rm jet} \sim a^2$, which is the scaling derived by Blandford & Znajek (1977) for slowly rotating black holes. They also found good agreement with the more accurate scaling $P_{\rm jet} \sim \Omega_H^2$ (Tchekhovskoy et al., 2010, 2012), which works up to $a \approx 0.95$. Here, a is the dimensionless spin of the black hole, $\Omega_H = a/2\,r_H$ is the angular velocity of the horizon, and $r_H = 1+\sqrt{1-a^2}$ is the horizon radius (in units where $r_g = GM/c^2 = 1$). If confirmed, this correlation provides observational evidence that jets are probably powered by the rotational energy of black holes.

Although the Blandford-Payne (BP; Blandford & Payne, 1982) mechanism may also operate to power outflows, it is unclear whether this process can produce highly-collimated, relativistic jets, which are observed in a wide range of sources. In particular, in numerical simulations the BP mechanism typically results in uncollimated, mildly-relativistic disk winds rather than jets (e.g., McKinney &

Blandford, 2009), while the Blandford-Znajek (BZ) mechanism can produce powerful, collimated outflows (Tchekhovskoy et al., 2011; McKinney et al., 2012). Therefore, throughout this thesis, we consider models of accreting plasma in which the BZ mechanism operates to extract energy from the black hole. We provide a brief derivation of the BZ mechanism in section 2.3, and consider the high-energy signatures of this process in chapter 4.

1.2.2 Accretion Models

Conservation of energy in accretion flows can be written simply as (e.g., Narayan & McClintock, 2008)

$$Q_+ = Q_- + Q_{\rm adv} \tag{1.2}$$

This states that the rate at which heat energy is released by viscous dissipation in the flow Q_+, equals the rate at which energy is lost by radiative cooling Q_-, plus the rate at which energy is advected with the flow $Q_{\rm adv}$. The standard "thin disk" model (Shakura & Sunyaev, 1973; Novikov & Thorne, 1973) corresponds to the case where the flow is radiatively efficient with $Q_- \gg Q_{\rm adv}$. In this case, the disk radiates approximately a tenth of its rest mass energy $L \sim 0.1\,\dot{M}c^2$, the sound speed is much less than the Keplerian speed v_K, and the disk is geometrically thin.

Livio et al. (1999) argued that the BZ mechanism will not operate efficiently in standard thin disks due to the fact that the magnetic flux at the horizon can not be significantly larger than that of the inner disk. A different class of accretion flow models, which readily advect magnetic fields towards the black hole, are the so-called "advection-dominated accretion flows" (ADAFs) (Narayan & Yi, 1994, 1995a,b; Abramowicz et al., 1995; Narayan & McClintock, 2008; Yuan & Narayan, 2014). In contrast to thin disks, ADAFs are geometrically thick and have $Q_{\rm adv} \gg Q_-$. They are also much less luminous than thin disks, with $L \ll 0.1\,\dot{M}c^2$. Avara et al. (2016), with the inclusion of results from McKinney et al. (2012), showed that the BZ mechanism produces much more powerful jets in ADAFs than in

standard thin disks. Therefore, in the rest of this thesis we restrict our attention to ADAFs.

Radiatively inefficient accretion flows (RIAFs), by definition, are flows for which the cooling time of a fluid element is much longer than the time required for the fluid element to be accreted onto the black hole. In this thesis, we deal exclusively with radiatively inefficient ADAFs and will simply refer to these in what follows as RIAFs. RIAFs have been used extensively to model low luminosity systems such as Sgr A* and the low/hard state in XRBs (see e.g., Narayan & McClintock, 2008; Yuan & Narayan, 2014). Here, low luminosity simply means that $L \ll L_{\rm Edd}$. These flows are geometrically thick, optically thin, and collisionless. Due to the fact that the electrons and ions are collisionally decoupled, they are likely to be at different temperatures, although the details of the electron thermodynamics in these systems are still being developed (Ressler et al., 2015). We discuss our approach for treating the radiating electrons in section 2.4.3.

As mentioned previously, efficient jet launching by the BZ process is only possible if enough ordered vertical magnetic flux can accumulate near the horizon. The BZ model predicts that energy is extracted from the black hole at a rate $P_{\rm BZ} = \kappa\, \Phi^2\, \Omega_{\rm H}^2\, /4\pi c$ (Blandford & Znajek, 1977; Tchekhovskoy et al., 2010). Here, κ is a dimensionless number which depends on the magnetic field geometry, and Φ is the magnetic flux threading the horizon. The expected BZ jet power therefore depends strongly on the black hole spin, as well as the properties of the near-horizon magnetic field. Narayan et al. (2003) predicted that, if the accretion flow drags in a strong poloidal magnetic field to the black hole, the magnetic pressure could become comparable to the gas pressure and disrupt further axisymmetric accretion. They suggested that such a "magnetically arrested disk" (MAD) could be very efficient at converting the rest-mass energy of the fluid into heat, radiation, and mechanical/magnetic energy. Recent work by Tchekhovskoy et al. (2011); McKinney et al. (2012) showed that the BZ mechanism can efficiently power relativistic jets in MAD RIAFs. By contrast, non-MAD flows (called SANE by Narayan et al., 2012) typically do not show very efficient energy extraction, even at high black hole spin, due to the turbulent, disordered fields at the horizon

(McKinney & Blandford, 2009). In recent years, both MAD and SANE RIAFs have been used extensively to model low-luminosity systems such as Sgr A* (Mościbrodzka et al., 2009; Shcherbakov et al., 2012; Mościbrodzka & Falcke, 2013; Mościbrodzka et al., 2014; Chan et al., 2015b,a; Ball et al., 2016; Ressler et al., 2017; Gold et al., 2017). In the following chapters, we consider both MAD and SANE RIAFs, however we usually drop the term "RIAF" since we do not consider any radiately efficient flows.

1.2.3 Numerical Simulations

The equations of general-relativistic magnetohydrodynamics (GRMHD) describe accreting systems in which the radiation is dynamically unimportant (i.e. RIAFs). We review the ideal GRMHD equations in section 2.2. In the past decade, global GRMHD simulations (Gammie et al., 2003; McKinney & Gammie, 2004) have greatly improved our understanding of accretion physics and jet launching. While these GRMHD simulations give much information about the fluid dynamics and possible jet launching mechanisms, the results can not be directly tested by comparing with observational data. To bridge this gap between theory and observations, in recent years, there has been wide interest in adding radiation to these simulations. Including radiation is necessary both for calculating the observational signatures, and for extending the simulations to regimes where the radiation becomes dynamically important i.e., where $L \gtrsim 10^{-4} L_{\rm Edd}$ (Dibi et al., 2012; Ryan et al., 2017). Broadly speaking, there are two main approaches to treating the radiation. The first involves evolving the radiation field self-consistently with the matter, and is mainly used to calculate the effects of radiation on the fluid dynamics. This approach is employed in the general relativistic radiation magnetohydrodynamics codes `KORAL` (Sądowski et al., 2013), `HARMRAD` (McKinney et al., 2014), and `bhlight` (Ryan et al., 2015). `KORAL` and `HARMRAD` treat the radiation as a separate fluid and close the fluid equations using the M1 closure (Levermore, 1984), in which the radiation field is assumed to be isotropic in some frame (not necessarily the fluid frame). This approach is formally accurate at high optical

depths, however fails to capture the frequency dependence required for Compton scattering, and the angular dependence expected at lower optical depths. These codes are therefore optimized for dealing with super-Eddington systems such as ultra-luminous X-ray sources (Sądowski et al., 2013; McKinney et al., 2014, 2015; Sądowski & Narayan, 2015; Narayan et al., 2017). `bhlight` solves the GRMHD equations using a direct Monte Carlo solution of the radiative transport equation. This approach has the advantage that the frequency and angular dependences of the radiation field can be included, however, since it involves tracking photons individually, it is limited to a regime in which radiative effects play a sub-dominant but non-negligible role on the dynamics. `bhlight` has been optimized for calculating the effects of radiation on the dynamical evolution, and so the spectral resolution at low and high frequencies (which have little effect on the dynamics) is limited.

The second method involves calculating the radiation field in a post-processing step, using the fluid data as input. Examples of general-relativistic radiative transport codes which employ a post-processing approach include `grmonty` (Dolence et al., 2009), `ASTRORAY` (Shcherbakov & Huang, 2011), `GRay` (Chan et al., 2013), and `HEROIC` (Zhu et al., 2015; Narayan et al., 2016). Since the fluid data is supplied by an external code, the post-processing algorithms can be optimized for calculating spectra and images. The disadvantage of this approach is that it is only applicable in regimes in which the radiation is dynamically unimportant. These codes have been used by many authors to calculate the observational signatures of low luminosity systems in which the radiation pressure can be neglected (e.g., Mościbrodzka et al., 2009; Mościbrodzka & Falcke, 2013; Mościbrodzka et al., 2014; Chan et al., 2009, 2015b,a; Shcherbakov et al., 2012; Shcherbakov & McKinney, 2013). These works mainly focussed on reproducing the spectra and variability properties of Sgr A*, and place important constraints on quantities such as the black hole spin, proton-to-electron temperature ratio, and inclination angle. The constraints placed on the proton-to-electron temperature ratio could also be relevant for the low/hard state in XRBs.

In this thesis, we use a similar post-processing approach for treating the radiation, with a radiative transport code based on the freely available `grmonty` (Dolence et al., 2009). We assume that energetic electrons (leptons) are responsible for the observed emission. While this is the assumption used by most works, it is also possible that hadronic models (Mannheim & Biermann, 1992; Aharonian, 2000; Mücke & Protheroe, 2001; Mücke et al., 2003; Romero et al., 2003; Bosch-Ramon et al., 2005), in which the protons are accelerated to ultrarelativistic energies, might play a role in explaining the source of X-ray emission from systems such as XRBs. For a review of the features of both leptonic and hadronic models as applied to blazars, see e.g., Böttcher (2010); Böttcher et al. (2013).

Despite the many important advances listed above, significant theoretical uncertainties remain which hinder a direct comparison between the dynamical models and observations. In particular, there is considerable uncertainty in the mass-loading physics of BZ jets. It is well known that GRMHD codes fail inside the highly-magnetized funnel (Gammie et al., 2003). This is because numerical errors accumulate when the ratio of the magnetic energy density to mass energy density becomes large. In what follows, we will refer to this ratio as the magnetization σ. To keep the numerical scheme stable, GRMHD codes typically inject matter when σ becomes larger than some (rather arbitrary) value. This effectively enforces a minimum density in the simulation, commonly referred to as a density floor. Although there are physical processes which may operate to mass-load the funnel, for example pair cascades (Blandford & Znajek, 1977; Levinson & Rieger, 2011; Broderick & Tchekhovskoy, 2015) or photon annihilation (Mościbrodzka et al., 2011), the injection of floor material is arbitrary and chosen simply to avoid numerical issues. Therefore, the funnel mass and internal energy densities are not determined by the GRMHD simulations.

Although the injected floor material has little effect on the dynamics, it can affect the resulting spectra and so must be considered when comparing GRMHD models with observations. Depending on the choice of initialisation for the floors, the plasma in the funnel might be tenuous enough such that it has a negligible contribution to the spectra. In this case, the jet emission is dominated by the

funnel wall or jet "sheath" as in Mościbrodzka & Falcke (2013) and Mościbrodzka et al. (2014). This "empty funnel" situation can also be achieved by simply removing floor material from the funnel during the radiative transport calculation. The material to remove can be chosen in a number of ways, for example, as cells in a large bipolar cone (Shcherbakov & McKinney, 2013), cells considered artificially hot or dense relative to their neighbours (Chan et al., 2015b), or cells with a large value of σ (O' Riordan et al., 2016b,a).

Recently, Gold et al. (2017) argued that the prescription used for treating the funnel material could be very important when interpreting future observations from the EHT. In particular, they showed that the black hole shadow can be completely obscured in the case of significant emission from the funnel, while the absence of strong funnel emission can, in fact, mimic features of the shadow. Therefore, in order to test general relativity using EHT observations it will be crucial to distinguish between features caused by strong-field gravity and those arising from the presence or absence of emitting matter in the jet. We perform a detailed investigation of the observational effects of mass-loading in the jet in chapter 6.

1.3 Thesis Structure

In the next chapter, we review important concepts related to plasma dynamics and radiative transport in rotating black hole spacetimes. In section 2.1, we introduce aspects of general relativity such as the metric tensor and geodesic equation. Then we describe the Kerr metric, which we use extensively throughout this thesis to model the gravitational field of rotating black holes. In section 2.2, we review the equations and assumptions of ideal GRMHD, which describe plasma dynamics in curved spacetimes. We discuss the possibility of energy extraction from rotating black holes in section 2.3. We also give a brief derivation of the BZ mechanism, which operates in all the numerical simulations considered in this thesis. Finally, in section 2.4 we discuss our approach for calculating the radiative properties of

the accreting plasma. We outline the radiative processes we consider as well as our assumptions about the emitting particles.

In chapter 3, we investigate the high-energy signatures of jets from the inner regions of XRBs. As mentioned previously, the role of jets in producing this high-energy emission remains uncertain. We find clear signatures of jets in the form of spectral breaks produced by overlapping jet and disk components. We also examine a large-scale plasmoid ejection event expected during state transitions, possibly launched by reconnecting magnetic fields near the horizon. We find significant variability in the ratio of the X-ray and γ-ray fluxes during this transient jet-launching process.

In chapter 4, we calculate the observational effects of black hole spin. We show that, even in magnetically-arrested disks (MADs) where the Blandford-Znajek (BZ) mechanism launches jets extremely efficiently, the resulting radiated power can deviate significantly from the predicted correlation between power radiated and black hole spin. At high spin, there is a much stronger dependence than expected, as well as a large increase in power for observers perpendicular to the spin axis. We find a simple analytic explanation for this result in terms of the strong gravitational effects experienced by photons emitted close to the horizon. The lower-energy radiation is independent of spin and so we identify the ratio of the X-ray and near-infrared power as a potential observational probe of black hole spin in XRBs.

The origin of variability in blazars is an important unsolved problem in high-energy astrophysics. The observed variability timescales range from minutes to years, the former being comparable to, and in some cases shorter than, the light-crossing time of the black hole. In chapter 5, we investigate the source of this variability in terms of turbulence in the jet launching region. The resulting power spectrum is very similar to the observed power-law spectrum, over many decades in frequency. Furthermore, turbulence in the flow naturally produces fluctuations in the plasma properties on scales smaller than the horizon radius, which may explain the ultra-fast variability.

In chapter 6, we investigate the observational effects of the mass-loading of force-free BZ jets. Understanding the contribution from plasma in the funnel region will be crucial for interpreting observations of Sgr A* with the EHT, expected next year. In particular, the absence of significant 230 GHz emission from the funnel can appear as "holes" in EHT images, mimicking features of the black hole shadow. We find significant differences in the spectra between the case where the funnel is mostly empty and the case where the funnel is filled with plasma, especially in the optical and X-ray bands. Interestingly, the radio emission in our models is largely independent of the mass-loading. In the context of Sgr A*, this means that even mass-loaded jets may appear as "holes" in EHT images. We also find that the current limits on the infra-red flux disfavor a mass-loaded funnel if the black hole is rapidly rotating.

Finally, in chapter 7 we summarize our main results. We also discuss the importance of studying the process of jet launching in light of the recent multi-messenger detection of gravitational waves and electromagnetic counterparts from merging neutron stars (Abbott et al., 2017a,b).

Chapter 2

Theoretical Background

In this chapter, we briefly review the theoretical framework and important concepts regarding the dynamical and radiative properties of accreting black hole systems. For simplicity, we often use naturalized units such that factors of Newton's gravitational constant G, the speed of light c, and the black hole mass M do not appear in the equations. As mentioned in chapter 1, we usually set $GM = c = 1$, however occasionally re-introduce these factors for clarity. We follow the convention that Greek indices run from 0 to 3, while Latin indices run from 1 to 3, and use $(-+++)$ for the metric signature.

2.1 Rotating Black Holes

In general relativity, the gravitational field is described by a quantity called the metric tensor. Throughout this thesis, we consider rotating black hole spacetimes which are described by the Kerr metric. In this section, we briefly introduce the metric tensor and geodesic equation. Then we discuss the Kerr metric in two useful coordinate systems which we use extensively in the following chapters.

2.1.1 The Metric Tensor

In 3-dimensional Euclidean space, the familiar line element in spherical coordinates (r, θ, ϕ) is given by

$$\mathrm{d}s^2 = \mathrm{d}r^2 + r^2\,\mathrm{d}\theta^2 + r^2 \sin^2\theta\,\mathrm{d}\phi^2 \tag{2.1}$$

This can be written compactly as

$$\mathrm{d}s^2 = g_{ij}\,\mathrm{d}x^i\,\mathrm{d}x^j \tag{2.2}$$

where g_{ij} are the components of the Euclidean metric

$$g_{ij} = \begin{pmatrix} 1 & 0 & 0 \\ 0 & r^2 & 0 \\ 0 & 0 & r^2\sin^2\theta \end{pmatrix} \tag{2.3}$$

and we have used the Einstein summation convention where a repeated index implies summation. In general relativity, spacetime is 4-dimensional and the line element reads

$$\mathrm{d}s^2 = g_{\mu\nu}\,\mathrm{d}x^\mu\,\mathrm{d}x^\nu \tag{2.4}$$

The metric tensor $g_{\mu\nu}$ satisfies the Einstein field equations (e.g., Carroll, 2004)

$$R_{\mu\nu} - \frac{1}{2}R\,g_{\mu\nu} = 8\pi\,T_{\mu\nu} \tag{2.5}$$

where $R_{\mu\nu}$ is the Ricci tensor, $R = R^\mu{}_\mu$ is the Ricci scalar, and $T^{\mu\nu}$ is the matter stress-energy tensor. These equations describe the coupling between the mass-energy distribution and the geometry of spacetime.

2.1.2 The Geodesic Equation

In the absence of external forces, photons and massive particles propagating in a gravitational field travel along geodesics. For a photon with four-momentum k^μ

$$k^\mu = \frac{\mathrm{d}x^\mu}{\mathrm{d}\lambda} \tag{2.6}$$

we calculate the photon trajectory by solving the geodesic equation

$$\frac{\mathrm{d}k^\mu}{\mathrm{d}\lambda} + \Gamma^\mu_{\alpha\beta} k^\alpha k^\beta = 0 \tag{2.7}$$

where λ is an affine parameter along the geodesic, and $\Gamma^\mu_{\alpha\beta}$ are the Christoffel symbols. The Christoffel symbols take the following form in a coordinate basis

$$\Gamma^\mu_{\alpha\beta} = \frac{1}{2} g^{\mu\nu} \left(\partial_\alpha g_{\beta\nu} + \partial_\beta g_{\alpha\nu} - \partial_\nu g_{\alpha\beta} \right) \tag{2.8}$$

where we have used the standard notation $\partial_\alpha = \partial/\partial x^\alpha$. Using (2.6), the geodesic equation can also be written as

$$k^\alpha \left(\partial_\alpha k^\mu + \Gamma^\mu_{\alpha\beta} k^\beta \right) = k^\alpha \nabla_\alpha k^\mu = 0 \tag{2.9}$$

where ∇_α is the covariant derivative.

2.1.3 The Kerr Metric in Boyer-Lindquist Coordinates

In this thesis, we consider rotating black hole spacetimes and use a "test fluid" approximation such that the contribution to the gravitational field from the accreting plasma is negligible. In this case, the gravitational field is described by the Kerr metric, which is a solution to the vacuum Einstein field equations

$$R_{\mu\nu} = 0 \tag{2.10}$$

The Boyer-Lindquist coordinates (BL; Boyer & Lindquist, 1967) are the simplest known coordinates for the Kerr metric, with a single off-diagonal term. In BL coordinates (t, r, θ, ϕ), the Kerr line element reads

$$\mathrm{d}s^2 = -\left(1 - \frac{2r}{\Sigma}\right)\mathrm{d}t^2 + \frac{\Sigma}{\Delta}\,\mathrm{d}r^2 + \Sigma\,\mathrm{d}\theta^2 + \frac{A\sin^2\theta}{\Sigma}\,\mathrm{d}\phi^2 - \frac{4ra}{\Sigma}\sin^2\theta\,\mathrm{d}t\,\mathrm{d}\phi \quad (2.11)$$

where

$$A = \left(r^2 + a^2\right)^2 - a^2\Delta\sin^2\theta \quad (2.12)$$

$$\Delta = r^2 + a^2 - 2r \quad (2.13)$$

$$\Sigma = r^2 + a^2\cos^2\theta \quad (2.14)$$

and $-1 \leq a \leq 1$ is the dimensionless spin of the black hole. The determinant of the metric is

$$g = \det\left(g_{\mu\nu}\right) = -\Sigma^2\sin^2\theta \quad (2.15)$$

For completeness, the inverse metric is given by (Bardeen et al., 1972)

$$\left(\partial_s\right)^2 = -\frac{A}{\Sigma\Delta}\left(\partial_t\right)^2 + \frac{\Delta}{\Sigma}\left(\partial_r\right)^2 + \frac{1}{\Sigma}\left(\partial_\theta\right)^2 + \frac{\Delta - a^2\sin^2\theta}{\Sigma\Delta\sin^2\theta}\left(\partial_\phi\right)^2 - \frac{4ra}{\Sigma\Delta}\,\partial_t\,\partial_\phi \quad (2.16)$$

which we make use of in appendix B.

As in the familiar form of the Schwarzschild solution, the Kerr metric in BL coordinates is singular on the event horizon at $r = r_H$, where $\Delta = 0$

$$r_H = \left(1 + \sqrt{1 - a^2}\right) r_g \quad (2.17)$$

Here, $r_g = GM/c^2$ is the gravitational radius (note that $r_g = 1$ in our units). For non-rotating black holes ($a = 0$), the horizon is located at the Schwarzschild radius

$$r_S = \frac{2GM}{c^2} \quad (2.18)$$

and the Kerr metric (2.11) reduces to the usual Schwarzschild solution. For maximally rotating black holes ($a = 1$), the horizon is located at $r_H = r_g$.

There is an interesting region near the horizon known as the ergosphere. Observers within the ergosphere are forced to rotate in the same direction as the black hole spin, a phenomenon known as frame dragging (for more details, see the discussion of circular motion in the Kerr spacetime in Appendix B.1). As discussed in section 2.3, the ergosphere also plays a central role in the extraction of rotational energy from Kerr black holes. Since no static observers can exist inside the ergosphere, its outer boundary is often referred to as the static limit. The static limit is located at $r = r_E$, where $g_{tt} = -\left(1 - \frac{2r}{\Sigma}\right) = 0$

$$r_E = \left(1 + \sqrt{1 - a^2 \cos^2\theta}\right) r_g \tag{2.19}$$

In particular, note that $r_E = r_S$ at the equator ($\theta = \pi/2$), and $r_E = r_H$ at the poles ($\theta = 0$ and $\theta = \pi$).

2.1.4 The Kerr Metric in Kerr-Schild Coordinates

The Kerr-Schild (KS) coordinates $(\mathfrak{t}, \mathfrak{r}, \vartheta, \varphi)$ are regular on the event horizon, which makes them particularly useful for numerical simulations of plasma accretion and near-horizon radiation transport. We make extensive use of these coordinates in all of our GRMHD and radiative calculations, as well as in our derivation of the BZ process in section 2.3.3. The KS coordinates are the rotating analogue of the Eddington-Finkelstein coordinates (e.g., Poisson, 2004), and are closely related to the BL coordinates with $\mathfrak{r} = r$ and $\vartheta = \theta$. The transformation matrix from BL to KS has (e.g., McKinney & Gammie, 2004)

$$\frac{\partial \mathfrak{t}}{\partial r} = \frac{2r}{\Delta} \tag{2.20}$$

$$\frac{\partial \varphi}{\partial r} = \frac{a}{\Delta} \tag{2.21}$$

with all other off-diagonal components 0, and all diagonal components 1. The components of the inverse transformation are identical, with the opposite signs for

the off-diagonal components. The line element in KS coordinates is

$$\begin{aligned} \mathrm{d}s^2 = &- \left(1 - \frac{2r}{\Sigma}\right) \mathrm{d}\mathfrak{t}^2 + \left(\frac{4r}{\Sigma}\right) \mathrm{d}\mathfrak{t}\, \mathrm{d}r + \left(1 + \frac{2r}{\Sigma}\right) \mathrm{d}r^2 + \Sigma\, \mathrm{d}\theta^2 \\ &+ \left(\Sigma + a^2 \sin^2\theta \left(1 + \frac{2r}{\Sigma}\right)\right) \sin^2\theta\, \mathrm{d}\varphi^2 \\ &- \left(\frac{4ar\sin^2\theta}{\Sigma}\right) \mathrm{d}\varphi\, \mathrm{d}\mathfrak{t} - 2a \left(1 + \frac{2r}{\Sigma}\right) \sin^2\theta\, \mathrm{d}\varphi\, \mathrm{d}r \end{aligned} \tag{2.22}$$

where we have used that $\mathfrak{r} = r$ and $\vartheta = \theta$. The metric determinant is the same as in the BL case (2.15). For completeness, the inverse metric is given by

$$\begin{aligned} (\partial_s)^2 = &- \left(1 + \frac{2r}{\Sigma}\right) (\partial_\mathfrak{t})^2 + \frac{\Delta}{\Sigma} (\partial_r)^2 + \frac{1}{\Sigma} (\partial_\theta)^2 + \frac{1}{\Sigma \sin^2\theta} (\partial_\varphi)^2 \\ &+ \frac{4r}{\Sigma}\, \partial_\mathfrak{t}\, \partial_r + \frac{2a}{\Sigma}\, \partial_r\, \partial_\varphi \end{aligned} \tag{2.23}$$

which we use in section 2.3.3.

2.2 Equations of Ideal GRMHD

Throughout this thesis, we treat the accreting plasma as a perfectly conducting fluid, which is a very good approximation in a wide range of astrophysical systems (see e.g., section 1.5 in McKinney, 2004). In this approximation, the plasma evolution is described by the equations of ideal GRMHD, which we review in this section. Further details can be found in Gammie et al. (2003) and references therein.

2.2.1 Conservation of Mass, Energy, and Momentum

Conservation of mass is described by the continuity equation (e.g., Landau & Lifshitz, 1959), which can be written in covariant form as

$$\nabla_\mu (\rho u^\mu) = 0 \tag{2.24}$$

Here, ρ is the mass density, u^μ is the fluid four-velocity, and ∇_μ is the covariant derivative. Conservation of energy and momentum are expressed in terms of the stress-energy tensor $T^{\mu\nu}$ as

$$\nabla_\mu T^{\mu\nu} = 0 \tag{2.25}$$

The stress-energy tensor is symmetric with $T^{\mu\nu} = T^{\nu\mu}$. For a plasma, $T^{\mu\nu}$ can be decomposed into the sum of a fluid part

$$T^{\mu\nu}_{\text{fluid}} = (\rho + P + U)\, u^\mu u^\nu + P\, g^{\mu\nu} \tag{2.26}$$

and an electromagnetic (EM) part

$$T^{\mu\nu}_{\text{EM}} = F^{\mu\alpha} F^{\nu}{}_{\alpha} - \frac{1}{4} g^{\mu\nu} F_{\alpha\beta} F^{\alpha\beta} \tag{2.27}$$

In the above expressions, P is the gas pressure, U is the internal energy density, $g_{\mu\nu}$ is the metric tensor, and $F^{\mu\nu}$ is the Faraday tensor. In an orthonormal basis, the components of the Faraday tensor can be written in terms of the usual electric and magnetic field three-vectors $\mathbf{E}$ and $\mathbf{B}$ as (e.g., Jackson, 1975)

$$F_{\mu\nu} = \begin{pmatrix} 0 & -E_x & -E_y & -E_z \\ E_x & 0 & B_z & -B_y \\ E_y & -B_z & 0 & B_x \\ E_z & B_y & -B_x & 0 \end{pmatrix} \tag{2.28}$$

Note that the Faraday tensor is antisymmetric with $F_{\mu\nu} = -F_{\nu\mu}$. The pressure and internal energy are related by the ideal gas equation of state

$$P = (\Gamma - 1)\, U \tag{2.29}$$

where we use an adiabatic index of $\Gamma = 4/3$, valid for relativistic fluids.

2.2.2 Maxwell's Equations

The evolution of the electromagnetic field is described by Maxwell's equations. The source-free Maxwell's equations read

$$\nabla \cdot \mathbf{B} = 0 \tag{2.30}$$

$$\nabla \times \mathbf{E} = -\partial_t \mathbf{B} \tag{2.31}$$

These can be written in covariant form as (e.g., Jackson, 1975)

$$\partial_\lambda F_{\mu\nu} + \partial_\nu F_{\lambda\mu} + \partial_\mu F_{\nu\lambda} = 0 \tag{2.32}$$

or more compactly as

$$\nabla_\mu (\star F)^{\mu\nu} = 0 \tag{2.33}$$

where $(\star F)^{\mu\nu} = \frac{1}{2}\epsilon^{\mu\nu\alpha\beta}F_{\alpha\beta}$ is the Hodge dual of the Faraday tensor, and $\epsilon^{\mu\nu\alpha\beta}$ is the Levi-Civita tensor. The remaining Maxwell's equations are

$$\nabla \cdot \mathbf{E} = 4\pi\rho_c \tag{2.34}$$

$$\nabla \times \mathbf{B} = 4\pi\mathbf{J} + \partial_t \mathbf{E} \tag{2.35}$$

where ρ_c is the charge density, and $\mathbf{J}$ is the three-current density. Introducing the four-current density $J^\mu = (\rho_c, \mathbf{J})$, these can be written as

$$\nabla_\nu F^{\mu\nu} = J^\mu \tag{2.36}$$

As we show below, for a perfectly conducting plasma, the evolution of the EM field is determined by the source-free Maxwell's equations alone.

2.2.3 Ideal MHD Approximation

The assumption of perfect conductivity greatly simplifies the MHD equations. This approximation is known as "ideal" MHD. Since the electric field vanishes in

the rest-frame of a perfect conductor, it is convenient to derive the ideal MHD condition in terms of three-vector quantities, and then write the final result in covariant form. Denoting the plasma rest-frame with a prime, we can write the ideal MHD condition simply as $\mathbf{E}' = 0$. Next, consider a Lorentz transformation of the fields into a frame in which the plasma moves with three-velocity $\mathbf{v}$ (e.g., Jackson, 1975)

$$\mathbf{E} = \gamma\left(\mathbf{E}' - \mathbf{v}\times\mathbf{B}'\right) - \frac{\gamma^2}{\gamma+1}\mathbf{v}\left(\mathbf{v}\cdot\mathbf{E}'\right) = -\mathbf{v}\times\gamma\mathbf{B}' \tag{2.37}$$

$$\mathbf{B} = \gamma\left(\mathbf{B}' + \mathbf{v}\times\mathbf{E}'\right) - \frac{\gamma^2}{\gamma+1}\mathbf{v}\left(\mathbf{v}\cdot\mathbf{B}'\right) = \gamma\mathbf{B}' - \frac{\gamma^2}{\gamma+1}\mathbf{v}\left(\mathbf{v}\cdot\mathbf{B}'\right) \tag{2.38}$$

where $\gamma = 1/\sqrt{1-v^2}$ is the Lorentz factor, and we have used that $\mathbf{E}' = 0$ in expressions on the right. This leads to the following relationship between the electric and magnetic fields, which is Ohm's Law for ideal MHD

$$\mathbf{E} + \mathbf{v}\times\mathbf{B} = 0 \tag{2.39}$$

Using this relation, the electric field appearing in the induction equation (2.31) can be replaced by $-\mathbf{v}\times\mathbf{B}$ giving

$$\nabla\times(\mathbf{v}\times\mathbf{B}) = \partial_t\mathbf{B} \tag{2.40}$$

Therefore, in the ideal MHD approximation, the evolution of the EM field is determined by the source-free Maxwell's equations. The remaining Maxwell's equations (2.35) simply determine the current, and are not needed for the evolution. Recognizing (2.39) as the vanishing of the Lorentz force, the ideal MHD condition can be written in covariant form as

$$u_\mu F^{\mu\nu} = 0 \tag{2.41}$$

2.2.4 Ideal GRMHD Stress-Energy Tensor

For an ideal plasma, we can re-write the stress-energy tensor in a convenient form by introducing the comoving magnetic field four-vector

$$b^\mu = u_\nu \left(\star F\right)^{\nu\mu} \tag{2.42}$$

In the orthonormal fluid frame, this vector has components $b^\mu = (0, B^i)$, where $B^i = \left(\star F\right)^{it}$ are the components of the magnetic field three-vector $\mathbf{B}$. Using the ideal MHD condition (2.41), we can re-arrange equation (2.42) and express the Faraday tensor in terms of b^μ as

$$F^{\mu\nu} = \epsilon^{\mu\nu\alpha\beta} u_\alpha b_\beta \tag{2.43}$$

Noting that $u_\mu b^\mu = 0$, the EM stress-energy tensor (2.27) can then be re-written as

$$T^{\mu\nu}_{\mathrm{EM}} = b^2 u^\mu u^\nu + \frac{1}{2} b^2 g^{\mu\nu} - b^\mu b^\nu \tag{2.44}$$

where $b^2 = b^\mu b_\mu$. Finally, the ideal GRMHD stress-energy tensor is

$$T^{\mu\nu} = \left(\rho + P + U + b^2\right) u^\mu u^\nu + \left(P + \frac{1}{2} b^2\right) g^{\mu\nu} - b^\mu b^\nu \tag{2.45}$$

The ideal MHD expression for the EM field (2.43) can also be used to write the dual field simply as

$$\left(\star F\right)^{\mu\nu} = b^\mu u^\nu - b^\nu u^\mu \tag{2.46}$$

From this we find that

$$F^{\mu\nu} \left(\star F\right)_{\mu\nu} = 0 \tag{2.47}$$

which is the covariant form of the Lorentz invariant expression

$$\mathbf{E} \cdot \mathbf{B} = 0 \tag{2.48}$$

2.2.5 Summary of Ideal GRMHD Equations

In summary, the equations of ideal GRMHD are

$$\nabla_\mu \left(\rho u^\mu\right) = 0 \tag{2.49}$$

$$\nabla_\mu T^{\mu\nu} = 0 \tag{2.50}$$

$$\nabla_\mu \left(\star F\right)^{\mu\nu} = 0 \tag{2.51}$$

with $T^{\mu\nu}$ given by (2.45), and $(\star F)^{\mu\nu}$ given by (2.46). Note that these equations must be supplemented by the equation of state (2.29), relating the pressure and internal energy. Also, recall that we have used the ideal MHD Ohm's law (2.41) in the expressions for $T^{\mu\nu}$ and $(\star F)^{\mu\nu}$, and to eliminate the second pair of Maxwell's equations (2.36).

2.3 Energy Extraction from Kerr Black Holes

The rotational energy stored in a spinning black hole is potentially extremely large. This large reservoir of energy, and the counter-intuitive observation by Penrose (1969) that this energy can in fact be tapped, makes rotating black holes attractive candidates for powering relativistic jets. Here, we estimate the energy available for extraction. The "irreducible" mass $M_{\rm irr}$ of a Kerr black hole can be written in terms of the gravitational mass M as (Carroll, 2004)

$$\left(M_{\rm irr}\right)^2 = \frac{1}{2} M\, r_H \tag{2.52}$$

where we have used units such that $G = c = 1$ and so $r_H = \left(1 + \sqrt{1 - a^2}\right) M$. The rotational energy is then given by

$$E_{\rm spin} = M - M_{\rm irr} = M \left(1 - \sqrt{\frac{1 + \sqrt{1 - a^2}}{2}}\right) \tag{2.53}$$

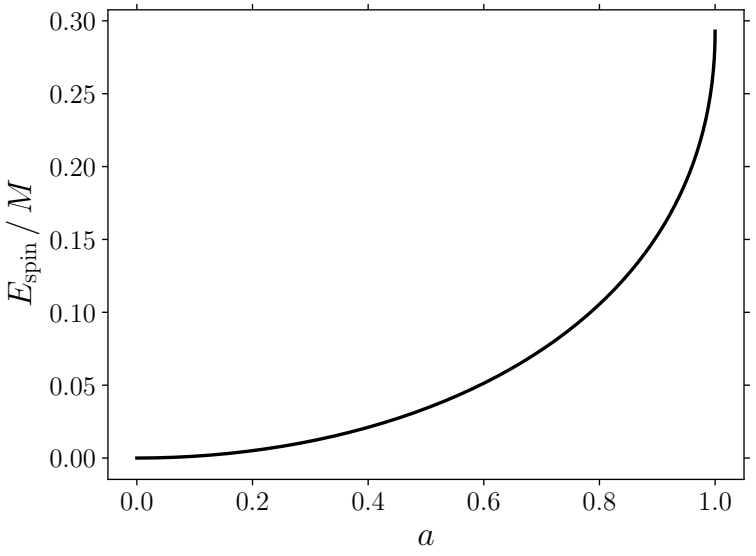

FIGURE 2.1: Rotational energy of a Kerr black hole as a function of the dimensionless spin a.

In Figure 2.1, we plot the rotational energy as a function of the dimensionless spin a. Note that for a Schwarzschild black hole $a = 0$ and $E_{\rm spin} = 0$, while for a maximally spinning black hole $a = 1$ and

$$E_{\rm spin}\,(a = 1) \approx 0.29\,M \approx 5 \times 10^{54} \left(\frac{M}{10\,M_\odot}\right) \text{erg} \tag{2.54}$$

where $M_\odot$ is the mass of the Sun.

In the rest of this section, we briefly review some important concepts regarding energy extraction from rotating black holes. Firstly, we introduce the framework used to describe energy conservation in general relativity. Then we discuss the possibility of energy extraction in the Kerr spacetime due to the existence of an ergosphere (known as the Penrose process; Penrose, 1969). Finally, we briefly derive the BZ mechanism (Blandford & Znajek, 1977), which is a potentially astrophysically relevant electromagnetic realization of the Penrose process (Lasota et al., 2014).

2.3.1 Killing Vectors and Energy Conservation

Spacetime symmetries imply the existence of conserved quantities along geodesics. Each symmetry of the spacetime has an associated Killing vector field K^μ, which satisfies Killing's equation (e.g., Carroll, 2004)

$$\nabla_\mu K_\nu + \nabla_\nu K_\mu = 0 \tag{2.55}$$

If $x^\mu(\lambda)$ is a geodesic with tangent vector $u^\mu = \mathrm{d}x^\mu/\,\mathrm{d}\lambda$, then

$$u^\mu \nabla_\mu (K_\nu u^\nu) = u^\mu u^\nu \nabla_\mu K_\nu + K_\nu u^\mu \nabla_\mu u^\nu = 0 \tag{2.56}$$

where the first term on the right vanishes because of Killing's equation (2.55), and the second term vanishes since $x^\mu(\lambda)$ is a geodesic (2.9). Therefore, the quantity $K_\mu u^\mu$ is conserved along geodesics.

The Kerr spacetime is stationary and admits a timelike Killing vector ξ^μ. In a coordinate system adapted to stationarity, such as the BL and KS coordinates described in section 2.1, the components of this timelike Killing vector are

$$\xi^\mu = (\partial_t)^\mu = \delta^\mu_t \tag{2.57}$$

For a photon four-momentum k^μ, we see that the Killing energy

$$\mathcal{E} = -\xi^\mu k_\mu = -\delta^\mu_t k_\mu = -k_t \tag{2.58}$$

is conserved along null geodesics. Recall that the four-velocity of any physical observer is a timelike unit vector satisfying $u^\mu u_\mu = -1$. Importantly, $\mathcal{E}$ is not the energy measured by any physical observer since ξ^μ is not a unit vector, except in the asymptotically flat region infinitely far from the black hole. For this reason, $\mathcal{E}$ is often referred to as the "energy at infinity". It is the energy that would be measured by a static observer if the photon or particle escapes to infinity.

For a matter stress-energy tensor $T^{\mu\nu}$ satisfying $\nabla_\mu T^{\mu\nu} = 0$, it follows from Killing's equation (2.55) that

$$\nabla_\mu \left(-T^\mu{}_\nu \, \xi^\nu\right) = \nabla_\mu \mathcal{P}^\mu = 0 \tag{2.59}$$

where

$$\mathcal{P}^\mu = -T^\mu{}_\nu \, \xi^\nu = -T^\mu{}_t \tag{2.60}$$

is the conserved energy flux. This is also referred to as the Noether current (Lasota et al., 2014). The flux of energy in the radial direction is found by integrating the radial component of the Noether current

$$\dot{E} = \int \sqrt{-g} \, \mathrm{d}x^\theta \, \mathrm{d}x^\phi \, \mathcal{P}^r \tag{2.61}$$

2.3.2 The Penrose Process

By the following simple thought experiment, Penrose (1969) showed that energy can be extracted from rotating black holes. The basic idea is that, due to the existence of an ergosphere, particles and fields near the horizon can access "negative energy" states (we will explain the meaning of this statement below). In the example given by Penrose (1969), a particle within the ergosphere splits into a negative energy particle which falls into the black hole, and a positive energy particle which escapes to infinity. Conservation of energy implies that the particle which escapes has more energy than the original particle, and so energy has been extracted from the black hole. Below we give a more detailed explanation of this process.

In the Kerr spacetime, consider a freely-falling particle that enters the ergosphere (2.19) with four-momentum p_1^μ, and Killing energy

$$\mathcal{E}_1 = -g_{\mu\nu} \, \xi^\mu p_1^\nu \tag{2.62}$$

Recall that the Killing energy is conserved along the particle's trajectory. At infinity, both ξ^μ and p_1^μ are timelike, and so their inner product is negative. It follows that the "energy at infinity" $\mathcal{E}_1$ is positive, as expected. In the ergosphere, the ingoing particle disintegrates into two particles with four-momenta p_2^μ and p_3^μ, and conserved Killing energies

$$\mathcal{E}_2 = -g_{\mu\nu}\,\xi^\mu p_2^\nu\,, \qquad \mathcal{E}_3 = -g_{\mu\nu}\,\xi^\mu p_3^\nu \tag{2.63}$$

Let particle 2 escape to infinity, and so $\mathcal{E}_2 > 0$, while particle 3 falls into the black hole. Within the ergosphere, ξ^μ becomes spacelike

$$\xi^\mu\,\xi_\mu = g_{\mu\nu}\,\xi^\mu\,\xi^\nu = g_{\mu\nu}\,\delta_t^\mu\,\delta_t^\nu = g_{tt} > 0 \tag{2.64}$$

and so the inner product $\xi^\mu p_\mu$ is not necessarily negative here. This means that, because particle 3 remains within the outer boundary of the ergosphere, its conserved Killing energy can be negative $\mathcal{E}_3 < 0$. For the remainder of this section, let us consider the case where $\mathcal{E}_3 < 0$. Conservation of momentum implies that

$$p_1^\mu = p_2^\mu + p_3^\mu \tag{2.65}$$

Contracting this with ξ^μ we find that

$$\mathcal{E}_1 = \mathcal{E}_2 + \mathcal{E}_3 \tag{2.66}$$

But $\mathcal{E}_1 > 0$, $\mathcal{E}_2 > 0$, and $\mathcal{E}_3 < 0$, which means that

$$\mathcal{E}_2 > \mathcal{E}_1 \tag{2.67}$$

Thus, particle 2 emerges from the ergosphere with more energy than particle 1 had entering the ergosphere. This excess energy comes at the expense of the rotational energy of the black hole. The scenario considered here is sometimes referred to as the "particle" or "mechanical" Penrose process, while the term "Penrose process" refers more generally to any process of energy extraction which relies on the

spacelike character of ξ^μ within the ergosphere (Lasota et al., 2014).

2.3.3 The Blandford-Znajek Mechanism

The BZ mechanism (Blandford & Znajek, 1977) is an electromagnetic realization of the Penrose process (Lasota et al., 2014). In this section, we give a brief derivation of this result. Following McKinney & Gammie (2004), we use KS coordinates instead of the BL coordinates used in the original derivation by Blandford & Znajek (1977), and so the electromagnetic field requires no special treatment at the horizon.

We assume that the black hole is surrounded by a tenuous, perfectly conducting plasma, and that the energy-momentum density of the electromagnetic field is many orders of magnitude greater than that of the fluid, $T^{\mu\nu}_{\rm EM} \gg T^{\mu\nu}_{\rm fluid}$. In this limit, the plasma is known as "force-free", and the electromagnetic stress-energy tensor is conserved by itself

$$\nabla_\mu T^{\mu\nu} = \nabla_\mu \left(T^{\mu\nu}_{\rm fluid} + T^{\mu\nu}_{\rm EM}\right) = \nabla_\mu T^{\mu\nu}_{\rm EM} = 0 \tag{2.68}$$

For simplicity, we assume that the field is axisymmetric ($\partial_\varphi \to 0$), and stationary ($\partial_{\rm t} \to 0$). We write the Faraday tensor in terms of the vector potential A_μ as

$$F_{\mu\nu} = \partial_\mu A_\nu - \partial_\nu A_\mu \tag{2.69}$$

Putting this into the perfectly conducting condition $F^{\mu\nu}\left(\star F\right)_{\mu\nu} = 0$ gives

$$A_{\varphi,\theta}\, A_{{\rm t},r} = A_{{\rm t},\theta}\, A_{\varphi,r} \tag{2.70}$$

where we have used the compact notation $\partial_\mu A_\nu = A_{\nu,\mu}$. From this we define

$$\omega\left(r,\theta\right) = -\frac{A_{{\rm t},\theta}}{A_{\varphi,\theta}} = -\frac{A_{{\rm t},r}}{A_{\varphi,r}} \tag{2.71}$$

This quantity is usually interpreted as the angular velocity of the field lines (Blandford & Znajek, 1977; McKinney & Gammie, 2004). In this case, the components of the Faraday tensor (2.69) can be written as

$$F_{\mu\nu} = \sqrt{-g} \begin{pmatrix} 0 & -\omega B^\theta & \omega B^r & 0 \\ \omega B^\theta & 0 & B^\varphi & -B^\theta \\ -\omega B^r & -B^\varphi & 0 & B^r \\ 0 & B^\theta & -B^r & 0 \end{pmatrix} \tag{2.72}$$

where

$$A_{\theta,r} - A_{r,\theta} = \sqrt{-g} B^\varphi \tag{2.73}$$

$$A_{\varphi,\theta} = \sqrt{-g} B^r \tag{2.74}$$

$$A_{\varphi,r} = -\sqrt{-g} B^\theta \tag{2.75}$$

Since the field is axisymmetric and force-free, the radial energy flux (2.61) is given by

$$\dot{E} = 2\pi \int_0^\pi \sqrt{-g}\, \mathrm{d}\theta\, \mathcal{P}^r \tag{2.76}$$

where the radial component of the Noether current is purely electromagnetic

$$\begin{aligned} \mathcal{P}^r &= -\left(T_{\mathrm{EM}}\right)^r{}_{\mathrm{t}} = -F^{r\alpha} F_{\mathrm{t}\alpha} = -F^{r\theta} F_{\mathrm{t}\theta} \\ &= -2\left(B^r\right)^2 \omega\, r \left(\omega - \frac{a}{2r}\right) \sin^2\theta - B^r B^\varphi \omega \Delta \sin^2\theta \end{aligned} \tag{2.77}$$

and we have used the inverse metric (2.23) to lower the indices on $F^{r\theta}$. On the horizon $r = r_H$ and $\Delta = 0$, so the Noether current reduces to

$$\mathcal{P}^r\left(r = r_H\right) = 2\left(B^r\right)^2 \omega\, r_H \left(\Omega_H - \omega\right) \sin^2\theta \tag{2.78}$$

where $\Omega_H = a/2\, r_H$ is the angular velocity of the horizon (Bardeen et al., 1972). Therefore, for $\left(B^r\right)^2 > 0$ there will be a net outward energy flux at the horizon if the field lines are rotating in the same direction as the black hole, with an angular

velocity less than that of the horizon

$$\mathcal{P}^r\left(r = r_H\right) > 0 \quad \Longleftrightarrow \quad 0 < \omega < \Omega_H \tag{2.79}$$

This electromagnetic extraction of energy from a rotating black hole is the BZ mechanism. Throughout this thesis, we consider numerical realizations of this process using the `HARM` code (Gammie et al., 2003).

2.4 Radiation Transport

In order to compare theoretical models of plasma dynamics with observations, we must calculate the resulting electromagnetic radiation. In this section, we describe our treatment of the emission and interaction of radiation with plasma in curved spacetimes.

2.4.1 Radiative Transfer Equation

The radiative transfer equation describes the change in specific intensity I_ν along a ray due to the emission and absorption of radiation at frequency ν (Rybicki & Lightman, 1979)

$$\frac{\mathrm{d}I_\nu}{\mathrm{d}l} = j_\nu - \alpha_\nu I_\nu \tag{2.80}$$

Here, $\mathrm{d}l$ is the differential path length along the ray, j_ν is the emission coefficient, and α_ν is the absorption coefficient. Note that the subscript ν is not a vector index in this case, but instead indicates the frequency dependence of these quantities. The specific intensity has units of erg s^{-1} cm^{-2} ster^{-1} Hz^{-1}, and is related to the net radiative flux in the direction $\hat{\mathbf{n}}$ by integrating over all solid angles $\mathrm{d}\Omega$

$$F_\nu = \int \mathrm{d}\Omega \, I_\nu \cos\theta \tag{2.81}$$

where $\cos\theta$ is the angle between $\hat{\mathbf{n}}$ and a given ray. In the form (2.80), the radiative transfer equation includes emission and absorption processes along the

ray, but does not include scattering into or out of the ray. Scattering involves more complicated angular and frequency-dependent terms, and the resulting transfer equation takes the form of an integrodifferential equation which in general must be solved by numerical techniques such as Monte Carlo methods (e.g., Dolence et al., 2009).

2.4.2 Lorentz Invariant Transfer Equation

It is convenient to write the transfer equation (2.80) in terms of Lorentz invariant quantities. Following Rybicki & Lightman (1979), below we give some simple physical arguments for the transformation properties of the specific intensity, emission, and absorption coefficients. Detailed derivations of these quantities can be found in Mihalas & Mihalas (1984).

Firstly, we show that the Lorentz invariant specific intensity is given by I_ν/ν^3. Consider the comoving frame of a group of particles with a small spread in position and momentum at a given time. These particles occupy the small phase space volume $\mathrm{d}\mathcal{V}' = \mathrm{d}^3x'\,\mathrm{d}^3p'$. To first order, the particles have $\mathrm{d}p'_t = 0$, since the contribution to the energy from the spatial momentum is quadratic in the comoving frame. For an observer moving with velocity β in the x-direction, the particles occupy a volume $\mathrm{d}\mathcal{V} = \mathrm{d}^3x\,\mathrm{d}^3p$. A Lorentz transformation gives

$$\mathrm{d}^3x = \gamma^{-1}\,\mathrm{d}^3x' \tag{2.82}$$

$$\mathrm{d}p_x = \gamma\,(\mathrm{d}p'_x + \beta\,\mathrm{d}p'_t) = \gamma\,\mathrm{d}p'_x \tag{2.83}$$

$$\mathrm{d}p_y = \mathrm{d}p'_y \tag{2.84}$$

$$\mathrm{d}p_z = \mathrm{d}p'_z \tag{2.85}$$

where $\gamma = 1/\sqrt{1-\beta^2}$, and we have used that $\mathrm{d}p'_t = 0$. Therefore, $\mathrm{d}\mathcal{V} = \mathrm{d}\mathcal{V}'$ and so the phase space volume is a Lorentz invariant quantity. Similarly, the phase space density $f = \mathrm{d}N/\,\mathrm{d}\mathcal{V}$ is Lorentz invariant, since $\mathrm{d}N$ is simply the number of particles. The phase space density is related to the specific intensity by (Rybicki

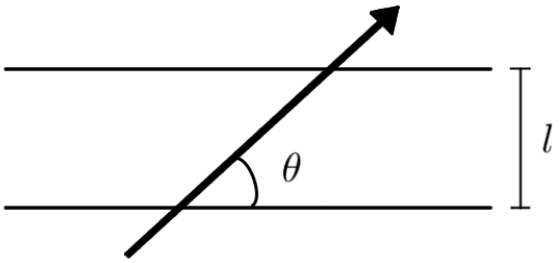

FIGURE 2.2: Beam of radiation propagating through an absorbing medium of thickness l at an angle θ in the rest frame of the slab.

& Lightman, 1979)

$$h\nu f \, \mathrm{d}^3p = h\nu f p^2 \, \mathrm{d}p \, \mathrm{d}\Omega = \frac{I_\nu}{c} \, \mathrm{d}\Omega \, \mathrm{d}\nu \tag{2.86}$$

Writing $p = h\nu/c$, we find that

$$\frac{I_\nu}{\nu^3} \sim f \tag{2.87}$$

and so I_ν/ν^3 is Lorentz invariant.

To show that the Lorentz invariant absorption coefficient is $\nu\alpha_\nu$, we consider a beam of photons propagating through an absorbing medium of thickness l at an angle θ in the rest frame of the medium (see Figure 2.2). The optical depth along the beam is given by

$$\tau_\nu = \left(\frac{l}{\sin\theta}\right)\alpha_\nu = \left(\frac{l}{\nu\sin\theta}\right)(\nu\alpha_\nu) \tag{2.88}$$

The optical depth is a Lorentz invariant quantity, since $e^{-\tau_\nu}$ simply gives the fraction of photons passing through the material. The slab thickness l is unaffected by a Lorentz boost in the x-direction. Similarly, the quantity $\nu\sin\theta$ is unchanged since it is proportional to the y component of the photon four-momentum. Therefore, from (2.88) we find that $\nu\alpha_\nu$ must also be Lorentz invariant.

Finally, we can find the invariant emission coefficient j_ν/ν^2 by considering the source function $S_\nu = j_\nu/\alpha_\nu$. By re-arranging the transfer equation (2.80), this

quantity appears as the difference $S_\nu - I_\nu$ and so must have the same transformation properties as I_ν. From this we see that j_ν/ν^2 is Lorentz invariant.

The transfer equation (2.80) can be written in terms of the Lorentz invariant intensity, emission, and absorption coefficients as (Rybicki & Lightman, 1979; Mihalas & Mihalas, 1984; Dolence et al., 2009)

$$\frac{1}{\mathcal{C}}\frac{\mathrm{d}}{\mathrm{d}\lambda}\left(\frac{I_\nu}{\nu^3}\right) = \left(\frac{j_\nu}{\nu^2}\right) - (\nu\alpha_\nu)\left(\frac{I_\nu}{\nu^3}\right) \tag{2.89}$$

where λ is an affine parameter along the ray (2.6). $\mathcal{C}$ is a constant which depends on our choice of units. Typically, we set $\mathcal{C} = h\, r_g/mc^2$, where h is Planck's constant, $r_g = GM/c^2$ is the gravitational radius, and m is the electron mass. In terms of the differential optical depth

$$\mathrm{d}\tau_\nu = (\nu\alpha_\nu)\,\mathcal{C}\,\mathrm{d}\lambda \tag{2.90}$$

and invariant source function $\mathcal{S}_\nu = S_\nu/\nu^3$, equation (2.89) can be written simply as

$$\frac{\mathrm{d}\mathcal{I}_\nu}{\mathrm{d}\tau_\nu} = \mathcal{S}_\nu - \mathcal{I}_\nu \tag{2.91}$$

where $\mathcal{I}_\nu = I_\nu/\nu^3$. This equation can be formally solved by (Rybicki & Lightman, 1979)

$$\mathcal{I}_\nu(\tau_\nu) = \mathcal{I}_\nu(0)\, e^{-\tau_\nu} + \int_0^{\tau_\nu} \mathrm{d}\tau'_\nu\, e^{-(\tau_\nu - \tau'_\nu)}\, \mathcal{S}_\nu(\tau'_\nu) \tag{2.92}$$

In the special case of a constant source function (e.g., across a single grid cell in a numerical simulation), this solution takes the particularly simple form

$$\mathcal{I}_\nu(\tau_\nu) = \mathcal{S}_\nu + e^{-\tau_\nu}\left(\mathcal{I}_\nu(0) - \mathcal{S}_\nu\right) \tag{2.93}$$

The Lorentz invariant transfer equation (2.89) is valid only in local orthonormal frames. To account for general-relativistic effects in curved spacetimes, we calculate the photon trajectories by solving the geodesic equation (2.7). We also calculate the photon energy in the local fluid frame via the inner product between

the photon four-momentum k^μ and the fluid four-velocity u^μ

$$E = -k^\mu u_\mu \tag{2.94}$$

which depends on the metric.

2.4.3 Radiative Processes

Throughout this thesis, we calculate the radiative properties of jets and accretion flows using a radiative transport code based on `grmonty` (Dolence et al., 2009). In this section, we describe our main assumptions regarding the relevant radiative processes. We account for synchrotron emission, self-absorption, and Compton scattering, since these are expected to be the dominant radiative processes in hot, highly-magnetized, optically thin accretion flows (e.g., Yuan & Narayan, 2014). We also assume that the radiating electrons are isotropic in the fluid frame, and that they have a thermal energy distribution. The assumption of thermal electrons has been used extensively for modelling low-luminosity accreting black hole systems such as Sgr A* (e.g., Mościbrodzka et al., 2009; Mościbrodzka & Falcke, 2013; Mościbrodzka et al., 2014; Chan et al., 2009, 2015b,a; Shcherbakov et al., 2012; Shcherbakov & McKinney, 2013).

Non-thermal electrons might also be present in the flow due to the dissipation of energy at shock waves (e.g., Sironi et al., 2015) and magnetic reconnection events (e.g., Sironi & Spitkovsky, 2014). It is expected that these acceleration processes result in a hybrid electron distribution, with a thermal component and a higher energy power-law tail (e.g., Özel et al., 2000). The main effect of such a distribution is an enhancement of the high-energy tails of the synchrotron and inverse Compton (IC) spectral components relative to the purely thermal case. The non-thermal component has a frequency-dependence of (Rybicki & Lightman, 1979)

$$P_\nu \sim \nu^{-(p-1)/2} \tag{2.95}$$

where P_ν is the radiated power per unit frequency, and p is the index of the non-thermal electron distribution. However, the precise contribution from the non-thermal particles depends on a range of poorly-constrained parameters such as the total number and energy of non-thermal electrons, the power-law index p, breaks in the electron distribution due to details of the acceleration process and radiative cooling, as well as uncertainties in the rates and locations of particle acceleration processes in the flow. Therefore, in this thesis, we take a conservative approach and assume a purely thermal electron distribution.

Our treatment of the above radiative processes closely follows that of Dolence et al. (2009). The GRMHD stress-energy tensor (2.45) tracks the total density, pressure, and internal energy of the flow. However, at low accretion rates, Coulomb coupling between the protons and electrons is inefficient and so the plasma is expected to be two-temperature (Yuan & Narayan, 2014). Therefore, when calculating the resulting radiation we must make a separation between the electrons and protons. We assume that each species obeys an ideal gas law $P = nkT$, where P is the pressure, n is the number density, k is Boltzmann's constant, and T is the temperature. We also assume that the plasma is quasi-neutral and set $n = n_e = n_p$, where n_e and n_p are the electron and proton number densities. It is convenient to introduce the proton-to-electron temperature ratio as a free parameter

$$\mathcal{T} = \frac{T_p}{T_e} \tag{2.96}$$

We can then write the gas pressure as $P = P_e + P_p = nkT_e\,(1 + \mathcal{T})$, from which we find the electron temperature

$$T_e = \frac{P}{\rho}\left(\frac{m_e + m_p}{k}\right)\left(\frac{1}{1+\mathcal{T}}\right) \tag{2.97}$$

In subsequent chapters, we discuss various prescriptions for specifying $\mathcal{T}$, as well as the limitations of this approach. In the rest of this section, all quantities refer to the electron gas and so we drop the subscript e.

The Maxwell-Jüttner distribution function for relativistic electrons at temperature $\Theta = kT/mc^2$ is given by

$$\frac{\mathrm{d}n}{\mathrm{d}\gamma} = \frac{n}{\Theta}\frac{\gamma^2\beta}{K_2(\Theta^{-1})}\exp\left(-\frac{\gamma}{\Theta}\right) \tag{2.98}$$

where $\gamma = (1-\beta^2)^{-1/2}$ is the electron Lorentz factor, β is the electron speed in the fluid frame, and K_2 is the modified Bessel function of the second kind. We use the following emission coefficient for thermal synchrotron emission (Dolence et al., 2009; Leung et al., 2011)

$$j_\nu = \frac{\sqrt{2}\pi q^2 n\nu_s}{3cK_2(\Theta^{-1})}\left(X^{1/2} + 2^{11/12}X^{1/6}\right)^2\exp(-X^{1/3}) \tag{2.99a}$$

$$X \equiv \frac{\nu}{\nu_s} \tag{2.99b}$$

$$\nu_s \equiv \frac{2}{9}\left(\frac{qB}{2\pi mc}\right)\Theta^2\sin\theta \tag{2.99c}$$

where q is the electron charge, B is the magnetic field strength, and θ is the angle between the photon wave vector and the magnetic field. The thermal synchrotron self-absorption coefficient is calculated using Kirchoff's law (Rybicki & Lightman, 1979; Dolence et al., 2009)

$$\alpha_\nu = \frac{j_\nu}{B_\nu} \tag{2.100}$$

where

$$B_\nu(T) = \frac{2h\nu^3}{c^2}\frac{1}{e^{h\nu/kT}-1} \tag{2.101}$$

is the Planck function.

The cross section for Compton scattering from a distribution of relativistic electrons is given by (Landau & Lifshitz, 1975; Dolence et al., 2009)

$$\sigma = \frac{1}{n}\int \mathrm{d}^3p\,\frac{\mathrm{d}n}{\mathrm{d}^3p}(1-\mu\beta)\,\sigma_{\mathrm{KN}} \tag{2.102}$$

Here, p is the electron four-momentum, $\mathrm{d}^3p = \mathrm{d}p_1\,\mathrm{d}p_2\,\mathrm{d}p_3$, and μ is the cosine of the angle between the electron momentum and photon momentum in the fluid frame.

The Klein-Nishina cross section, $\sigma_{\rm KN}$, accounts for quantum-electrodynamical corrections to the Thomson cross section, σ_T, when the photon energy in the electron rest frame becomes comparable to mc^2 (Rybicki & Lightman, 1979)

$$\sigma_{\rm KN} = \sigma_T \frac{3}{4\epsilon^2}\left(2 + \frac{\epsilon^2(1+\epsilon)}{(1+2\epsilon)^2} + \frac{\epsilon^2 - 2\epsilon - 2}{2\epsilon}\log(1+2\epsilon)\right) \tag{2.103}$$

Here, σ_T is the Thomson cross section, $\epsilon = \epsilon'\gamma(1-\mu\beta)$ is the photon energy (in units of mc^2) in the electron rest frame, and ϵ' is the photon energy in the fluid frame. The principal effect is a reduction of the scattering cross section for high energy photons. Note that for $\epsilon \ll 1$

$$\sigma_{\rm KN} = \sigma_T\left(1 - 2\epsilon + \mathcal{O}\left(\epsilon^2\right)\right) \tag{2.104}$$

while for $\epsilon \gg 1$

$$\sigma_{\rm KN} = \frac{3}{8}\,\sigma_T\,\epsilon^{-1}\left(\log\left(2\epsilon\right) + \frac{1}{2}\right) \tag{2.105}$$

We use the thermal distribution in equation (2.98) when calculating the Compton cross section (2.102). The scattered photon energy and angle can be determined using the Klein-Nishina differential cross section (Dolence et al., 2009)

$$\frac{2\pi}{\sigma_T}\frac{{\rm d}\sigma_{\rm KN}}{{\rm d}\epsilon_s} = \frac{1}{\epsilon_s}\left(\frac{\epsilon}{\epsilon_s} + \frac{\epsilon_s}{\epsilon} - 1 + \cos^2\theta_s\right) \tag{2.106}$$

where ϵ_s is the energy of the scattered photon, and θ_s is the scattering angle in the electron frame.

Chapter 3

Jet Signatures in the Spectra of Accreting Black Holes

3.1 Overview

Jets are observed as radio emission in active galactic nuclei and during the low/hard state in XRBs, but their contribution at higher frequencies has been uncertain. In this chapter, we study the dynamics of jets in XRBs using the GRMHD code `HARM`, and calculate the high-energy spectra and variability properties using a general-relativistic radiative transport code based on `grmonty`. We find the following signatures of jet emission (i) a significant γ-ray peak above $\sim 10^{22}$ Hz, (ii) a break in the optical/UV spectrum, with a change from $\nu L_\nu \sim \nu^0$ to $\nu L_\nu \sim \nu$, followed by another break at higher frequencies where the spectrum roughly returns to $\nu L_\nu \sim \nu^0$, and (iii) a pronounced synchrotron peak near or below $\sim 10^{14}$ Hz indicates that a significant fraction of any observed X-ray emission originates in the jet. We investigate the variability during a large-scale magnetic field inversion in which the Blandford-Znajek jet is quenched and a new transient hot reconnecting plasmoid is launched by the reconnecting field. The ratio of the γ-rays to X-rays changes from $L_\gamma/L_X > 1$ in the BZ jet to $L_\gamma/L_X < 1$ during the launching of the transient plasmoid.

This chapter is based on work published in O' Riordan et al. (2016a).

3.2 Introduction

As discussed in chapter 1, the contribution of jets to the observed high-energy emission in XRBs remains a topic of active research and debate. In this chapter, we are interested in identifying the observational signatures of jet emission. Since our goal is to study jets, we use GRMHD simulations of RIAFs, supplied by the `HARM` code, as input for our post-processing calculation. We perform our radiative transport calculations for both MAD and non-MAD RIAFs, and find significant differences in the resulting spectra. Furthermore, we make a distinction between jet and disk emission, and keep track of whether or not photons had some interaction (emission or scattering) with the jet before escaping the system. This allows us to determine the jet contribution to the spectrum, and identify unique observational signatures of jets.

This chapter is organised as follows. In Section 3.3 we briefly describe our 3D GRMHD simulations and radiative transport code. In Section 3.4 we present our results, showing the observational jet signatures and variability properties of the jet and disk emission. In Section 3.5 we discuss our findings and summarize our main results.

3.3 Model

3.3.1 GRMHD simulation

We are interested in jets and so we focus on RIAFs, since these are likely necessary for jet launching by the BZ mechanism (Livio et al., 1999; Meier, 2001; Avara et al., 2016). In this case, radiation is dynamically unimportant and the evolution is well described by standard GRMHD codes. We use the `HARM` code (Gammie et al.,

2003; McKinney & Gammie, 2004), which evolves the GRMHD equations using a conservative, shock-capturing scheme. For our MAD model, we choose the fiducial model, A0.94BfN40, from McKinney et al. (2012) in which the magnetic field has saturated near the black hole. In this magnetically choked accretion flow, the black hole magnetosphere compresses the inflow such that it becomes geometrically thin and the standard magneto-rotational instability is suppressed. The jet power in the BZ model is given by (Blandford & Znajek, 1977; Tchekhovskoy et al., 2010; Yuan & Narayan, 2014)

$$P_{\rm BZ} = \frac{\kappa}{4\pi c}\Phi^2\Omega_H^2 \tag{3.1}$$

where Φ is the magnetic flux threading the horizon, $\Omega_H = ac/2r_H$ is the angular velocity of the horizon, and $\kappa \approx 0.05$ is a dimensionless coefficient which depends weakly on the magnetic field geometry. The horizon radius, r_H, is given by $r_H = (1+\sqrt{1-a^2})r_g$, where a is the dimensionless black-hole spin, $r_g = GM/c^2$, and M is the mass of the black hole. Thus, the highly magnetized state over most of the horizon (see Figure 3.1), and large black-hole spin ($a = 0.9375$), are optimal for the BZ mechanism to generate powerful, relativistic jets (Tchekhovskoy et al., 2011; McKinney et al., 2012).

The initial mass distribution is an isentropic hydroequilibrium torus (Fishbone & Moncrief, 1976; Gammie et al., 2003) with the inner edge at $r = 10r_g$ and pressure maximum at $r = 100r_g$. The magnetic field has poloidal geometry with multiple loops of alternating polarity for inducing magnetic field inversion/annihilation. These field inversions quench and relaunch magnetically dominated BZ jets (see Section 3.4.2.1).

The jet forms as a highly magnetized, low density funnel region along the spin axis of the black hole. In the left panel of Figure 3.1 we show snapshots of the electron number density n, magnitude of the magnetic field B, and dimensionless electron temperature $\Theta \equiv kT_e/mc^2$, at $t = 26548r_g/c$. These plots are scaled to the low/hard state in XRBs, with a black hole mass $M = 10M_\odot$ and accretion rate $\dot{M} = 10^{-5}\dot{M}_{\rm Edd}$, where $\dot{M}_{\rm Edd}$ is the Eddington accretion rate defined as $\dot{M}_{\rm Edd} = L_{\rm Edd}/\left(0.1c^2\right)$ (see e.g., Narayan & McClintock, 2008). The electron temperature

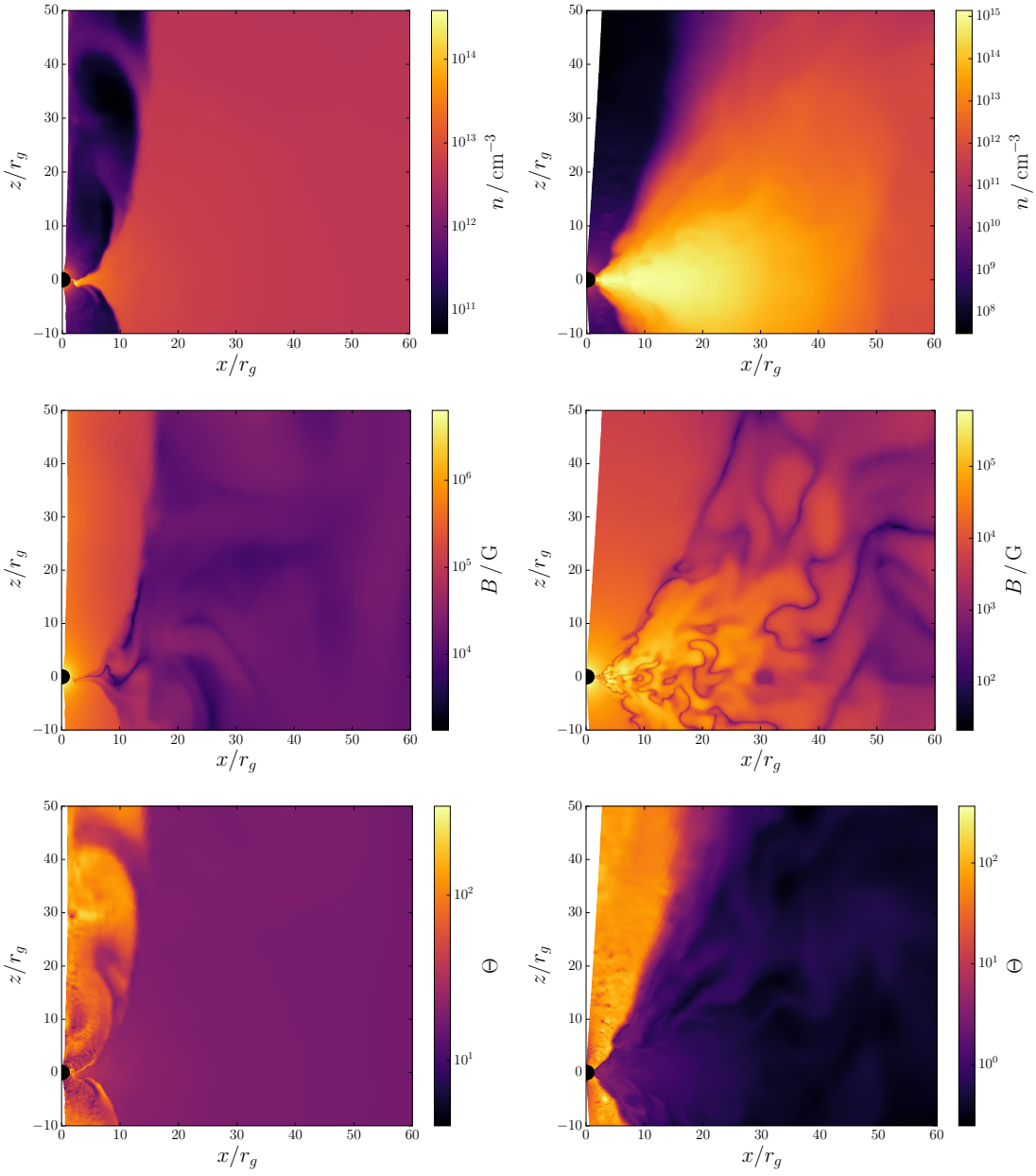

FIGURE 3.1: The left panels show the electron number density, magnetic field strength, and electron temperature, close to the black hole, at $t = 26548 r_g/c$, in our MAD model. The inner $r \lesssim 10 r_g$ of the disk is compressed by the black hole magnetosphere. The disk itself is geometrically thick, with approximately uniform density out to the boundary. The jet is visible as a lower density funnel region. The density enhancements in the jet are the result of QPOs driven by instabilities at the jet-disk interface. The jet region is highly magnetized, with $B \sim 10^6 - 10^7$G. The right panels show a snapshot of the fluid properties close to the black hole, at $t = 4000 r_g/c$, in our non-MAD model. The inner disk is geometrically thicker and cooler than in the MAD case.

shown corresponds to a proton-to-electron temperature ratio of $T_p/T_e = 10$ (see Section 3.3.2.1). The inner $r \lesssim 10r_g$ of the disk is compressed by the black hole magnetosphere. The density enhancements in the jet are due to instabilities at the jet-disk interface (see Section 3.4.2.2). The horizon and funnel regions are both highly magnetized. We use the ratio of the magnetic and rest-mass energy densities to define the jet, i.e. where $b^2/\rho c^2 \geq \xi$, for some constant ξ. Here, ρ is the rest mass density of the gas, and $b^2 = b^\mu b_\mu$, where b^μ is the magnetic field four-vector. The precise value of ξ is somewhat arbitrary and depends on the particular simulation. We find that $\xi = 0.5$ gives a reasonable distinction between the jet and disk in our simulations.

It is also possible to distinguish between the jet, disk, and magnetized wind. The wind can be defined roughly by the condition that $b^2/\rho c^2 < \xi$ and $\beta_p < 2$ (McKinney et al., 2012), where $\beta_p = p_{\rm gas}/p_{\rm mag}$ is the ratio of gas and magnetic pressures. The disk then corresponds to the region with $b^2/\rho c^2 < \xi$ and $\beta_p \geq 2$. In our MAD simulation, the disk is geometrically very thick and maintains approximately uniform density to the boundary, so the wind is limited to a small part of the fluid at the jet-disk interface. Therefore, for our purposes, we choose only to distinguish between the disk and funnel regions.

The simulation runs for a total time of $t_f = 26548\, r_g/c$ and reaches a quasi-steady state by time $t \approx 8000 r_g/c$. A snapshot of the fluid data is saved every $\Delta t = 4r_g/c$. Modified spherical coordinates are used, with resolution $N_r \times N_\theta \times N_\phi = 272 \times 128 \times 256$. This simulation is the highest resolution, longest duration 3D simulation of a MAD configuration to date. The grid extends to a maximum radius of $R_{\rm out} = 26000 r_g$. In order to focus on the dynamics at small radii while avoiding numerical reflections off the outer boundary, the resolution is concentrated near the black hole, with a transition at $r = 500 r_g$ to a much sparser grid (see McKinney et al., 2012, for details). We limit our analysis to the inner $r = 200 r_g$, which corresponds to 194 cells in the radial direction. Coordinate singularities along the poles can cause further numerical difficulties and so we exclude cells near the poles from our radiative transport calculations. This can be seen as an excised region along the z-axis in Figure 3.1.

The jet in our MAD simulation is highly collimated by pressure support from the geometrically very thick disk, and remains nearly cylindrical out to the boundary at $r = 200r_g$. For comparison, we checked our results against the A0.99N100 model from McKinney et al. (2012). This model is a MAD RIAF and is qualitatively similar to the fiducial model, however, the disk is geometrically thinner. We find similar spectra in both cases, indicating that our results are not just peculiarities of the very thick disk.

For our non-MAD model, we use the dipole model of McKinney & Blandford (2009). In this simulation, a MAD state does not develop and the accretion is driven by the magneto-rotational instability. In the right panel of Figure 3.1 we show snapshots of the electron number density, magnetic field, and electron temperature at $t = 4000r_g/c$ in our non-MAD model. The black-hole magnetosphere does not disrupt the inner accretion flow in this case, and so the inner disk is geometrically thicker than in the MAD simulation. While the jet efficiency in our MAD simulation is > 100 per cent, the corresponding efficiency in our non-MAD simulation is only about 1 per cent, even with a large black-hole spin of $a = 0.92$.

The initial disk torus has inner edge at $r = 6r_g$, pressure maximum at $r = 12r_g$, and contains a single magnetic field loop. The simulation runs for a total time of $t_f = 5000r_g/c$ and reaches a quasi-steady state by time $t \approx 3000r_g/c$. The grid resolution is $N_r \times N_\theta \times N_\phi = 256 \times 128 \times 32$, and warps to follow the disk at small radii and the jet at large radii. The outer boundary is located at $R_{\rm out} = 1000r_g$. Again, we limit our calculations to the inner $r = 200r_g$ and excise cells near the poles. We distinguish between the jet and disk using the same condition on $b^2/\rho c^2$ as in the MAD case.

3.3.1.1 Density floors

The `HARM` code, as well as many other GRMHD codes (e.g., `WhiskyMHD`, Giacomazzo & Rezzolla 2007; `HARM3D`, Noble et al. 2009; `KORAL`, Sądowski et al. 2013; `IllinoisGRMHD`, Etienne et al. 2015; `Athena++`, White et al. 2016), can not handle a vacuum. If the rest-mass density ρ, or the internal energy density u become too

small in comparison with b^2, truncation errors in the evolution can lead to large fractional errors in these quantities. To avoid this, GRMHD codes use density "floors", which effectively inject mass into the system in regions where these floors are activated.

In the simulations considered here, the internal energy is chosen to enforce $u/\rho c^2 \leq 50$, then ρ is chosen with the conditions that $b^2/\rho c^2 \leq 50$ and $b^2/u \leq 10^3$. We find numerically that these floors are only activated in the central regions of the highly-magnetized, low-density funnel. McKinney & Gammie (2004) showed that, as long as $b^2/\rho c^2 \gg 1$, the flow is approximately force-free (with maximum deviations of $\sim$ few %) and so the dynamics of the electrodynamic field in the funnel is unaffected by the injection.

Artificial mass injection primarily occurs near $r \sim 10 r_g$. At larger radii, this mass injection no longer occurs and the solution becomes a valid MHD solution, as shown in McKinney (2006). The only effect of the floors on the dynamics is therefore to set a rough upper limit on the bulk Lorentz factor of $\Gamma_{\rm max} = b^2/\rho c^2$ at large radii. In this chapter, we limit our analysis to the inner $r = 200\, r_g$, where the Lorentz factor of the flow is much less than the local value of $b^2/\rho c^2$. Therefore, the values chosen for the floors do not have any effect on the dynamics of the jet in the simulated region.

Although the artificially injected material has no effect on the dynamics, it is potentially very hot and so could modify the predicted spectra by overproducing high-energy emission. Physically-motivated estimates of mass injection in funnel region suggest that the electron number density is in fact very low (Mościbrodzka et al., 2011; Levinson & Rieger, 2011) and so should not contribute significantly to the emission (Mościbrodzka & Falcke, 2013; Mościbrodzka et al., 2014).

To ensure that the injected mass does not affect the resulting spectra, we remove this material before performing the radiative transport calculation on our MAD and non-MAD models.

3.3.2 Radiative transport

We calculate the spectra and variability properties of the low/hard state in XRBs using a general relativistic radiative transport code based on the freely available `grmonty` (Dolence et al., 2009). This code uses a post-processing approach for calculating the spectra and relies on an external fluid model to supply the rest-mass density ρ, internal energy density u, fluid four-velocity u^μ, and magnetic field four-vector b^μ, at every point in the grid. We interpolate these quantities to arbitrary points as needed. We modify the original code to work with general 3D `HARM` data as input, and to allow for different temperature prescriptions in the disk and in the jet (see Section 3.3.2.1).

As described in Chapter 2, the spectra are calculated assuming synchrotron emission, self-absorption, and Compton scattering from a thermal distribution of relativistic electrons. Introducing radiation breaks the scale-free nature of the GRMHD data. We set the length and time scales by specifying the black hole mass M. The appropriate scales are then the gravitational radius, r_g, and the light crossing time, $t_g = r_g/c$. The fluid mass/energy unit $\mathcal{M}$ must also be specified (this is not set by M because the fluid mass is $\ll M$). Using these units, the `HARM` data can be scaled to a particular system, for example, the mass density is set as $\rho = (\mathcal{M}/r_g^3)\widetilde{\rho}$, where $\widetilde{\rho}$ is the dimensionless mass density given by the `HARM` code. Note that once M is chosen, the accretion rate at a given radius is set by $\mathcal{M}$ via

$$\dot{M} = \left| \int \sqrt{-g}\, \mathrm{d}x^\theta\, \mathrm{d}x^\phi \rho u^r \right| \tag{3.2}$$

For our purposes, we set $M = 10M_\odot$ and choose $\mathcal{M}$ such that the accretion rate at the black-hole horizon is $\dot{M} = 10^{-5}\dot{M}_{\mathrm{Edd}}$.

By tracking photons individually, we can unambiguously determine the jet contribution to the spectrum. We track $\sim 10^8$ photons to an outer radial boundary of $r = 200r_g$. The choice of this boundary is discussed in Section 3.3.1 and has little effect on the results as most of the high-energy emission originates close to the black hole. While relativistic Doppler effects are fully accounted for by the

code, we find that the effects on the resulting spectra are small since the jets in our simulations are only mildly relativistic at small radii.

For computational simplicity, we use a "fast light" approximation in which the fluid data is treated as time-independent during the radiative transport calculation. This approximation may break down in regions where the light crossing time is comparable to the dynamical time, however, we perform our post-processing calculation only after the fluid simulation has reached a quasi-steady state and so we expect this to be a reasonable approach. Furthermore, Shcherbakov et al. (2012) performed both time-independent and fully time-dependent radiative transport calculations in the context of Sgr A*, and found good agreement in most cases.

3.3.2.1 Disk and jet electron temperatures

The details of the electron thermodynamics in RIAFs have not been determined. A common approach is to assume that the electron temperature is some constant fraction of the proton temperature, and to use this ratio as a free parameter (Mościbrodzka et al., 2009). Although more sophisticated models are being developed (Ressler et al., 2015; Foucart et al., 2016), there are still many parameters whose values are unknown. Because of these uncertainties, we use the simple assumption of a constant proton-to-electron temperature ratio $\mathcal{T} \equiv T_p/T_e$. However, since differences in density and magnetization in the disk and jet can lead to different cooling rates for the electrons in these regions, we vary this temperature ratio independently in these regions (Chan et al., 2015b; Ressler et al., 2015). We define a proton-to-electron temperature ratio $\mathcal{T}_d$ in the disk where $b^2/\rho c^2 < 0.5$, and a ratio $\mathcal{T}_j$ in the jet where $b^2/\rho c^2 \geq 0.5$.

The values of these ratios depend on poorly understood electron thermodynamics. However, assuming that (i) the dissipation of turbulence mainly heats the protons, (ii) the cooling time for the electrons is shorter than that of the protons, and (iii) the electron cooling time is shorter than the timescale for significant energy exchange between the electrons and protons, we expect these temperature ratios to be greater than unity (Yuan & Narayan, 2014; Chan et al., 2015b). Furthermore,

Model	$\mathcal{T}_d$	$\mathcal{T}_j$
1	3	3
2	10	10
3	30	30
4	3	10
5	3	30
6	10	30
7	10	3
8	30	3
9	30	10

TABLE 3.1: List of MAD model proton-to-electron temperature ratios.

because of the similarities between AGN and the low/hard state in XRBs, we assume that the physics of electron heating and cooling is the same across these systems. We therefore choose a range of values of $\mathcal{T}_d$ and $\mathcal{T}_j$ motivated by fitting to Sgr A* and M87, since these are the only sources whose spectra have been fitted to constrain these parameters (Mościbrodzka et al., 2009; Mościbrodzka & Falcke, 2013; Mościbrodzka et al., 2014; Chan et al., 2015b; Mościbrodzka et al., 2016).

3.4 Results

3.4.1 Jet signatures

3.4.1.1 MAD model

For our MAD model, we calculate spectra for the nine temperature models listed in Table 3.1. In Figure 3.2 we show the spectra calculated with $\mathcal{T}_d = \mathcal{T}_j$. The distinction between the jet and disk contributions is defined such that the "jet" (short dashes) component corresponds to the contribution from photons which either originated in the jet or scattered in the jet before escaping. The "disk" (long dashes) component corresponds to photons which originated in the disk and escaped without scattering in the jet (possibly scattering in the disk before leaving the system).

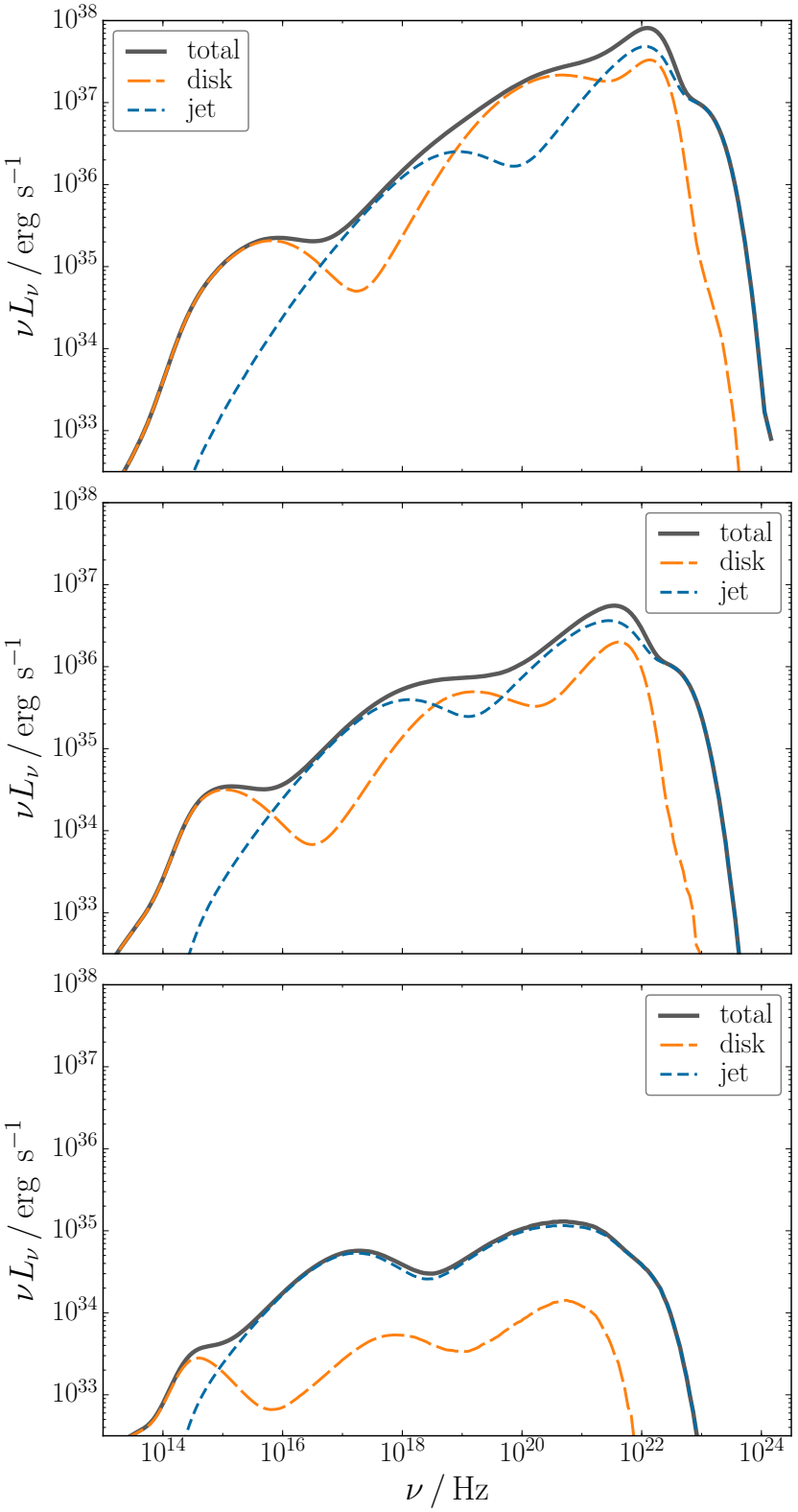

FIGURE 3.2: MAD model spectra with $\mathcal{T}_d = \mathcal{T}_j$. From top to bottom, these were calculated with $(\mathcal{T}_d, \mathcal{T}_j) = (3, 3), (10, 10), (30, 30)$, respectively. The disk contribution dominates mainly around 10^{15} Hz, while the jet contributes significantly in the X-rays and γ-rays.

The middle panel shows the spectrum calculated with $(\mathcal{T}_d, \mathcal{T}_j) = (10, 10)$. This spectrum qualitatively captures the main spectral features present in most models, which we describe below. Both the "disk" and "jet" components have three peaks. The peak in the "disk" component at $\sim 10^{15}$ Hz is due to synchrotron emission from the disk, while the two higher peaks at $\sim 10^{19}$ Hz and $\sim 10^{22}$ Hz result from single and double synchrotron self-Compton, respectively. The peak in the "jet" component at $\sim 10^{18}$ Hz is due to synchrotron emission from the jet, while the peak at $\sim 10^{22}$ Hz corresponds to synchrotron photons from the jet which scattered once in the disk before escaping. The peak at $\sim 10^{23}$ Hz is due to single scattering in the jet. In all models with $\mathcal{T}_d = \mathcal{T}_j$, the disk dominates in the optical, while the jet contributes significantly to the X-rays and γ-rays. The disk contributes to the hard X-rays in models with $\mathcal{T}_d < 30$. In these models, the disk emission peaks around 10^{22} Hz, and decays rapidly above this. The emission decays since the photons have been scattered up to the same temperature as the electrons in the disk. In what follows, we will refer to this frequency as the "saturation frequency", $\nu_{\rm sat}$.

It is interesting to note that, although all these models have $\mathcal{T}_d = \mathcal{T}_j$, there are differences in the resulting spectra. This is due to the strong dependence of the scattering on the electron temperature. The synchrotron peak depends on the temperature as $(\nu j_\nu)_{\rm syn} \sim \Theta^2$, while the inverse Compton peak goes like $(\nu j_\nu)_{\rm IC} \sim y(\nu j_\nu)_{\rm syn} \sim \Theta^4$. Here, y is the Compton y parameter given by $y = 16\Theta^2\tau$ (Rybicki & Lightman, 1979), and τ is the optical depth. We have assumed that the fluid is optically thin, and that the electrons are ultrarelativistic, $\gamma \gg 1$, and have a thermal distribution.

In Figure 3.3 we show spectra calculated with $\mathcal{T}_d < \mathcal{T}_j$. The features in the "disk" component are similar to those in Figure 3.2, with a synchrotron peak around $\sim 10^{15}$ Hz, and two higher energy peaks due to single and double synchrotron self-Compton. The "jet" component shows a synchrotron peak at $\sim 10^{18}$ Hz, and a peak at 10^{22} Hz corresponding to photons which originated in the jet and scattered once in the disk before escaping. The disk dominates most of the spectra in this

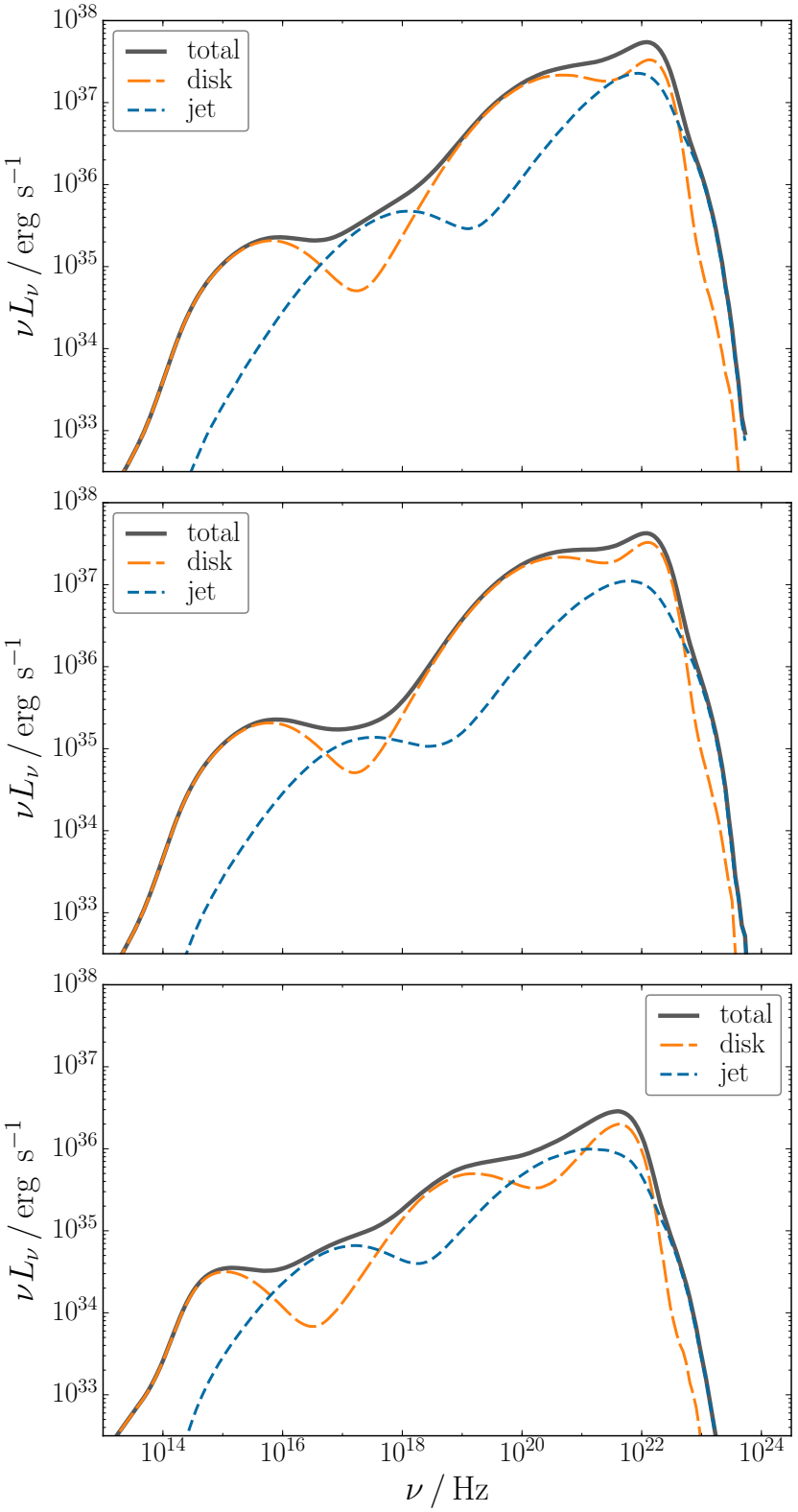

FIGURE 3.3: Same as Figure 3.2 but for models with $\mathcal{T}_d < \mathcal{T}_j$. From top to bottom $(\mathcal{T}_d, \mathcal{T}_j) = (3, 10), (3, 30), (10, 30)$, respectively. The disk dominates the spectra at all wavelengths in this case. However,there are frequencies where the jet contributes significantly.

case. The high-energy γ-ray peak, present in models with $\mathcal{T}_d = \mathcal{T}_j$, is absent or obscured by the hotter disk contribution.

In Figure 3.4 we show spectra calculated with $\mathcal{T}_d > \mathcal{T}_j$. In this case, the jet dominates most of the spectrum, with a small contribution from the disk around the optical band. The peak around $\sim 10^{15}$ Hz is due to synchrotron from the disk, while the peak at $\sim 10^{19}$ Hz is synchrotron emission from the jet. The third peak, at $\sim 10^{21}$ Hz, again corresponds to photons which were emitted in the jet and scattered once in the disk. The peak in the γ-rays around 10^{23} Hz is due to scattering in the jet.

The locations of the synchrotron and saturation peaks provide a wealth of information about the fluid properties in the jet and in the disk. The ratio of the jet and disk synchrotron peak frequencies depends on the temperatures and magnetic fields as $\nu_{\mathrm{syn},j}/\nu_{\mathrm{syn},d} \sim \Theta_j^2 B_j / \Theta_d^2 B_d$. The saturation frequency is simply proportional to the electron temperature, $\nu_{\mathrm{sat}} \sim \Theta$. Therefore, the ratio of jet and disk magnetic fields can be estimated from the spectra as

$$\frac{B_j}{B_d} \sim \left(\frac{\nu_{\mathrm{syn},j}}{\nu_{\mathrm{syn},d}}\right)\left(\frac{\nu_{\mathrm{sat},d}}{\nu_{\mathrm{sat},j}}\right)^2 \tag{3.3}$$

For example, the top panel of Figure 3.4 shows $\nu_{\mathrm{sat},d}/\nu_{\mathrm{sat},j} \sim 1/30$ and $\nu_{\mathrm{syn},j}/\nu_{\mathrm{syn},d} \sim 10^4$, which corresponds to a magnetic field ratio of $B_j/B_d \sim 10$. This analysis is independent of the temperature model, however, we have used the fact that the jet in our simulation is only mildly relativistic.

While separating the spectrum into jet and disk components is useful for identifying their contributions, in reality, this decomposition is not so straightforward. Therefore, we are interested in identifying signatures of jet emission in the composite spectrum.

In all our MAD calculations, the highest energy emission is produced by inverse Compton scattering of synchrotron photons. Therefore, the electron temperature sets an upper limit on the high energy emission. In all models with $\mathcal{T}_d \geq \mathcal{T}_j$ (Figures 3.2 and 3.4) the jet electrons are one or two orders of magnitude hotter

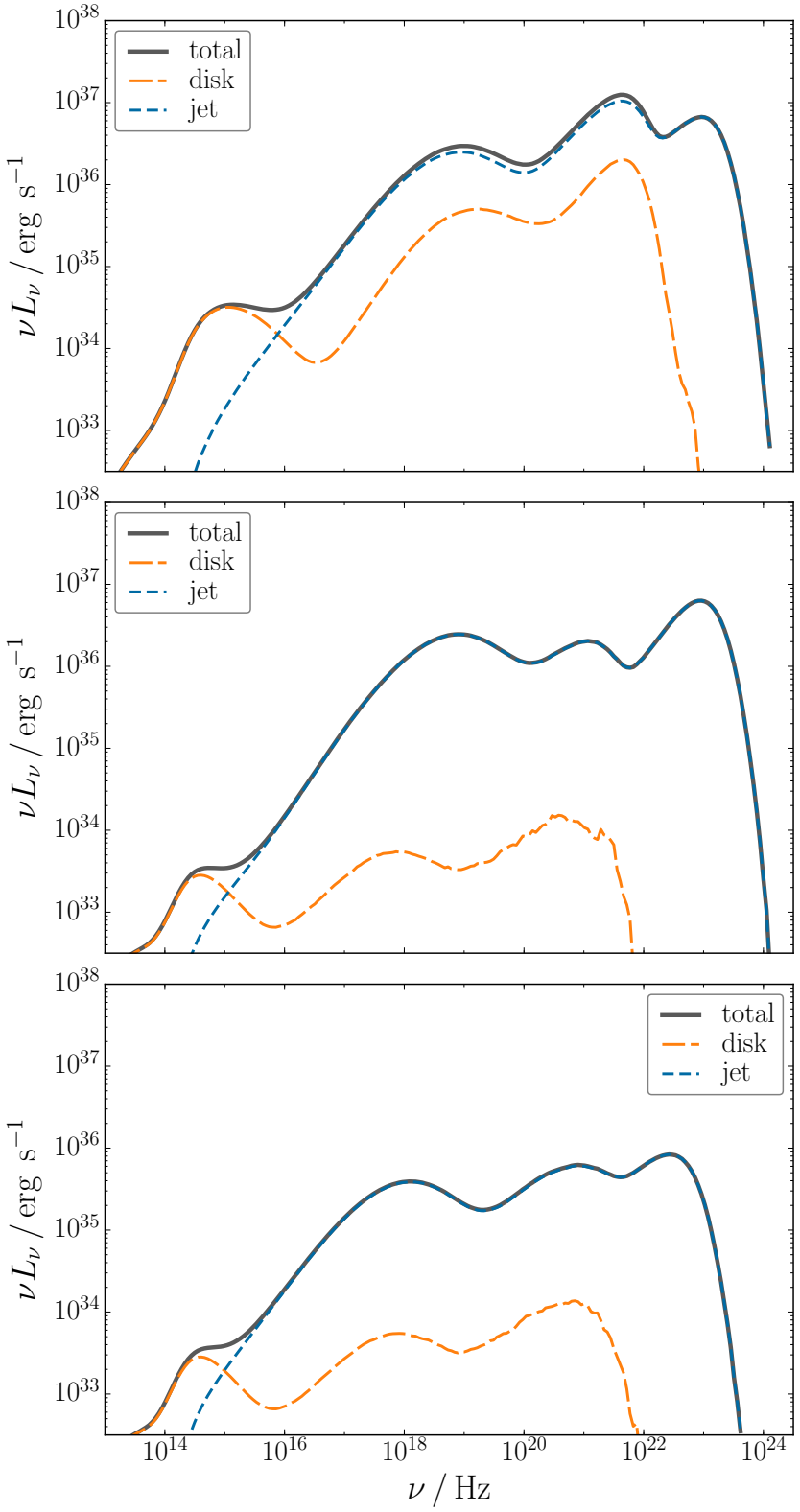

FIGURE 3.4: Same as Figure 3.2 but for models with $\mathcal{T}_d > \mathcal{T}_j$. From top to bottom $(\mathcal{T}_d, \mathcal{T}_j) = (10, 3), (30, 3), (30, 10)$, respectively. The jet dominates everything above $\sim 10^{16}$ Hz.

than those in the disk. Therefore, we expect the highest energy emission to come from the jet. This is clearly visible in the spectra as a γ-ray peak in the jet component around $\sim 10^{23}\,\mathrm{Hz}$, well above the highest energy disk contribution. This feature is absent in disk-dominated spectra, i.e., those with $\mathcal{T}_d < \mathcal{T}_j$ (see Figure 3.3). We conclude that this high-energy feature could be a good indicator of jet emission.

Another possible signature of jet emission occurs in regions where the spectra change from disk to jet dominated. The overlapping jet and disk components tend to smooth out parts of the spectrum which would otherwise be much steeper. Most of the spectra from our MAD simulation show roughly flat ($\nu L_\nu \sim \nu^0$) regions, followed by a break where the spectrum changes to $\nu L_\nu \sim \nu$. This can be seen clearly in the spectra in Figure 3.4, with breaks around $\sim 10^{15}\,\mathrm{Hz}$. There is a second break in the spectrum around $\sim 10^{18}\,\mathrm{Hz}$, where it returns roughly to $\nu L_\nu \sim \nu^0$. This second break is followed by "wiggles" in spectrum, with variations in the luminosity of a factor of a few. These features are less clear in models where the spectra are almost completely dominated by disk emission ($\mathcal{T}_d < \mathcal{T}_j$). The breaks are due to the combined effect of the jet and disk contributions, and so are a clear indication of the presence of jet emission.

3.4.1.2 Non-MAD model

For our non-MAD model, we use the same black hole mass as in our MAD calculations. Since we are interested in signatures of jets, we choose temperature models which potentially show a substantial jet contribution, i.e., those with $\mathcal{T}_d > \mathcal{T}_j$. For comparison with our MAD model, we choose $\dot{M} = 10^{-5}\dot{M}_{\mathrm{Edd}}$. In this case, the spectra are primarily dominated by disk emission and so we also investigate a lower accretion rate of $\dot{M} = 10^{-6}\dot{M}_{\mathrm{Edd}}$.

In Figure 3.5 we show spectra from our non-MAD model, calculated with $(\mathcal{T}_d, \mathcal{T}_j) = (30, 3)$ and accretion rates of $10^{-6}\dot{M}_{\mathrm{Edd}}$ (top panel) and $10^{-5}\dot{M}_{\mathrm{Edd}}$ (bottom panel). These spectra show pronounced synchrotron peaks from the disk at $\sim 10^{14}\,\mathrm{Hz}$ and $\sim 10^{15}\,\mathrm{Hz}$. In the model with $\dot{M} = 10^{-6}\dot{M}_{\mathrm{Edd}}$, the jet component contributes

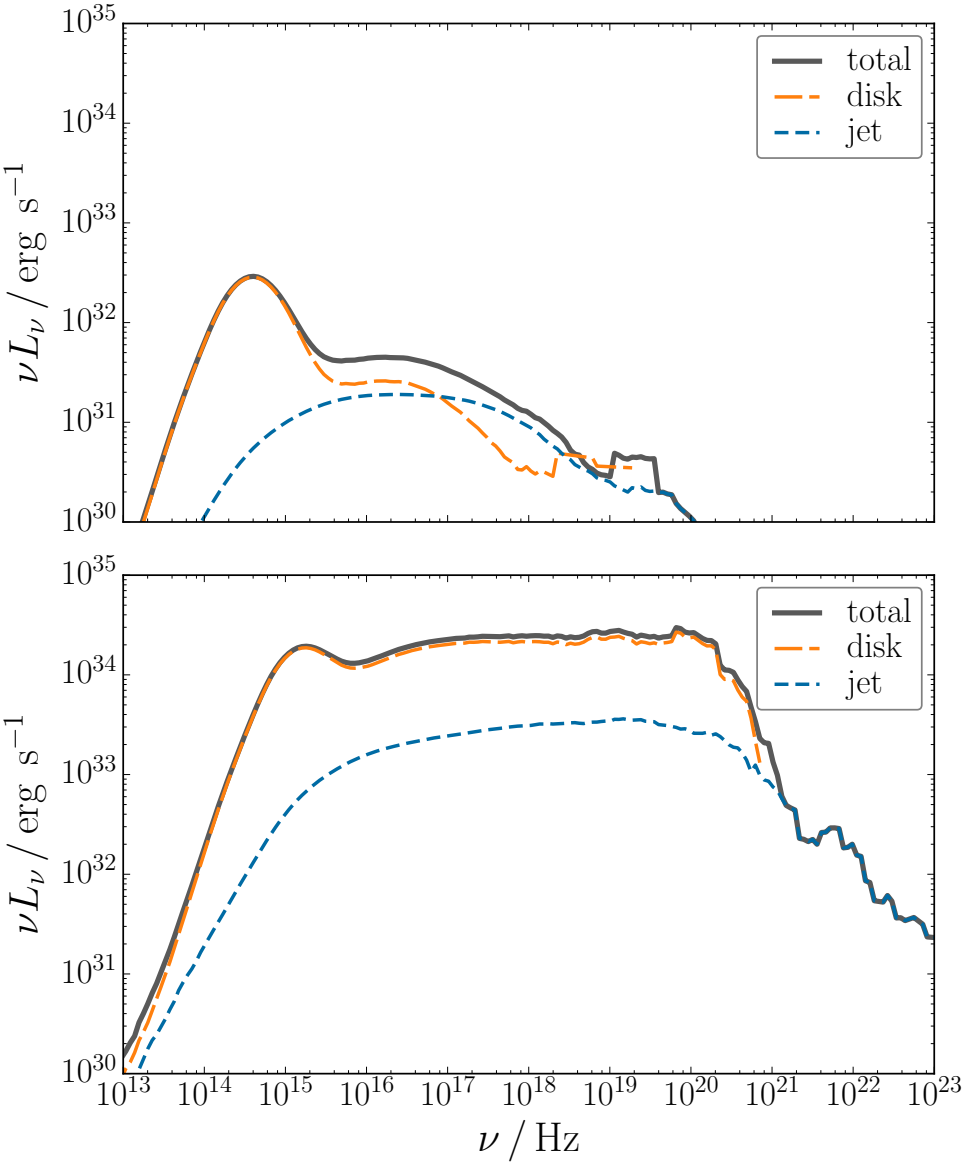

FIGURE 3.5: Non-MAD model spectra calculated with $(\mathcal{T}_d, \mathcal{T}_j) = (30, 3)$. The top panel shows the spectrum with $\dot{M} = 10^{-6}\dot{M}_{\rm Edd}$, while the bottom panel has $\dot{M} = 10^{-5}\dot{M}_{\rm Edd}$. High-energy γ-ray emission is clearly produced by the jet. In models where the disk synchrotron peaks near or below $\sim 10^{14}$ Hz, the jet contributes significantly to the X-rays. In models where this synchrotron peak is near or above $\sim 10^{15}$ Hz, the X-rays are dominated by emission from the disk. The higher energy emission is noisy due to poor photon statistics.

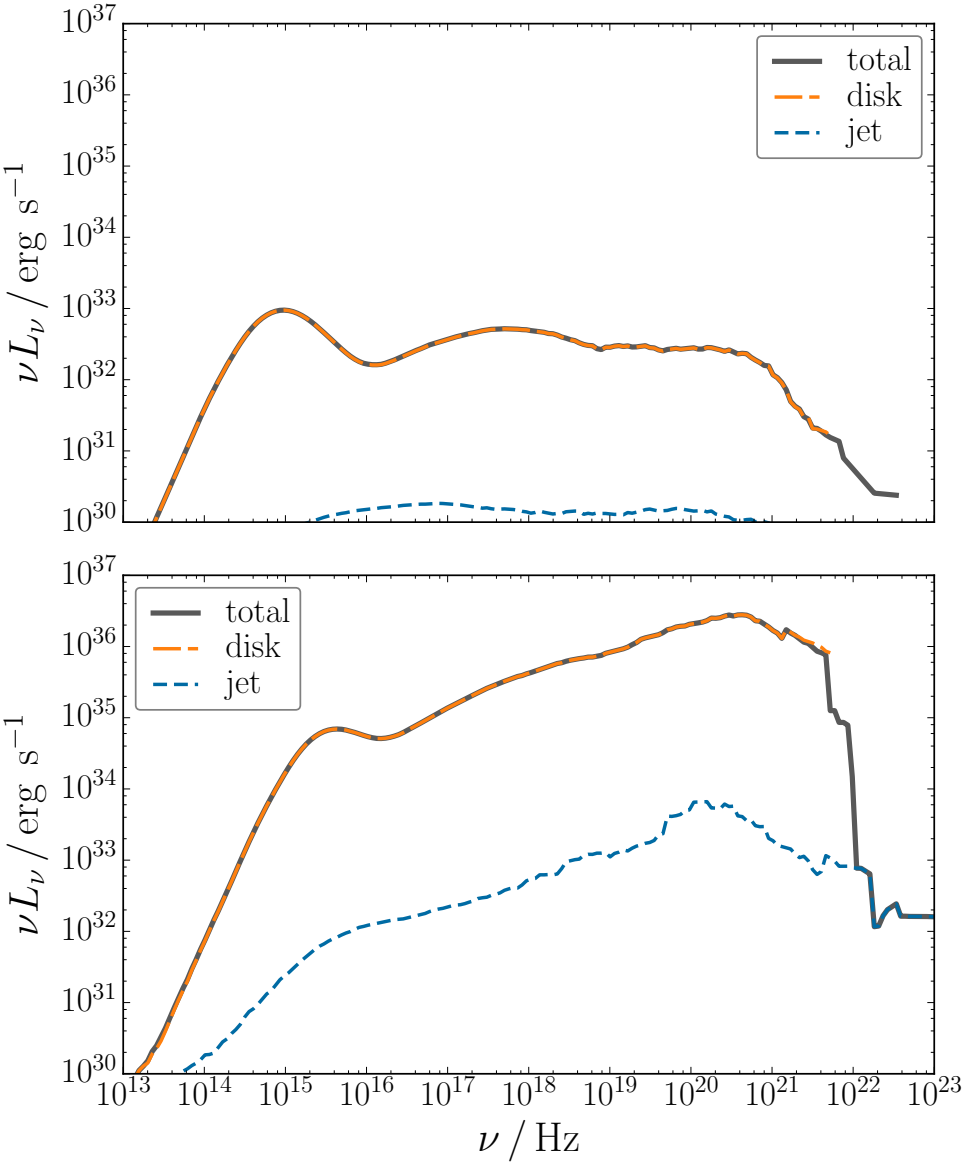

FIGURE 3.6: Non-MAD model spectra calculated with $(\mathcal{T}_d, \mathcal{T}_j) = (10, 3)$. The top panel shows the spectrum with $\dot{M} = 10^{-6}\dot{M}_{\rm Edd}$, while the bottom panel has $\dot{M} = 10^{-5}\dot{M}_{\rm Edd}$. Synchrotron emission and scattering from the disk dominate most of the spectrum. Similar to the MAD case, the high-energy γ-ray emission above $\sim 10^{22}$ Hz is due to scattering in the jet.

significantly to the X-rays, while in the model with $\dot{M} = 10^{-5}\dot{M}_{\rm Edd}$, the disk dominates at all frequencies up to the γ-rays. Interestingly, although the disk component dominates most of the spectrum in the $\dot{M} = 10^{-5}\dot{M}_{\rm Edd}$ case, there is significant γ-ray emission from the jet at and above $\sim 10^{22}$ Hz. As in our MAD model, this is due to scattering in the jet and is located at higher frequencies than the disk saturation frequency, i.e., above where the disk emission decays. From the top panel of Figure 3.5, we can conclude that a pronounced synchrotron peak at or below $\sim 10^{14}$ Hz, which can be attributed to the disk, indicates that any observed X-ray emission is likely due to emission from the jet.

In Figure 3.6 we show spectra calculated with the same accretion rates as in Figure 3.5, but with $(\mathcal{T}_d, \mathcal{T}_j) = (10, 3)$. In this case, there is a peak at $\sim 10^{15}$ Hz due to synchrotron emission from the disk, while the rest of the spectrum up to $\sim 10^{21}$ Hz is dominated by synchrotron self-Compton from the disk. Again, the highest-energy γ-rays are produced by scattering in the jet. Therefore, this is a robust signature of jet emission which is independent of whether the accretion flow is MAD or non-MAD. It is interesting to note that the X-rays from our MAD model are dominated by synchrotron photons from the jet, while the X-rays are produced by scattering in the disk in our non-MAD model (see Figures 3.4 and 3.6).

3.4.2 MAD model variability

In this Section, we investigate jet variability in our MAD model, and so choose a temperature model which produces significant jet emission. In what follows we set $\mathcal{T}_d = 10$, and $\mathcal{T}_j = 3$.

3.4.2.1 Magnetic field inversion

The initial magnetic field in our MAD model contains multiple poloidal field loops, with adjacent field loops having opposite polarity. Igumenshchev (2009) argued that the accretion of such oppositely polarized loops could be responsible for the

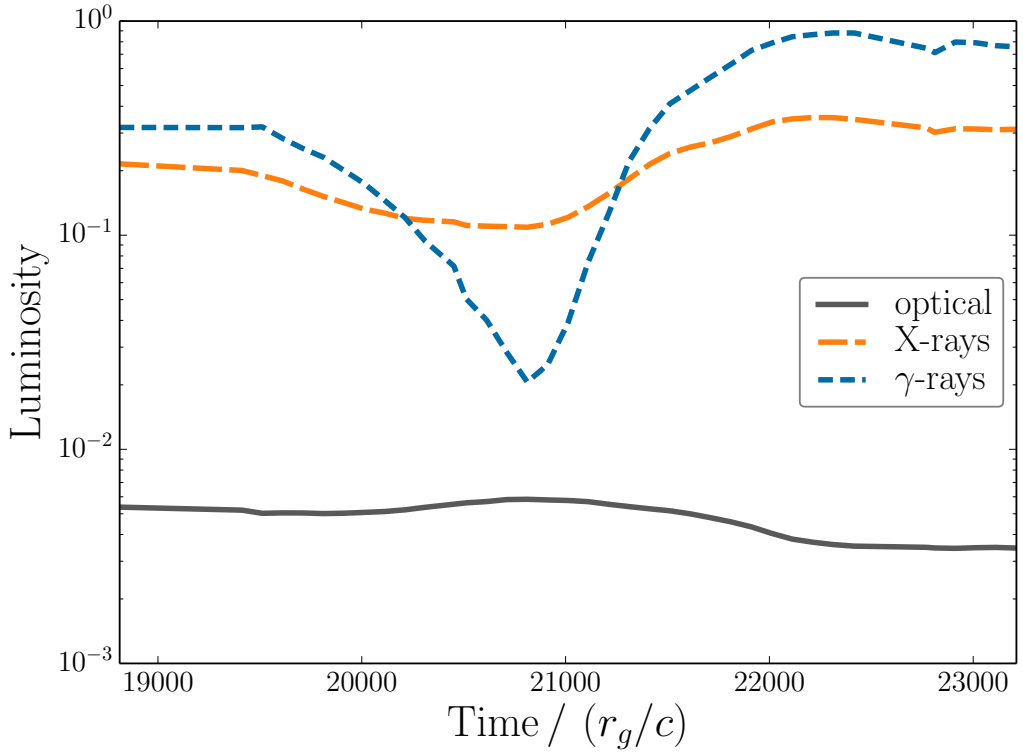

FIGURE 3.7: Optical, X-ray, and γ-ray variability during a global magnetic field inversion. These lightcurves were calculated with $\mathcal{T}_d = 10$, $\mathcal{T}_j = 3$. The γ-ray luminosity varies by nearly two orders of magnitude, and the ratio of the γ-ray to X-ray luminosities, L_γ/L_X, varies such that $L_\gamma/L_X > 1$ in the steady BZ jet and $L_\gamma/L_X < 1$ during the transient outburst. Note that we have normalized the luminosity by its maximum value after the outburst.

observed state transitions in XRBs. As discussed in Dexter et al. (2014), the polarity inversion causes large-scale magnetic reconnection in the disk. The inner disk, compressed by the black-hole magnetosphere in the MAD state, expands vertically due to the decreasing magnetic pressure. During the inversion (a timescale of $\sim 2000 r_g/c \sim 0.1$s), the MAD state is destroyed and the disk more closely resembles that of our non-MAD model, in which the accretion is driven by the magneto-rotational instability. The steady BZ jet is also quenched by this process and a new transient jet is launched by the reconnecting field. This transient jet is mildly relativistic, with velocity $\sim 0.1c$ at $200 r_g$, and is qualitatively similar to the transient, ballistic jets seen during transitions from the hard to soft state.

Here, we investigate the observational signatures of such a polarity inversion. In Figure 3.7, we show the evolution of the optical, X-rays, and γ-rays during the

global magnetic field inversion in which the MAD state is destroyed and then re-established. In the initial MAD state ($t \approx 19000\, r_g/c$), the optical band is dominated by synchrotron emission from the disk, while the X-rays and γ rays are produced by synchrotron emission and Compton scattering in the steady BZ jet. In this state, the ratio of the γ-ray to X-ray luminosities is $L_\gamma/L_X > 1$. During the transient outburst, corresponding to the destruction of the MAD state, this ratio changes to $L_\gamma/L_X < 1$. After the inversion, the disk returns to a MAD state and the BZ jet is re-launched with $L_\gamma/L_X > 1$.

Overall, the γ-ray luminosity varies by nearly two orders of magnitude while the X-rays vary by a factor of a few. There is a small increase in optical emission from the disk, peaking around the minimum of the γ-ray and X-ray emission. The re-launched BZ jet is significantly more luminous in the γ-rays and X-rays, while the disk is less luminous after the outburst. The X-ray and γ-ray lightcurves, and in particular the ratio L_γ/L_X, could be used as an observational probe of such a global magnetic field inversion, and so might be useful for directly comparing models of state transitions in XRBs with observations.

3.4.2.2 Jet-disk quasi-periodic oscillations

McKinney et al. (2012) found that the black hole magnetosphere and disk exhibit significant quasi-periodic oscillations (QPOs) in dynamical quantities including the mass density and magnetic energy density. These QPOs result from instabilities at the jet-disk interface and strongly affect the jet dynamics. The effects on the jet can clearly be seen in Figure 3.1 as density enhancements in the funnel region.

Shcherbakov & McKinney (2013) tested the observability of the QPOs in the context of Sgr A* for synchrotron emission at submillimeter wavelengths. In the present work, we investigate the detectability at higher frequencies in the case of XRBs, and extend the previous analysis to include Comptonization. In Figure 3.8, we show the power spectral density from lightcurves at 10^{15} Hz, 10^{19} Hz, and 10^{23} Hz, during a quasi-steady period of the MAD simulation (i.e., well after $t \approx 8000 r_g/c$). The lightcurves are very noisy and the power spectra show no clear

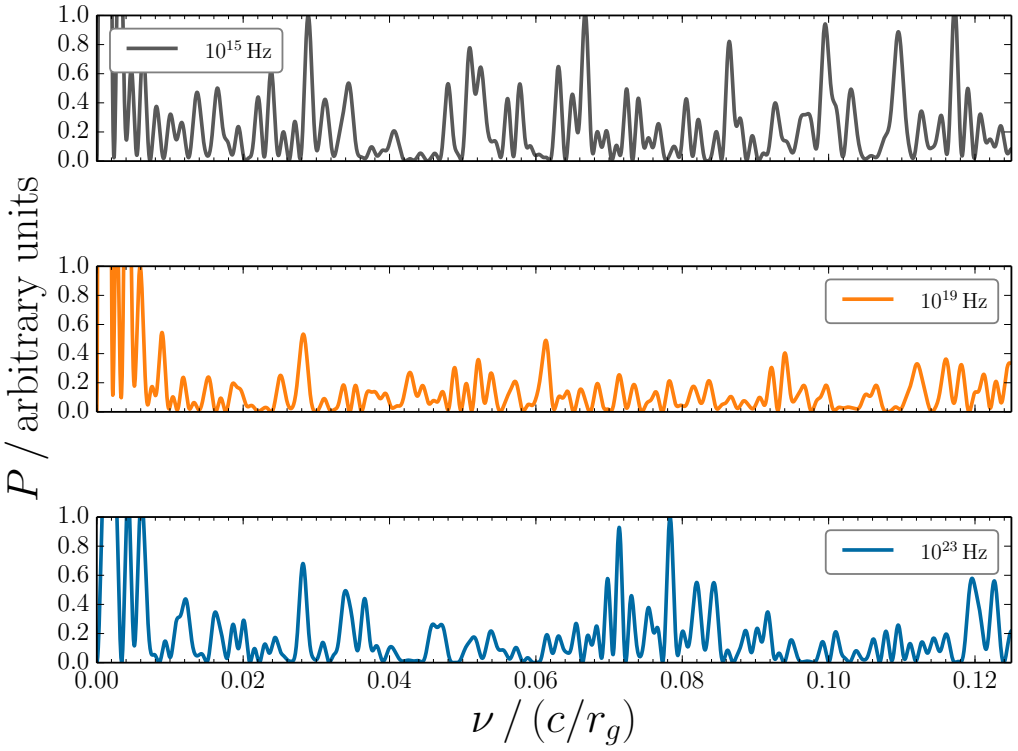

FIGURE 3.8: Power spectral densities from lightcurves at 10^{15} Hz, 10^{19} Hz, and 10^{23} Hz corresponding to synchrotron from the disk, synchrotron from the jet, and scattering from the jet, respectively. These were calculated with $\mathcal{T}_d = 10$, and $\mathcal{T}_j = 3$.

QPO signal. The lack of a clear QPO signal with Comptonization is an interesting result, and could have important implications for future efforts aimed at detecting QPOs at high frequencies. We will perform a more thorough investigation of this issue in a future work.

3.5 Summary and discussion

In this chapter, we calculated the spectrum of a RIAF in the context of the low/hard state in XRBs, with the goal of identifying high-energy signatures of jets in these systems. We investigated both MAD and non-MAD RIAFs, and find the following observational signatures of jet emission: (i) A significant peak in the γ-rays at $\sim 10^{23}$ Hz. (ii) A break in the optical/UV spectrum where it transitions from disk to jet dominated, changing from $\nu L_\nu \sim \nu^0$ at lower frequencies

to $\nu L_\nu \sim \nu$ at higher frequencies. This is followed by a second break around $\sim 10^{18}$ Hz, where the spectrum roughly returns to $\nu L_\nu \sim \nu^0$, with "wiggles" in the luminosity of a factor of a few. (iii) A pronounced peak near or below $\sim 10^{14}$ Hz indicates that jet emission contributes significantly to the X-rays. These signatures are present across a range of proton-to-electron temperature ratios.

Comparing the spectra in Figures 3.4 and 3.6, we find that spectra from our MAD model are almost completely jet dominated while those from our non-MAD model are dominated by the disk. In particular, the X-rays are produced by synchrotron self-Compton from the disk in our non-MAD model, while jet synchrotron emission dominates the X-rays in our MAD model. Our results suggest that the two competing models of X-ray production in XRBs, namely the synchrotron and synchrotron self-Compton models, are realised separately in MAD and non-MAD accretion flows, respectively. Therefore, an investigation of the observational signatures of MAD vs non-MAD systems could provide valuable insights into breaking the degeneracy between these X-ray models. We will study these observational signatures further in a future work.

In our MAD model, we investigated the evolution of the jet and disk emission during a large-scale magnetic field inversion in which the BZ jet is quenched and a new transient jet is launched. This transient jet is qualitatively similar to those observed during state transitions in XRBs (Dexter et al., 2014). During the field inversion, the X-ray and γ-ray luminosities vary dramatically on a short timescale of ~ 0.1s. The ratio of the γ-ray and X-ray luminosities changes from $L_\gamma/L_X > 1$ in the steady BZ jet to $L_\gamma/L_X < 1$ during the transient outburst, and so is potentially an important observational signature of this process. Furthermore, although outside the scope of the current work, we expect to find significant variability in the radio at later times, as the hot plasmoid propagates outward and disrupts the flow at large radii. Thus, a time lag between the fast correlated X-ray/γ-ray variability and radio variability could be a further indication of such a transient outburst.

The effects of QPOs on the jet dynamics were discussed in McKinney et al. (2012), and their effects on disk emission were discussed in Shcherbakov & McKinney (2013). Here, we extended this analysis to include the effects of Comptonization. Our results are noisy and show no clear QPO signal. This non-detection of the QPO is potentially important for future campaigns aimed at detecting QPOs at high-frequencies. The analysis here was carried out using a single electron temperature prescription, however, it is possible that different temperature prescriptions might reveal the QPO. We leave a more complete analysis of this jet-QPO variability to future work.

Our analysis was carried out for a limited range of fluid models and temperature ratios, however, it is straightforward to estimate how the spectra would change with variations in n, Θ, and B. The synchrotron and inverse Compton peak frequencies scale with fluid properties as $\nu_{\rm syn} \sim \Theta^2 B$, and $\nu_{\rm IC} \sim \Theta^2 \nu_{\rm syn}$, respectively. The heights of these peaks scale as $(\nu j_\nu)_{\rm syn} \sim n\Theta^2 B^2$, and $(\nu j_\nu)_{\rm IC} \sim y(\nu j_\nu)_{\rm syn} \sim n\Theta^2(\nu j_\nu)_{\rm syn}$. The saturation frequency is proportional to the electron temperature, $\nu_{\rm sat} \sim \Theta$. We can then scale our XRB results to AGN as follows. Assuming that the accretion rate is proportional to the black hole mass, the magnetic field, number density, and electron temperature in RIAFs vary with M as $B \sim M^{-1/2}$, $n \sim M^{-1}$, and $\Theta \sim M^0$ (see the discussion about scaling the `HARM` data to a particular system in Section 3.3.2). With these relationships, and the dependence of the spectral features on these quantities as outlined above, we can scale our results to arbitrary black hole masses.

The most significant limitation of the current work is the assumption of a thermal distribution of electrons. This may be a reasonable assumption for the disk, however it is likely that the jet will contain a significant amount of non-thermal particles due to shocks and magnetic reconnection. Also, the "fast light" approximation, which we use for computational efficiency, is an oversimplification since the dynamical time of the accretion disk and jet can be close to the light crossing time. We will extend this analysis to include the effects of non-thermal particles and time-dependence in a future work.

Chapter 4

Effects of Spin on High Energy Radiation from Accreting Black Holes

4.1 Overview

Observations of jets in X-ray binaries show a correlation between radio power and black hole spin. This correlation, if confirmed, points towards the idea that relativistic jets may be powered by the rotational energy of black holes. In order to examine this further, in this chapter, we perform general-relativistic radiative transport calculations on magnetically arrested accretion flows, which are known to produce powerful jets via the BZ mechanism. We find that the X-ray and γ-ray emission strongly depend on spin and inclination angle. Surprisingly, the high-energy power does not show the same dependence on spin as the BZ jet power, but instead can be understood as a redshift effect. In particular, photons observed perpendicular to the spin axis suffer little net redshift until originating from close to the horizon. Such observers see deeper into the hot, dense, highly-magnetized inner disk region. This effect is largest for rapidly rotating black holes due to

a combination of frame dragging and decreasing horizon radius. While the X-ray emission is dominated by the near horizon region, the near-infrared radiation originates at larger radii. Therefore, the ratio of X-ray to near-infrared power is an observational signature of black hole spin.

This chapter is based on work published in O' Riordan et al. (2016b).

4.2 Introduction

Near the black hole where the jet originates, it is not necessarily easy to distinguish what one means by a disk vs a jet due to the generically low plasma β parameter and inflow-outflow regions in both the disk and jet (McKinney & Gammie, 2004; McKinney, 2006). There is much uncertainty about the potentially complicated relationship between the high-energy emission, the inner regions of the disk/jet, and the central black hole. In particular, even if jets are powered by the rotational energy of black holes (Blandford & Znajek, 1977), due to the uncertainties in the source of the high-energy radiation discussed in chapter 1, it is not clear *a priori* how this radiation should depend on spin.

To investigate this issue, we take fully three-dimensional GRMHD simulations with different black hole spins. We perform radiative transfer calculations with Comptonization to obtain the spectrum of radiation with a focus on high-energy radiation resolved by the region near the black hole. We restrict our attention to the low/hard state in XRBs, since it is widely accepted that jets exist during this state (with transient jets launched during state transitions; Fender et al., 2004). Interestingly, although we find a strong spin dependence for the high-energy power, this does not follow the BZ scaling discussed in chapter 1. Furthermore, the effects of spin are maximum for observers located perpendicular to the spin axis of the black hole. We show that the high-energy emission originates from very close to the horizon, and the strong spin and viewing angle dependence can be understood as a redshift effect. While the X-ray power strongly depends on spin and observer inclination, the near-infrared (NIR) emission originates at larger radii and so is

less sensitive to redshift effects. Therefore, for systems whose inclination angles are known, the ratio of X-ray to NIR power in the low/hard state can potentially be used to estimate spin. Since the black hole spin does not vary between the low/hard and high/soft states, this ratio would compliment measurements of spin in the high/soft state (see e.g., McClintock et al., 2011, for a review).

In section 4.3 we briefly describe our GRMHD simulations and radiative transport post-processing method. In section 4.4 we show the dependence of radiated power on spin and calculate the effects of redshift. In section 4.5 we summarize and discuss our findings.

4.3 Model

Radiatively inefficient accretion flows (RIAFs) have been used extensively to model low luminosity systems such as the low/hard state in XRBs (see e.g., Narayan & McClintock, 2008; Yuan & Narayan, 2014). For RIAFs, by definition, the cooling time of a fluid element is much longer than the accretion time. Therefore, radiation is dynamically unimportant and the evolution of the disk/jet can be calculated using the non-radiative GRMHD equations. This allows a separation between the dynamical simulations and radiative transport post-processing of the simulation results. We use the `HARM` code (Gammie et al., 2003), which solves the GRMHD equations using a conservative, shock-capturing scheme.

For our purposes, we choose five MAD accretion flows with spins $a = \{0.1, 0.2, 0.5, 0.9, 0.99\}$ (these are A0.1N100, A0.2N100, A0.5N100, A0.9N100, A0.99N100 from McKinney et al., 2012). In these models, the black hole magnetosphere compresses the inner accretion disk such that it becomes geometrically thin and the magneto-rotational instability is suppressed. These MAD models efficiently extract rotational energy from the black hole via the BZ mechanism, launching jets along the spin axis (Tchekhovskoy et al., 2011; McKinney et al., 2012). Estimates of the jet power, based on integrating fluid energy fluxes (dominated by the Poynting flux), show that the power scales as expected for the BZ mechanism (with

corrections for high spins and disk thickness; Tchekhovskoy et al., 2012). However, such estimates are based solely on the dynamical properties of the fluid, and so the radiated power must be calculated in order to compare with observations.

Since we limit our analysis to the low/hard state in XRBs, we choose a black hole mass of $10M_\odot$, and accretion rate of $\dot{M} = 10^{-5}\dot{M}_{\rm Edd}$. Such a low accretion rate ensures that the flow is radiatively inefficient (see e.g., Narayan & McClintock, 2008). The Eddington accretion rate, $\dot{M}_{\rm Edd}$, is defined to be the mass accretion rate at which a disk with radiative efficiency 0.1 would radiate at the Eddington luminosity $L_{\rm Edd}$. That is, $\dot{M}_{\rm Edd}\, c^2 = 10\, L_{\rm Edd}$ (Narayan & McClintock, 2008). Although radio emission is expected to originate in the jet at large radii, computational limitations force us to restrict our analysis to the inner $r \approx 200\, r_g$, where $r_g = GM/c^2$ is the gravitational radius. While the setup we use can not properly capture radio emission, the NIR to high-energy emission ($\nu \gtrsim 10^{13}\,{\rm Hz}$) is dominated by regions close to the black hole, and so setting the boundary to $r = 200\, r_g$ has little effect on our results at these frequencies.

As discussed in chapter 3, the centre of the highly-magnetized, low density funnel can become artificially dense and hot due to the introduction of numerical density floors. We therefore remove this floor material by setting the density to zero in regions where $b^2/\rho > \zeta$. Here, ρ is the rest mass density, and $b^2 = b^\mu b_\mu$, where b^μ is the magnetic 4-field. The magnetic 4-field can be written in terms of the 3-field B^i as $b^\mu = h^\mu_\nu\, B^\nu/u^t$, where $h^\mu_\nu = \delta^\mu_\nu + u^\mu u_\nu$ is a projection tensor, u^μ is the fluid 4-velocity, and $B^0 = 0$. We choose $\zeta = 20$ at the horizon, and linearly interpolate to $\zeta = 10$ at $r = 10$. For $r > 10$, we simply set $\zeta = 10$. This interpolation happens to ensure that the injected floor material is accurately removed, without unnecessarily removing material very close to the black hole which can naturally become highly magnetized.

We calculate spectra using the same general relativistic radiative transport code as in chapter 3, which is based on the freely available `grmonty` (Dolence et al., 2009). This code uses the fluid data as input, and calculates the spectra assuming

synchrotron emission, self-absorption, and Compton scattering from a Maxwell-Jüttner distribution of electrons. We assume a constant proton-to-electron temperature ratio T_p/T_e. However, since differences in density and magnetization in the disk and jet can lead to different cooling rates for the electrons (Ressler et al., 2015; Foucart et al., 2016), we allow this temperature ratio to vary independently in these regions. In our models, the X-rays are dominated by the highly-magnetized inner disk (which is nearly indistinguishable from the jet base) and so varying T_p/T_e independently in the disk and jet has a negligible effect on the high-energy radiation in this case. Therefore, we simply choose a constant ratio of $T_p/T_e = 30$ everywhere (we find the same dependence of the radiated power on spin with $T_p/T_e = 3$ and $T_p/T_e = 10$).

4.4 Results

4.4.1 Radiated Power

In Figure 4.1 we show the time-averaged radiated power (frequency integrated between 10^{13} – 10^{24} Hz) for different spins and viewing angles. In what follows, any time averaging corresponds to the quasi-steady state between $t = 10000\, r_g/c$ and $t = 14000\, r_g/c$, with steps of $\Delta t = 400\, r_g/c$. We investigated the stability of this averaging in the extreme case of $a = 0.99$. Firstly, we doubled our time resolution between $t = 10000\, r_g/c$ and $t = 14000\, r_g/c$. We also increased our averaging window to $t = 18000\, r_g/c$, and found identical results in all cases.

For observers located parallel to the spin axis ($\theta = 0$), there is a difference of approximately one order of magnitude between the $a = 0.1$ and $a = 0.99$ cases. This difference increases to more than two orders of magnitude for observers perpendicular to the spin axis. Interestingly, the dependence of the radiated power on spin is significantly different from the BZ scaling. As we show below, the origin of this discrepancy is that the emission in our MAD models is dominated by the

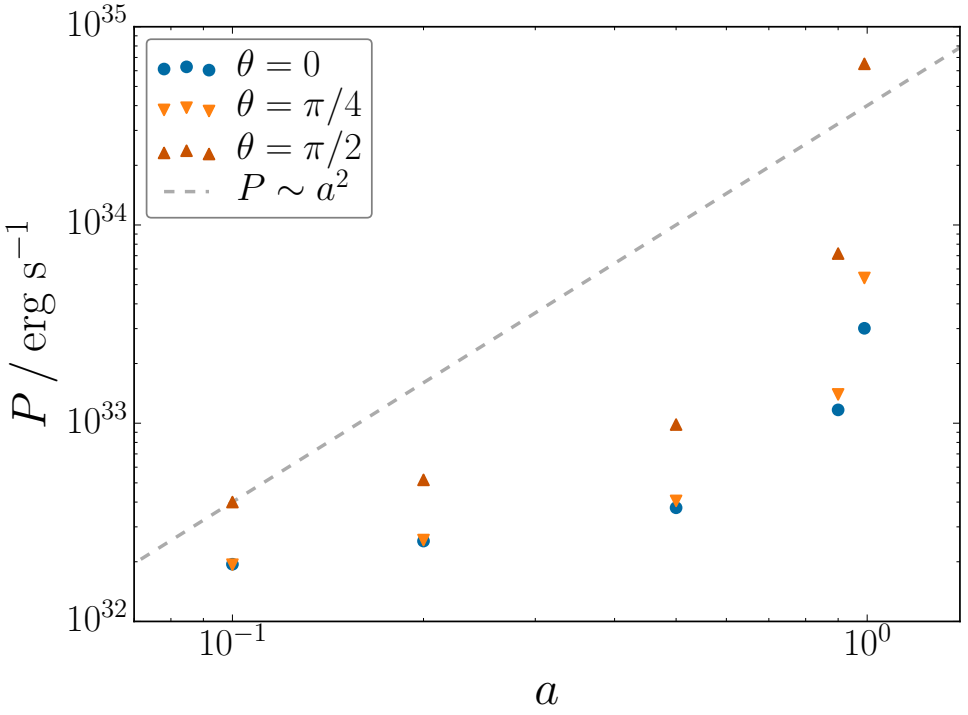

FIGURE 4.1: Integrated power vs spin for observer viewing angles of $\theta = 0$ (parallel to the spin axis), $\theta = \pi/4$, and $\theta = \pi/2$ (perpendicular to the spin axis). The dashed line corresponds to the BZ scaling $P \sim a^2$. The dependence of the radiated power on spin clearly deviates significantly from this scaling. Interestingly, the effects of spin are strongest for observers located perpendicular to the spin axis, with a difference of more than two orders of magnitude in power between the $a = 0.1$ and $a = 0.99$ cases.

inner disk, very close to the black hole horizon. The strong dependence on spin and viewing angles can be understood as a somewhat surprising redshift effect.

For any fluid quantity Q, we define the density-weighted, shell-average $\langle Q \rangle_\rho$ to be

$$\langle Q \rangle_\rho = \frac{\int \mathrm{d}A\, \rho\, Q}{\int \mathrm{d}A\, \rho} \tag{4.1}$$

where $\mathrm{d}A = \sqrt{-g}\, \mathrm{d}x^\theta \mathrm{d}x^\phi$, and $g = \det(g_{\mu\nu})$ is the metric determinant. In all our models, the Compton y parameter is $y \lesssim 1$, and so, to a good approximation, we can show the effects of spin on the power by treating synchrotron emission alone. For a thermal electron distribution, the (comoving) synchrotron power scales as $P_{\rm syn} \sim \int \mathrm{d}V n B^2 \Theta^2$, where $\mathrm{d}V = \sqrt{-g}\, \mathrm{d}x^r \mathrm{d}x^\theta \mathrm{d}x^\phi$, n is the electron number density, B is the magnetic field strength, and $\Theta = kT_e/mc^2$ is the dimensionless electron temperature. In Figure 4.2 we show the time-averaged $\langle nB^2\Theta^2 \rangle_\rho$, which

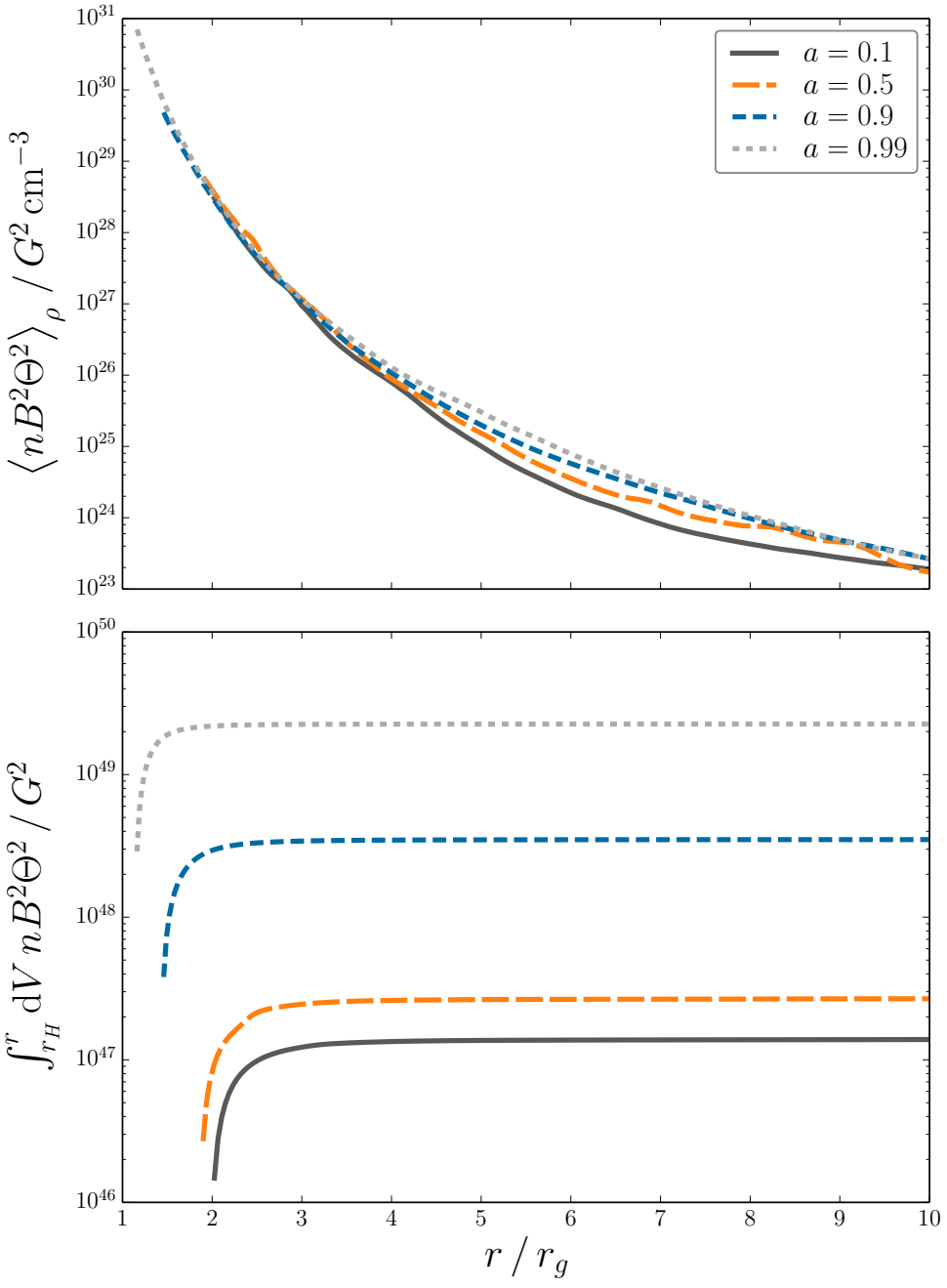

FIGURE 4.2: Time- and shell-averaged $nB^2\Theta^2$, weighted by the density. This quantity is proportional to the total synchrotron emissivity. The bottom panel shows $nB^2\Theta^2$ integrated over volume with the integral taken between the horizon and r. This quantity is proportional to the total synchrotron power. It is clear that the (comoving) radiated power is dominated by the near horizon region.

is proportional to the synchrotron emissivity νj_ν (where j_ν has units of erg cm^{-3} s^{-1} ster^{-1} Hz^{-1}; Rybicki & Lightman, 1979).

Clearly, the emissivity is a strong function of r, and increases towards the black hole due to the increase in magnetic energy density and compression by the magnetosphere. Furthermore, the emissivity profiles are roughly independent of spin. This is likely a consequence of the MAD state. McKinney et al. (2012); Tchekhovskoy et al. (2012) showed that in MAD accretion flows the magnetic flux saturates near the horizon, depending only weakly on spin ($\sim 20\%$ difference between the $a = 0$ and $a = 1$ simulations). Therefore, for a fixed disk angular thickness, black hole mass and accretion rate, we expect the profile of B^2 to be the same for different spins. Close to the black hole, the fluid properties are determined by an approximate force balance between the inner magnetosphere and the thermal and ram pressures (McKinney et al., 2012), and so this explains why the fluid properties are also roughly independent of spin.

The bottom panel shows the (comoving) synchrotron power $P_{\rm syn}(r) \sim \int_{r_H}^{r} \mathrm{d}V n B^2 \Theta^2$. It is clear from this plot that the radiated power is dominated by the near horizon region. The synchrotron emissivity profiles are independent of spin, and so the increase in power is simply a consequence of the decreasing horizon radius (from $r = 2\,r_g$ to $r = 1\,r_g$ as the spin increases from $a = 0$ to $a = 1$). However, since the difference in power is due to radiation from $r \lesssim 2\,r_g$, it will be strongly gravitationally redshifted and so it is not immediately obvious that this effect is observable. In order to check that this is in fact the reason for the spin dependence in Figure 4.1, we must estimate the observed power. That is, we must account for the effects of redshift (both gravitational and Doppler).

Interestingly, as we explain in section 4.4.2, redshift effects naturally explain the dependence on spin and viewing angle. In particular, for rapidly rotating black holes, frame dragging ensures that photons received by observers located at $\theta = \pi/2$ suffer little net redshift until very close to the horizon. In this case, there is little difference between the comoving and observed power, and so these observers see a very large increase in radiated power with spin. Although this effect is largest

for observers perpendicular to the spin axis, observers located parallel to the spin axis should also see an increase in power due to the fact that the radius of the event horizon (i.e., the infinite redshift surface) decreases with spin.

4.4.2 Redshift

We consider the Kerr spacetime with metric $g_{\mu\nu}$ in Boyer-Lindquist coordinates. We define the redshift factor to be the ratio of the energy at infinity to the energy in the rest frame of the fluid

$$\mathcal{R} = \frac{E_\infty}{E} = \frac{\xi^\mu p_\mu}{u^\mu p_\mu} = \frac{p_t}{u^\mu p_\mu} \tag{4.2}$$

Here, u^μ is the fluid 4-velocity, p^μ is the photon 4-momentum, and $\xi^\mu = \delta^\mu_t$ is the Killing vector associated with stationarity. Since p_t is conserved along geodesics, all the above quantities can be measured at the location of the emitting fluid element.

In Figure 4.3, we show the numerically calculated redshift profiles for different spins and viewing angles. For a given spin and viewing angle, this calculation shows the average redshift experienced by a photon as a function of r. The top panel shows the redshift factor for an observer with $\theta = 0$. Close to the black hole, the θ velocity is negligible and so Doppler boosting is unimportant for these observers. Therefore, for $a = 0.1$, the redshift factor is almost identical to the Schwarzschild case. More accurately, for observers located at $\theta = 0$, the redshift is given by the lapse function $\alpha = \sqrt{-g_{tt} + \Omega^2 g_{\phi\phi}}$, where $\Omega = -g_{t\phi}/g_{\phi\phi}$ is the angular velocity of a "zero angular momentum observer" (ZAMO; Bardeen et al., 1972; MacDonald & Thorne, 1982). Note, however, that $\mathcal{R} = \alpha$ only if $\chi^\mu p_\mu = p_\phi = 0$, where $\chi^\mu = \delta^\mu_\phi$ is the Killing vector associated with axisymmetry (see appendix B for details). Importantly, although these profiles are identical at large radii, they deviate from each other close to the black hole since the horizon radius decreases with spin.

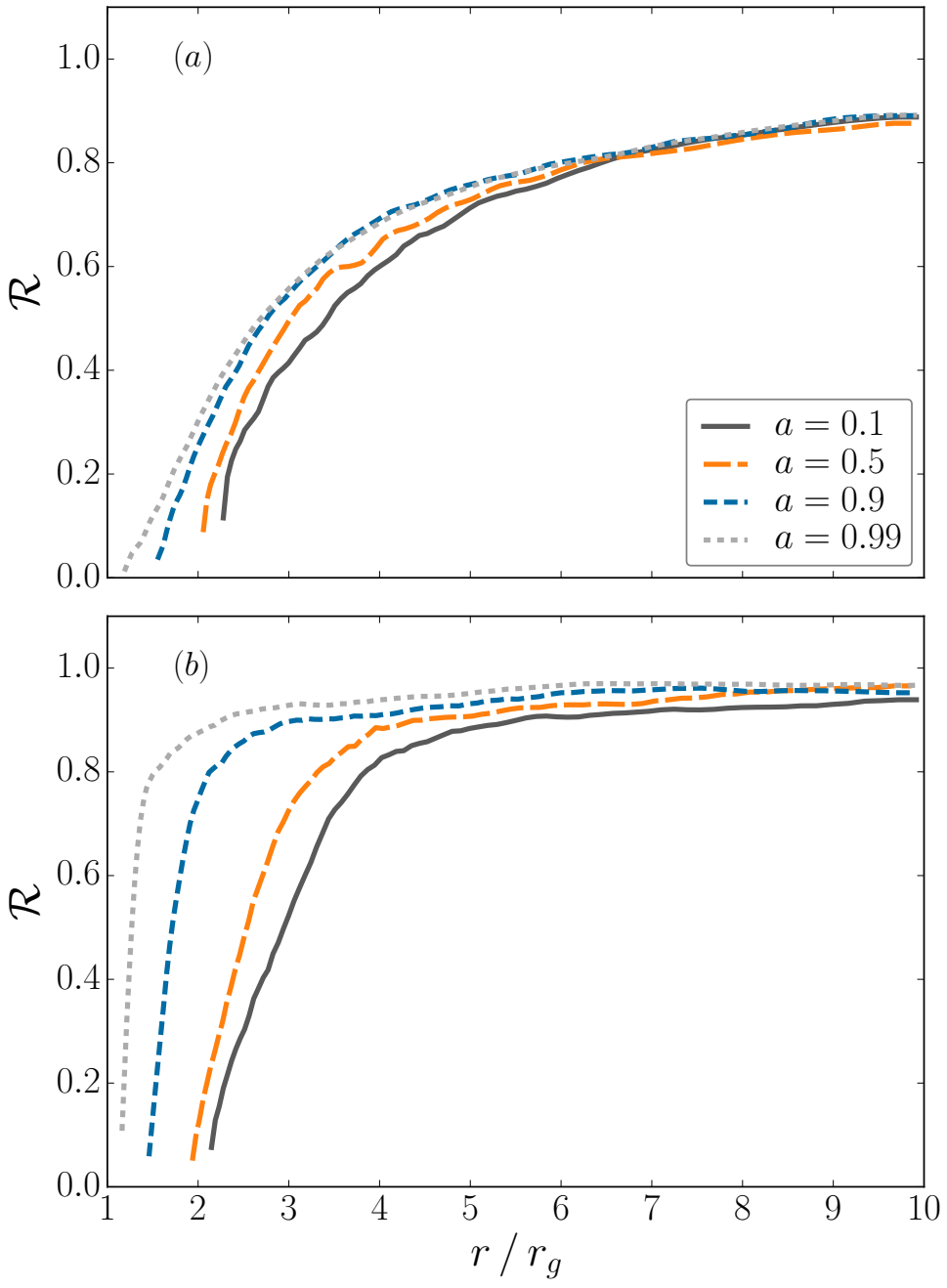

FIGURE 4.3: Redshifts for different spins and viewing angles (a) : $\theta = 0$, (b) : $\theta = \pi/2$. These were calculated numerically from snapshots of the GRMHD data. The redshift profiles are much flatter for observers with $\theta = \pi/2$. That is, photons received by these observers suffer little net redshift until very close to the horizon. Observers with $\theta = \pi/2$ see much deeper into the inner disk than observers with $\theta = 0$.

The bottom panel shows the redshift factor for observers with $\theta = \pi/2$. These profiles are strikingly different from the $\theta = 0$ case. In particular, due to a combination of frame dragging and Doppler boosting, photons suffer little net redshift until very close to the horizon. Observers located at $\theta = \pi/2$ see deeper into regions of higher emissivity. This naturally explains the large difference in observed power between the $\theta = 0$ and $\theta = \pi/2$ inclinations.

While these calculations use model-dependent fluid data as input, we show in appendix B that the flattening of the redshift profile with spin is in fact a very general feature of rotating black holes. That is, the redshift profiles depend only weakly on the details of the accretion model, with the main contributions being black hole spin and observer viewing angle. Therefore, for systems in which the comoving power is dominated by fluid close to the horizon, we expect the high-energy emission to be a robust signature of spin and viewing angle.

4.4.3 Spectra and Observational Signatures of Black Hole Spin

In Figure 4.4 we show spectra for different spins and viewing angles, calculated from snapshots of the fluid data. In the top panel, we show spectra for observers with $\theta = \pi/2$, which maximizes the effects of spin. For the $a = 0.1$ case, the synchrotron emission peaks in the optical, while for the $a = 0.99$ case this peak increases to the X-rays. There is also clear γ-ray emission due to inverse Compton scattering, which becomes more pronounced with increasing spin. Interestingly, the NIR emission is roughly constant with spin while the high-energy radiation, namely the X-rays and γ-rays, vary significantly with spin. The bottom panel shows the effects of varying observer inclination in the $a = 0.9$ case. Both the total luminosity and frequency of the peak emission increase with viewing angle. Interestingly, there is little difference between the $\theta = 0$ and $\theta = \pi/4$ inclinations (see also Figure 4.1), however the luminosity increases by roughly an order of magnitude between the $\theta = \pi/4$ and $\theta = \pi/2$ cases.

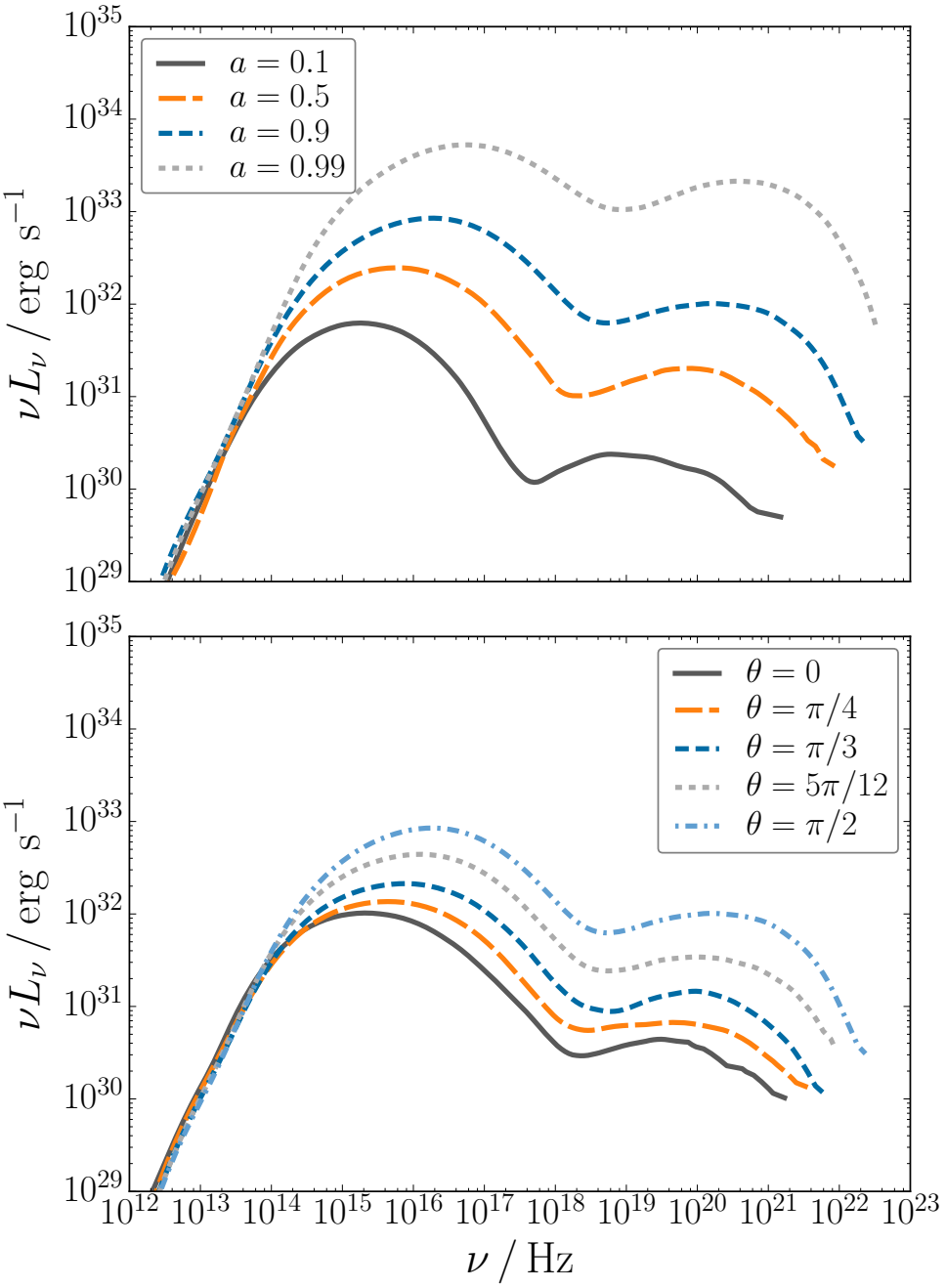

FIGURE 4.4: The top panel shows spectra for observers with $\theta = \pi/2$, calculated from snapshots of the fluid data. The NIR emission is roughly constant with spin while the X-rays and γ-rays vary significantly. The bottom panel shows the dependence on viewing angle for the $a = 0.9$ case. Both the luminosity and frequency of emission increase with viewing angle.

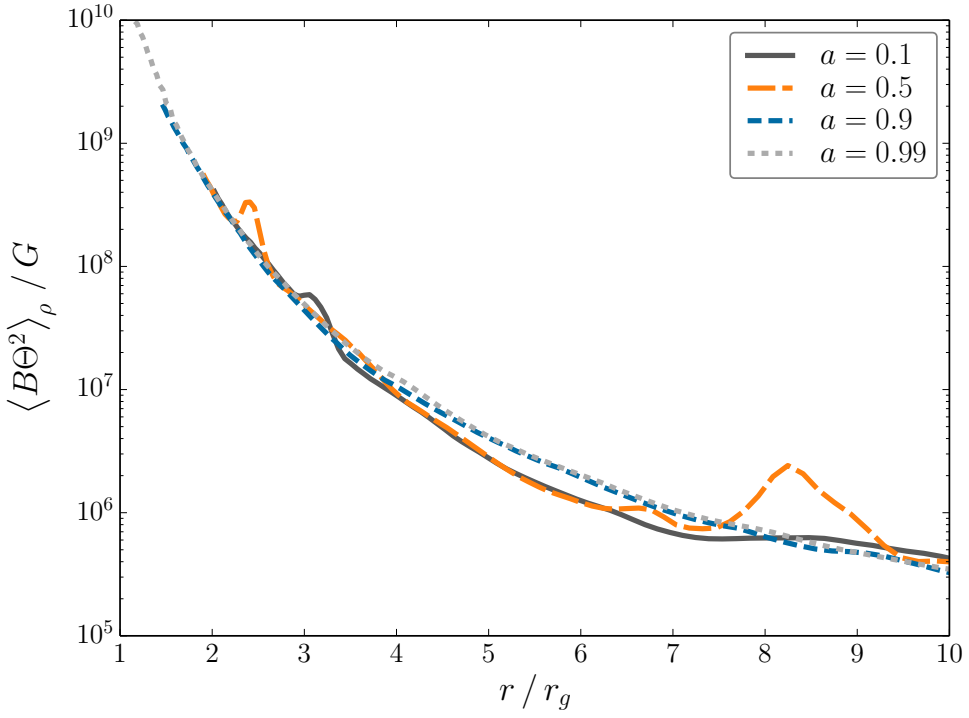

FIGURE 4.5: Time- and shell-averaged $B\Theta^2$, weighted by the density. This quantity is proportional to the characteristic synchrotron frequency. The high-energy emission is dominated by the near horizon region.

As with the total radiated power, the dependence of the spectra on spin and viewing angle can be understood as a simple consequence of the emission radius. In Figure 4.5 we show $\langle B\Theta^2 \rangle_\rho$ as a function of radius and spin. This quantity is proportional to the characteristic synchrotron frequency and so, as with the total radiated power, we expect the frequency of emission to increase towards the horizon. For higher spins and inclinations, observers receive radiation from smaller radii and therefore higher frequencies. Lower frequency photons come from larger radii and so are less sensitive to redshift effects, therefore the low-frequency power should vary less with spin and viewing angle. Furthermore, since the emission is dominated by the near horizon region, we expect the lightcurves to show significant variability over short timescales ($\sim$ few r_g/c). We also expect the high-frequency emission to vary over shorter timescales than the low-frequency emission, with a factor of $\sim$ few difference between the NIR and X-ray variability timescales.

In Figure 4.6 we show the (time averaged) ratio of the X-ray (integrated between 10^{16} – 10^{19} Hz) to NIR (integrated between 10^{13} – 10^{14} Hz) power. As expected,

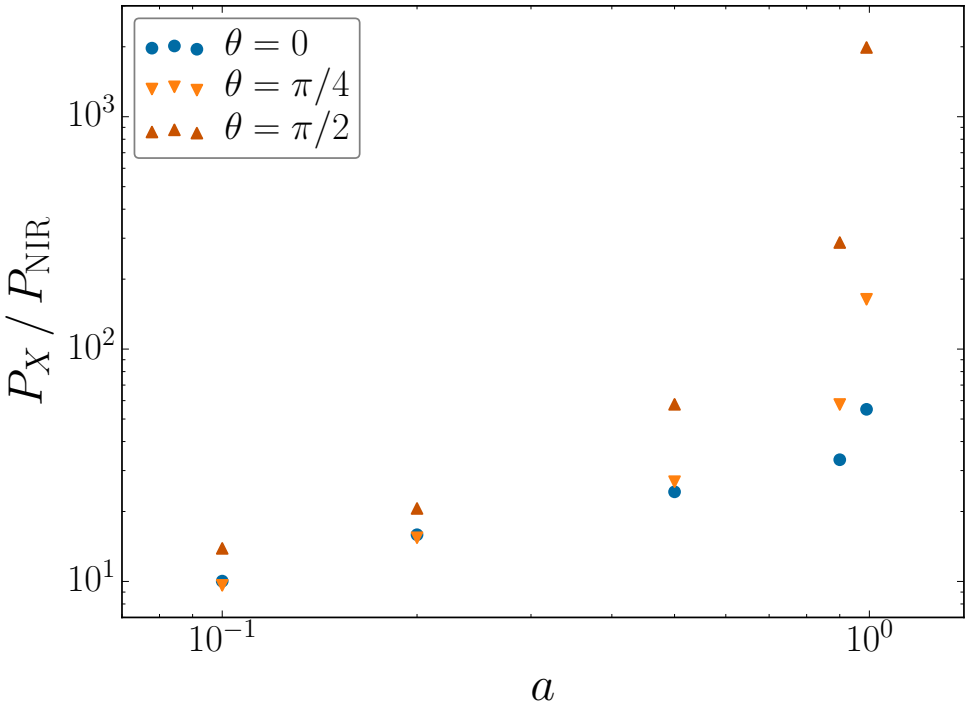

FIGURE 4.6: Ratio of the X-ray power to the NIR power for different spins and viewing angles. For large inclinations, this ratio depends very strongly on spin.

this ratio depends very strongly on viewing angle and spin. Therefore, for systems whose inclination angle is known, especially those with large inclinations, the ratio $P_X/P_{\rm NIR}$ is a strong signature of spin. The black hole spin likely does not vary significantly between the low/hard and high/soft states, and so this ratio potentially compliments measurements of spin in the high/soft state. Since the synchrotron frequency depends reasonably weakly on our choice of mass accretion rate ($\nu_{\rm syn} \sim \dot{M}^{1/2}$; see appendix C), we expect this ratio to be a robust signature over a range of accretion rates.

4.4.4 Retrograde Spin

For comparison with Figure 4.1, in Figure 4.7 we show the integrated power vs spin for retrograde spins $a = \{-0.2, -0.5, -0.9\}$. As in the prograde case, the radiated power increases with spin and this effect is largest for observers perpendicular to the spin axis. Interestingly, the total radiated power is lower in the retrograde case than in the prograde case. This is likely due to the fact that prograde black

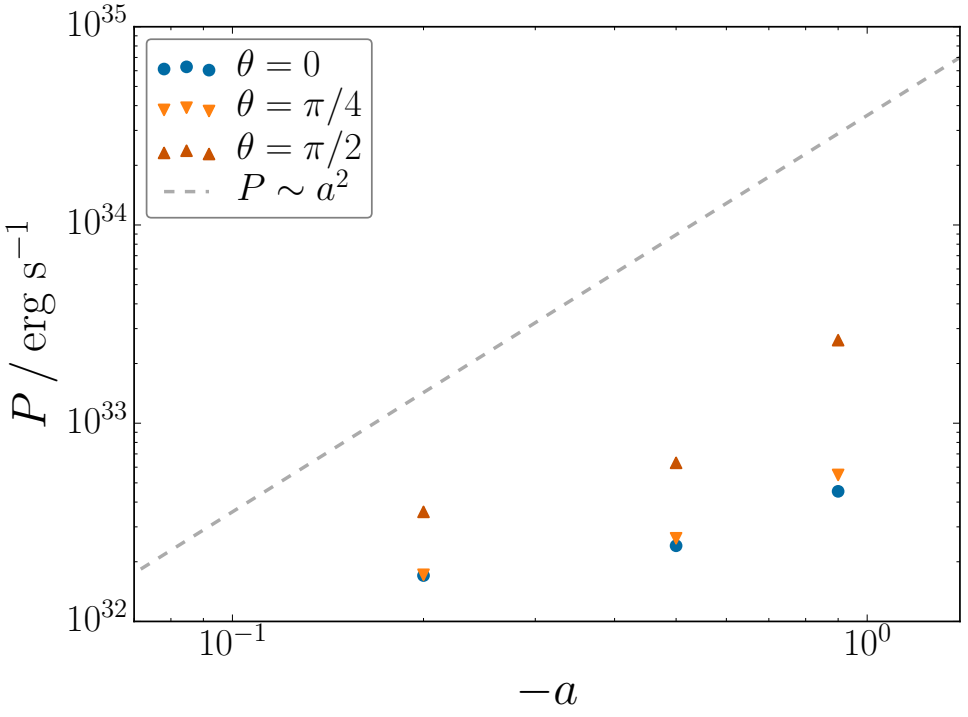

FIGURE 4.7: Integrated power vs spin for retrograde spins. The total radiated power is lower in the retrograde case than the prograde case due to a combination of redshift and the fact that less magnetic flux is trapped in the retrograde case.

holes trap more magnetic flux close to the horizon than retrograde black holes (Tchekhovskoy & McKinney, 2012). Our results show a difference of a factor of ~ 3 between the $a = -0.9$ and $a = 0.9$ cases, which is consistent with the findings of Tchekhovskoy & McKinney (2012). Importantly, although the radiated power is not completely symmetric with spin, there is clearly a degeneracy between the prograde and retrograde cases. Therefore, while the ratio of the X-ray to NIR power discussed in section 4.4.3 is an observational probe of spin, more information would be required to distinguish between prograde and retrograde spins.

4.4.5 Misalignment Between Jet/Disk and Spin Axis

In the models considered so far, the disk angular momentum axis is aligned parallel to the black hole spin axis. In principle, however, the accreting plasma can have an arbitrary angular momentum axis. McKinney et al. (2013) studied systems in

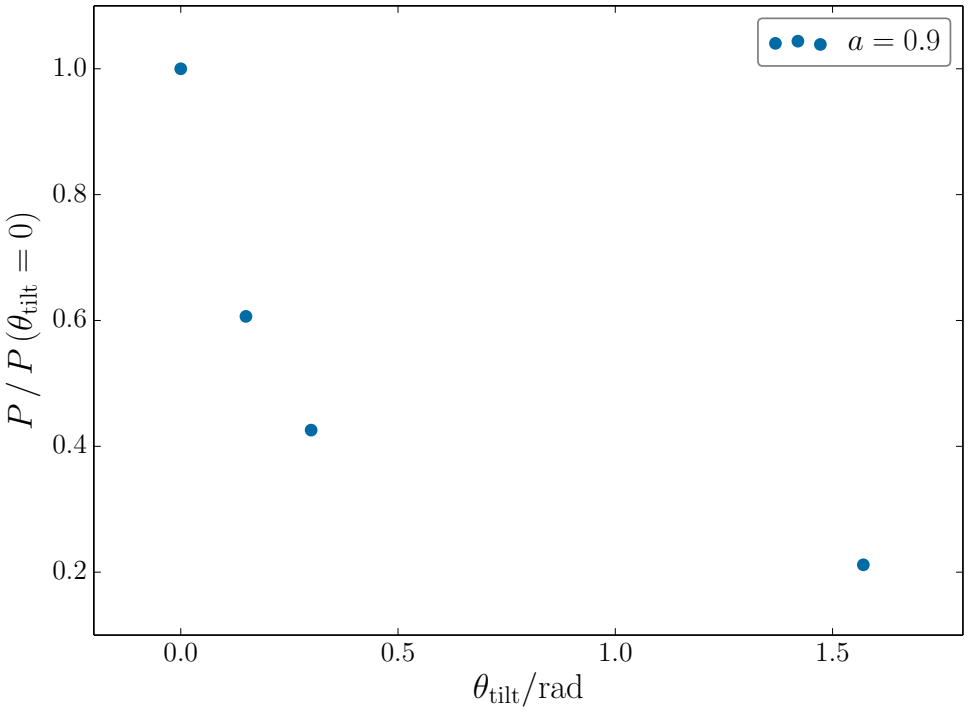

FIGURE 4.8: Observed integrated power (as a fraction of untilted power) vs relative tilt angle. Since the emission is dominated by the near horizon region, for small misalignments there is little deviation from the untilted case.

which there is a misalignment between the disk/jet and the black hole spin axis. They reported a "magneto-spin alignment" mechanism which tends to align disks and jets with the rotation axis at small radii. Therefore, since the emission in our models is dominated by the near horizon region, we expect our results to be robust to minor misalignments.

In Figure 4.8 we show the integrated power vs relative tilt angle for the $a = 0.9$ case, with the observer located perpendicular to the spin axis. The relative tilt angle, $\theta_{\rm tilt}$, is defined to be the angle between the spin axis and the disk's angular momentum axis at large distances. The tilt angles (in radians) are $\theta_{\rm tilt} = \{0.0, 0.15, 0.3, \pi/2\}$. There is a factor ~ 2.5 difference in the observed power between the untilted and $\theta_{\rm tilt} = 0.3\,{\rm rad}$ cases, and a difference of ~ 5 between the untilted and fully tilted ($\theta_{\rm tilt} = \pi/2\,{\rm rad}$) cases. We also considered a small tilt of $\theta_{\rm tilt} = 0.15\,{\rm rad}$ for the extreme case of $a = 0.99$, and found a difference of < 2 between the untilted and tilted models. Therefore, we expect our results to be

valid for systems with minor misalignments between the disk/jet and the black hole spin axis.

4.5 Summary and Discussion

In this chapter, we calculated the effects of spin on high-energy emission from the low/hard state in XRBs. We modelled the low/hard state as a MAD accretion flow, and investigated both prograde retrograde spins. We found that the X-ray power strongly depends on spin and observer inclination. In particular, the spin dependence is strikingly different from the BZ dependence expected for jet emission. In our models, the X-rays are dominated by the inner disk, and the strong dependence on spin and viewing angle can be understood as a redshift effect. For high spins and inclination angles, observers receive photons from smaller radii and therefore regions of larger synchrotron emissivity. Since the high-energy emission originates close to the horizon, it is more sensitive to spin than the low-energy emission that originates from larger radii. We identified the ratio of the X-ray power to NIR power as an observational signature of spin. This quantity could potentially be used to estimate spin, and would compliment measurements of spin based on observations in the high/soft state.

While we expect this ratio to be particularly useful in systems with large inclinations, in general, its dependence on quantities such as the viewing angle introduces significant degeneracy. Therefore, by itself, this ratio can not uniquely determine the black hole spin. However, since the high-energy spectrum in the low/hard state is clearly sensitive to both spin and viewing angle, it may be possible to use more features of the spectrum to constrain these quantities. In particular, following the approach of the continuum-fitting (CF) and Fe line methods (e.g., McClintock et al., 2011), one could build up models of high-energy spectra for different spins and inclinations and, for a given observational spectrum, find the best χ^2 fit. This new approach could potentially cross-validate existing methods based on fitting observations in the high/soft state. A disadvantage of this method

is that it can not easily distinguish between prograde and retrograde spins. Both the CF and Fe line methods use the ISCO, which is monotonic with spin. The method described here relies on the horizon radius and the effects of redshift and so is more symmetric with spin. Therefore, more information would be needed to break the degeneracy between retrograde and prograde spins.

The dependence of the high-energy power on spin is due to the combination of two main components, the redshift and synchrotron emissivity profiles. Interestingly, the behaviour of the redshift is in fact a very general feature of rotating black holes, and is largely independent of the details of accretion. On the other hand, the emissivity itself is a model-dependent quantity. Our results rely on the fact that the comoving synchrotron power in our MAD models is strongly dominated by the near horizon region. The observed high-energy radiation should therefore be highly variable on timescales of the order of a few light crossing times. Furthermore, we expect the variability timescale for the lower frequency emission to be longer since this originates at larger radii.

The spectra shown in Figure 4.4 are consistent with the basic observed X-ray hardness/flux relations for XRBs in the low/hard state (Fender et al., 2004). The time-averaged X-ray hardness ratio (defined to be the ratio of the flux at 6.3–10.5 keV to the flux at 3.8–7.3 keV; Fender et al., 2004; Belloni et al., 2005) varies between 0.7 and 0.9, with higher spins slightly softer than lower spins. The luminosities in the low spin cases are likely somewhat lower than expected for the low/hard state, and are probably more consistent with the so-called quiescent state (e.g., Remillard & McClintock, 2006). However, this is not a serious issue. As we show in appendix C, small changes in the accretion rate can significantly increase the total luminosity without greatly affecting the frequency of emission. Therefore, increasing the luminosity would not change our conclusions regarding the scaling in Figure 4.1 or the ratio $P_X/P_{\rm NIR}$ in Figure 4.6.

Mościbrodzka et al. (2009) considered the effects of spin and viewing angle on radiation from non-MAD (called SANE in Narayan et al., 2012) accretion flows in the context of Sgr A*. Interestingly, while they found that the X-ray flux

increases dramatically with both spin and observer inclination, they attribute this dependence to a different effect than the one described here. In their models, the X-ray emission is produced by scattering from hot electrons at $r = r_{\rm ISCO}$, and so the dependence on spin manifests itself in a very similar manner to thin disks (see e.g., McClintock et al., 2011). In our models, by contrast, most of the observed high-energy radiation originates from right outside the horizon, with the ISCO playing no special role. This can likely be attributed to the fact that the disks considered here are geometrically thicker, and so the density does not drop off significantly inside the ISCO. Therefore, our results are probably more relevant for low luminosity, radiatively inefficient systems, in which the disk is expected to be geometrically thick.

Furthermore, our work improves upon this study in two major areas. Firstly, our simulations are fully 3D, which is required to avoid decaying turbulence and reach a well defined steady state (Cowling, 1933; Sądowski et al., 2015). Axisymmetric simulations can not reliably capture the effects of spin, since the resulting radiation will be influenced by the extent to which the spin has affected the flow by the time the turbulence decays. Secondly, in MAD models, the final amount of magnetic flux at the horizon is independent of the initial flux content of the torus, which in SANE models can artificially introduce a spin dependence (Tchekhovskoy & McKinney, 2012; Tchekhovskoy et al., 2012). Therefore, MAD models are more reliable for studying the effects of spin on the high-energy radiation.

While our calculations apply to MAD accretion flows in the low/hard state, the redshift effects described here might also be important when considering thin MADs in the high/soft state. Avara et al. (2016) demonstrated an 80% deviation from the standard Novikov-Thorne radiative efficiency, with most of the radiation coming from at or below the ISCO. As shown here, for rapidly spinning black holes, radiation from small radii is very strongly affected by variations in spin and viewing angle. Therefore, if the radiation from thin MADs originates at smaller radii than expected for standard thin disks, this could have important implications for measurements of spin in the high/soft state.

Our analysis was carried out for a black hole mass of $M = 10M_\odot$. However, since the relevant length and time scales are set by M, we can scale our results to arbitrary masses as follows. Assuming that the accretion rate is a fixed fraction of the Eddington rate $\dot{M} \sim \dot{M}_{\rm Edd} \sim M$, from appendix C we find that $n \sim M^{-1}$, $B \sim M^{-1/2}$, and $\Theta \sim M^0$. These relationships can be used to scale the spectral features in Figure 4.4 to supermassive black holes. Importantly, however, this scaling is only appropriate for systems which are well described by RIAFs. Therefore, our results are potentially relevant for accreting supermassive black hole systems such as Sgr A* and low luminosity subclasses of AGN such as LINERS and BL Lac objects (see e.g., Yuan & Narayan, 2014). Although BL Lacs (and blazars in general) have jets roughly aligned with the observer, at small radii there could be a misalignment between the jet and spin axes (see section 4.4.5). Such a misalignment could significantly enhance the high-energy emission from close to the black hole, leading to the intriguing possibility that near-horizon emission is responsible for the short-timescale variability observed in these systems (e.g., Aharonian et al., 2007; Albert et al., 2007; Aleksić et al., 2011; Ackermann et al., 2016).

The current work is somewhat limited by the assumption of a thermal distribution of electrons. The highly-magnetized inner disk region could contain a significant number of non-thermal particles due to acceleration by magnetic reconnection (e.g., Sironi & Spitkovsky, 2014). However, thermal electrons might dominate emission from near the horizon, as has been sufficient to explain the low-hard like state in Sgr A* and M87 (Dexter et al., 2012; Broderick et al., 2014; Broderick & Tchekhovskoy, 2015). Furthermore, different prescriptions for treating the electron temperature might reduce the dominance of emission from the inner disk and instead "light up" the funnel wall region (e.g., Mościbrodzka & Falcke, 2013; Mościbrodzka et al., 2014). As discussed in chapter 3, these prescriptions usually separate the jet and disk based on b^2/ρ or the plasma β. In our models, the inner disk is highly magnetized and so differentiating between the jet and disk based on the magnetization alone would in fact treat the inner disk region in a similar manner to the jet. The treatment of the electron physics in accretion disks and

jets remains an active area of research, and we will apply our results with new models of electron physics as they become available.

Chapter 5

Blazar Variability from Turbulence in Jets Launched by Magnetically Arrested Accretion Flows

5.1 Overview

Blazars show variability on timescales ranging from minutes to years, the former being comparable to and in some cases even shorter than the light-crossing time of the central black hole. The observed γ-ray lightcurves can be described by a power-law power density spectrum (PDS), with a similar index for both BL Lacs and flat-spectrum radio quasars. In this chapter, we show that this variability can be produced by turbulence in relativistic jets launched by magnetically arrested accretion flows (MADs). We perform radiative transport calculations on the turbulent, highly-magnetized jet launching region of a MAD with a rapidly rotating supermassive black hole. The resulting synchrotron and synchrotron self-Compton emission, originating from close to the black hole horizon, is highly variable. This variability is characterized by PDS which is remarkably similar to the observed

power-law spectrum at frequencies less than a few per day. Furthermore, turbulence in the jet launching region naturally produces fluctuations in the plasma on scales much smaller than the horizon radius. We speculate that similar turbulent processes, operating in the jet at large radii (and therefore high bulk Lorentz factor), are responsible for blazar variability over many decades in frequency, including on minute timescales.

This chapter is based on work published in O' Riordan et al. (2017).

5.2 Introduction

As discussed in chapter 1, the origin of the significant variability observed in blazars remains uncertain. In this chapter, we argue in favour of the proposal by Narayan & Piran (2012), namely that turbulence in the relativistic jet can produce the observed variability properties. To support this claim, we investigate the variability of high-energy radiation from a magnetically arrested accretion flow (MAD; Narayan et al., 2003), which efficiently launches jets via the BZ mechanism (Blandford & Znajek, 1977; Tchekhovskoy et al., 2011; McKinney et al., 2012). Importantly, computational limitations force us to restrict our analysis to the inner $r \lesssim 200 r_g$ of the MAD, where $r_g = GM/c^2$ is the gravitational radius. O' Riordan et al. (2016b) showed that, for rapidly rotating black holes, observers see deep into the hot dense, highly-magnetized plasma in the inner parts of MADs. In what follows, we will refer to this region as the "jet launching region". Since the radiated power in our model is dominated by the turbulent plasma of the jet launching region close to the horizon, we expect the resulting radiation to be variable on timescales comparable to the light-crossing time $t_g = r_g/c$.

We find that γ-ray lightcurves from the jet launching region can be described by a PDS which is remarkably similar to that observed in both BL Lacs and FSRQs. Furthermore, the optical synchrotron emission can also be described by the same PDS, despite having a different origin. The large inferred pair opacity in high-luminosity FSRQs prevents radiation originating in the jet launching zone from

directly contributing to the observed variability. However, assuming that the turbulent properties of the launching region persist at large radii (and therefore large bulk Lorentz factor Γ), we argue that it is plausible that the observed variability properties result from turbulence in the jet.

In section 5.3 we briefly describe our model and assumptions. In section 5.4 we show the resulting PDS and compare with observations. In section 5.5 we discuss our findings, with emphasis on the limitations of our model and suggestions for future work in this area. We use units where $G = c = 1$ and therefore $r_g = t_g = M$, however we occasionally reintroduce factors of c for clarity.

5.3 Model

We simulate a MAD accretion flow using the fully 3D GRMHD code `HARM` (Gammie et al., 2003). Our model is based on run A0.99N100 from McKinney et al. (2012), restarted at $t = 15000\,M$ with a very high temporal resolution of $\Delta t = 0.1M$, and a spatial resolution of $N_r \times N_\theta \times N_\phi = 288 \times 128 \times 128$. This is the highest spatial resolution available for a 3D GRMHD simulation of a MAD accretion flow. As described in Tchekhovskoy et al. (2011); McKinney et al. (2012), the grid concentrates resolution in the equatorial disk at small radii and in the jet at large radii. Close to the black hole, the radial grid is logarithmically spaced with $\Delta r \approx 0.03\,M$ at the horizon, increasing to $\Delta r \approx M$ at $r = 30\,M$. For our purposes, we consider a black hole spin of $a = 0.99$ and limit our analysis to times $t \geq 15000\,M$, well after the simulation settled into a quasi-steady MAD state. As is discussed in chapters 3 and 4, we remove the numerical density floor material from the centre of the funnel region before performing our radiative transport post-processing calculation. Although this material is required to maintain numerical stability during the GRMHD simulation, it can become artificially dense and hot and so might distort the resulting spectra. Therefore, when calculating the spectra, we simply remove the floor material, focussing our attention on the self-consistent disk and funnel wall regions. We do this by setting the density to zero in regions

where the ratio of magnetic and rest mass energy densities becomes too large; $b^2/\rho > \zeta$. Here, $b^2 = b^\mu b_\mu$, b^μ is the magnetic 4-field, ρ is the rest mass density of the fluid. At the horizon, we choose $\zeta = 20$, and linearly interpolate to $\zeta = 10$ at $r = 10\,M$. Beyond this, we choose a constant value of $\zeta = 10$. This ensures that we don't remove any of the self-consistent, highly-magnetized fluid close to the horizon when discarding the floor material.

We calculate the properties of the resulting radiation field using a code based on `grmonty` (Dolence et al., 2009). We include synchrotron emission, self-absorption, and Compton scattering from relativistic, thermal electrons. We choose a constant proton-to-electron temperature ratio of $T_p/T_e = 30$, which is consistent with recent radiative GRMHD simulations of active galactic nuclei (Sądowski & Gaspari, 2017). As discussed in Ressler et al. (2015); Foucart et al. (2016); Sądowski et al. (2017), electrons in the jet and disk are probably subject to different heating and cooling mechanisms due to differences in density and magnetization. This would likely cause T_p/T_e to vary across these regions. In our case, the emission is strongly dominated by a highly-magnetized, compact region close to the black hole and we find that varying T_p/T_e independently in the jet and disk has little effect on our main results. Furthermore, choosing a different ratio of $T_p/T_e = 3$ everywhere doesn't affect the resulting temporal behaviour. The absence of non-thermal electrons, which could be important in a more realistic description of the high-energy γ-ray lightcurves, is a limitation of the current model; we will address this in a future work.

For analysing the variability, we choose snapshots of the GRMHD data corresponding to time steps Δt ranging from $0.1M$ to $10M$. This allows us study variability on a wide range of timescales, while still producing lightcurves which are evenly sampled in time. We also vary the total number of photons tracked during our radiative transport calculation. The number of photons tracked per time step ranges from 10^5, for calculations over long timescales, to 10^7 per time step for the shortest timescales. Importantly, we use a "fast-light" approximation in which each snapshot is treated independently. This allows us to parallelize our

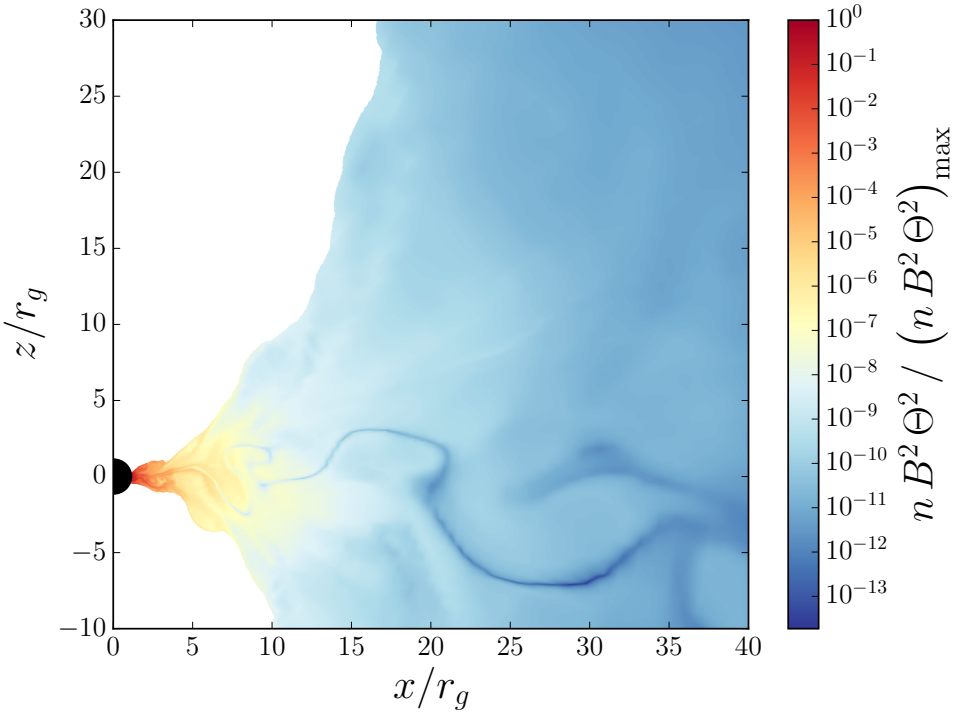

FIGURE 5.1: Snapshot of the GRMHD model showing the quantity $nB^2\Theta^2$, which is proportional to the comoving synchrotron power per unit volume. The floor material has been excised from the funnel region. Both the synchrotron power and the synchrotron self-Compton component are strongly dominated by the inner $\sim 5\,M$.

radiative transport calculation over both photons and time steps, significantly improving both performance and computational simplicity. Since the emission from our model originates in the compact jet launching region, this approximation is valid over a wide range of timescales. The disadvantage of this approach, however, is that it sets practical limitations on the shortest timescales that we can reliably probe. The "fast-light" assumption effectively sets the speed of light to infinity, which fails to be valid for timescales shorter than the light-crossing time of the emission region. Therefore, our current code is not sensitive to very fast variability on timescales shorter than $\sim M$. Furthermore, the smallest structures in the GRMHD data are smoothed out over ~ 10 cells and so, on the shortest timescales, our analysis is also limited by the grid resolution.

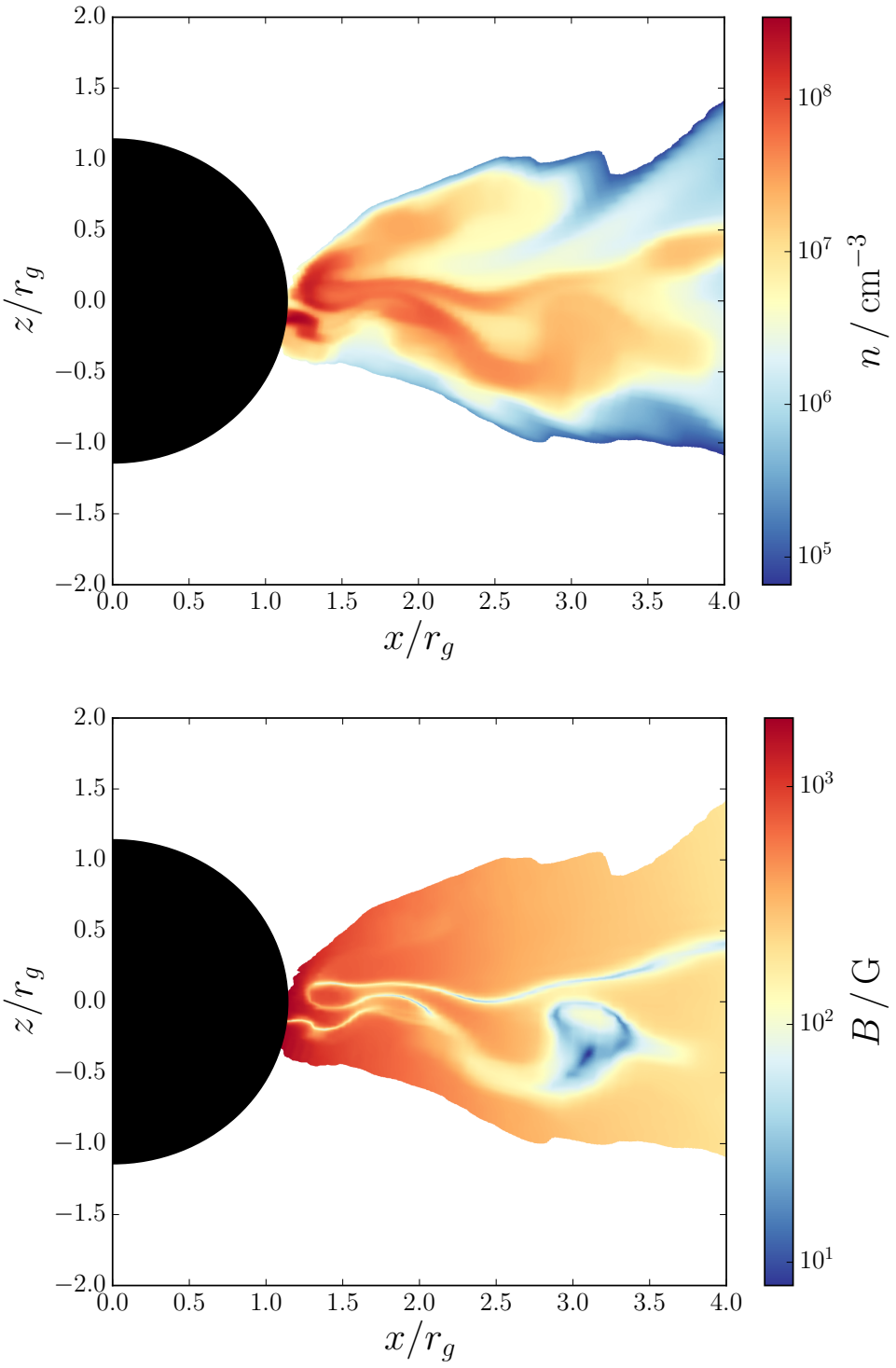

FIGURE 5.2: Snapshot of the GRMHD model at $t = 15700\,M$. The top panel shows the comoving electron number density and the bottom panel shows the comoving magnetic field strength. The white regions correspond to floor material which has been removed. Clearly, there are fluctuations in both n and B on scales smaller than r_g.

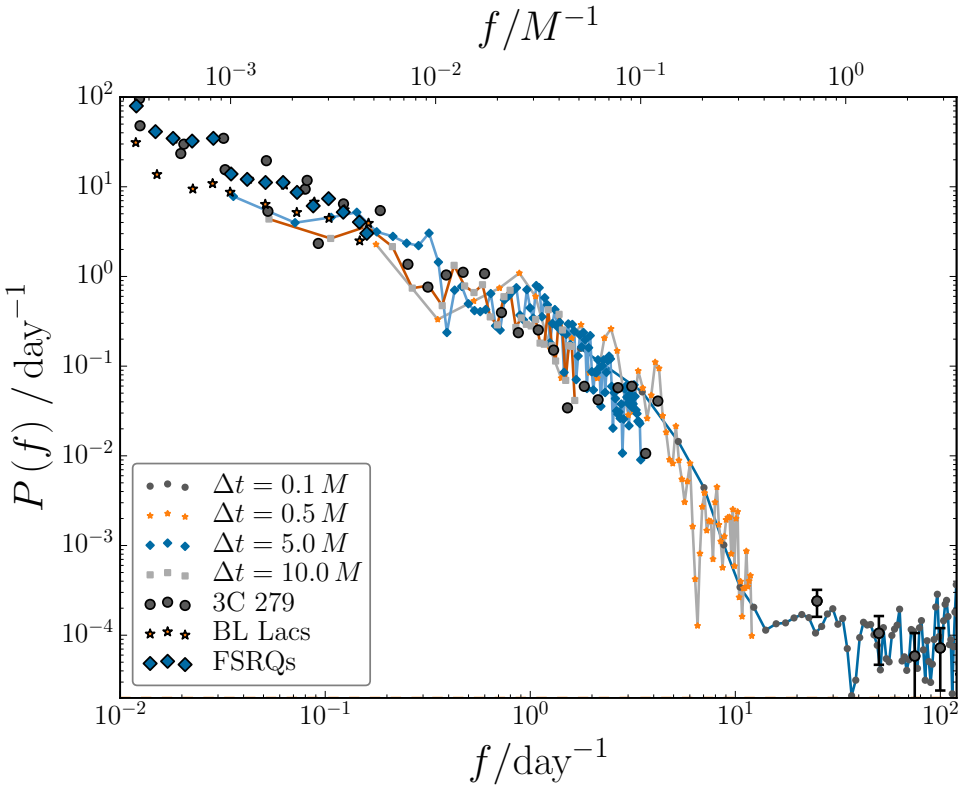

FIGURE 5.3: γ-ray PDS corresponding to four lightcurves frequency-integrated between $\nu_{\min} = 10^{19}$ Hz and $\nu_{\max} = 10^{24}$ Hz. The time steps show the sampling of each lightcurve. The circles correspond to observational data from 3C 279 (Ackermann et al., 2016), while the stars and diamonds correspond to data averaged over BL Lacs and FSRQs (Abdo et al., 2010). The observational data corresponds to energies > 100 MeV. Both BL Lacs and FSRQs show similar power-law behaviour, and the simulated PDS agrees reasonably well with both of these. There is a clear cut-off in the spectrum above $\sim 5\,\mathrm{day}^{-1}$. The white noise part of the spectrum above $10\,\mathrm{day}^{-1}$ is due to poor photon statistics. Note that the top axis is scaled to a black hole mass of $M = 5 \times 10^8\,M_\odot$ for comparison with the data for 3C 279, while the averaged data from Abdo et al. (2010) corresponds to systems with different masses. The normalization on the y-axis is arbitrary, and simply chosen for comparing the shape of our simulated PDS to the observations.

5.4 Results

For a thermal electron distribution, the synchrotron power radiated in the co-moving frame scales as $P_{\mathrm{syn}} \sim \int \mathrm{d}V\, nB^2\Theta^2$, where $\mathrm{d}V = \sqrt{-g}\,\mathrm{d}x^r\,\mathrm{d}x^\theta\,\mathrm{d}x^\phi$, $g = \det(g_{\mu\nu})$ is the metric determinant, n is the electron number density, B is the magnetic field, $\Theta = kT/mc^2$ is the electron temperature, and all fluid quantities are measured in the fluid frame. In Figure 5.1 we show a snapshot of the fluid

data at $t = 15700\,M$. The white region aligned with the spin axis corresponds to the numerical floor material that has been removed from the funnel. We plot the quantity $nB^2\Theta^2$, which is proportional to the comoving synchrotron power per unit volume. Clearly, the synchrotron emission in this model is strongly dominated by the inner $\sim 5\,M$. Similarly, the synchrotron self-Compton component originates in a compact region close to the black hole. Therefore, the variability in the resulting lightcurves is dominated by the turbulent, highly magnetized plasma in the inner parts of the MAD. Since the emission is dominated by fluid at small radii, there is no significant Lorentz boosting of the radiation.

In the top panel of Figure 5.2 we show a snapshot of the comoving electron number density close to the black hole horizon. In the bottom panel we show the corresponding comoving magnetic field strength. The flow is turbulent, and there are significant fluctuations in the fluid properties extending down to spatial scales much smaller than M. Notably, there are structures in the density apparent on scales $\lesssim 0.5\,M$, and structures in B apparent on scales of $\lesssim 0.1\,M$ due to a polarity change of the poloidal magnetic field. The resolution of our numerical model means that we can only resolve such small scale structures close to the horizon. However, we expect that similar sub-M features could be produced by turbulent processes operating at large radii. In particular, if such inhomogeneities are produced at large distances in a highly-magnetized, relativistic jet, it is plausible that they could contribute significantly to variability on very short timescales.

The PDS for real signal $h(t)$ is $P(f) = 2\left|\hat{h}(f)\right|^2$, where $\hat{h}(f)$ is the Fourier transform of $h(t)$ and the frequency range is $0 \leq f < \infty$ (see e.g., Press et al., 1986). To numerically estimate the PDS, we follow a similar procedure to that described in Wellons et al. (2014). To reduce noise, we divide each lightcurve into two segments and average the resulting power spectra. Furthermore, to suppress leakage between frequency bins,we apply a Hann window to each segment (e.g, Press et al., 1986). In practise, we use the implementation provided by the "welch" function in the SciPy Python module (Jones et al., 2001). In Figure 5.3 we show the PDS calculated from four γ-ray lightcurves (frequency integrated between 10^{19} and 10^{24} Hz) with time steps ranging from $0.1\,M$ to $10\,M$. The resulting PDS is

not particularly sensitive to the sampling of the lightcurves, with good agreement in regions of overlap. These γ-rays result from inverse-Compton scattering by hot electrons in the jet launching region. For comparison with observations, the bottom axis shows the frequency in units of day^{-1}, while the top axis shows the frequency in units of inverse light-crossing time, normalized to a black hole mass of $M = 5 \times 10^8\, M_\odot$. We have also included data for 3C 279 from Ackermann et al. (2016) as well as the average PDS for 6 BL Lacs and 9 FSRQs from Abdo et al. (2010). Note that the scaling of the top axis is appropriate for comparison with the 3C 279 data, while the Abdo et al. (2010) data is averaged over different masses. Remarkably, our simulated PDS is largely consistent with the data from both BL Lacs and FSRQs (including 3C 279) below $f \sim$ few day^{-1}. This result is suggestive of a connection between blazar variability and turbulence in the jet launching region of MADs. Note that since we are primarily interested in the scaling with f, the normalization of the y-axis is arbitrary, and simply chosen to ease comparison between the shape of our simulated PDS and the data. Also, since the overall magnitude of the PDS is probably sensitive to the prescription for treating the electron temperature, a detailed investigation of the normalization is beyond the scope of the this work.

The rough power law behaviour below $f \sim$ few day^{-1} changes to a cutoff at high frequencies. The location of this cutoff is likely affected both by the spatial resolution of the fluid data, and the photon statistics of the radiative transport calculation. Furthermore, the spectrum transitions to a flat white noise section above 10 day^{-1}. This is clearly due to poor photon statistics on the shortest timescales. That is, the magnitude of the γ-ray variability is overwhelmed by fluctuations due to photon statistics at timescales shorter than $\sim M$. In Figure 5.4 we show one of the γ-ray lightcurves with $\Delta t = 0.1\, M$. Clearly, the variability on short times is significantly affected by noise in the radiative transport calculation. The $\Delta t = 0.1\, M$ lightcurve corresponds to our highest resolution simulations, tracking $\sim 10^7$ photons per time step, and so improving upon this would be too computationally expensive. In any case, our "fast-light" assumption limits the reliably of the radiative transport results on timescales shorter than $\sim M$.

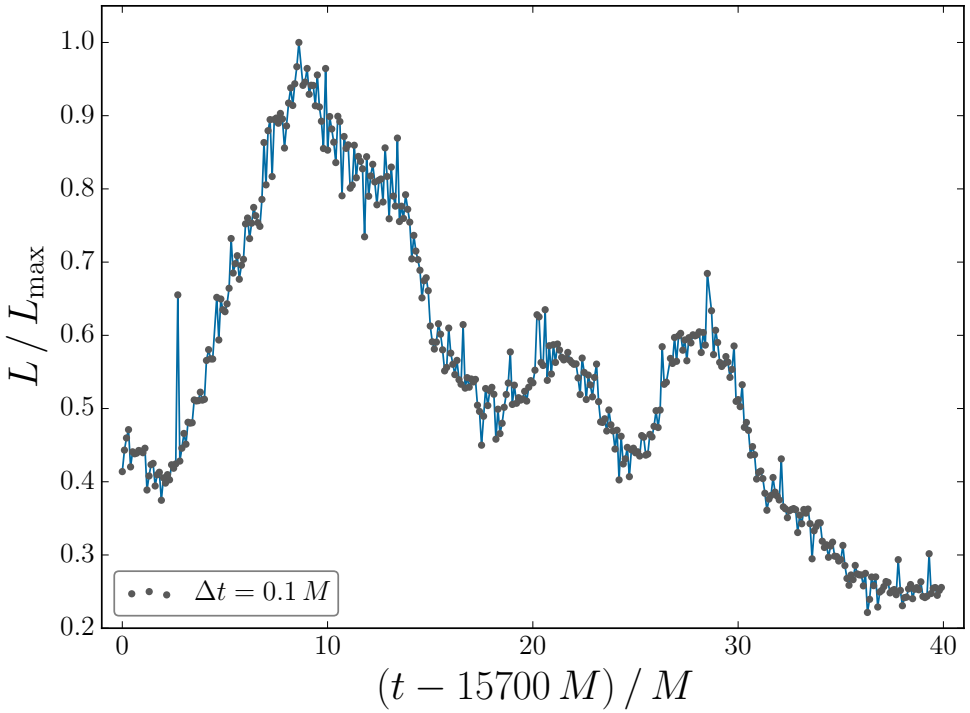

FIGURE 5.4: γ-ray lightcurve (frequency-integrated between 10^{19} and 10^{24} Hz) with a high temporal resolution of $\Delta t = 0.1\,M$. Although each time step corresponds to tracking $\sim 10^7$ photons, variability on timescales shorter than $\sim$ few M is significantly affected by noise due to photon statistics.

In Figure 5.5 we show the PDS in the optical band. In this case the radiation is primarily due to synchrotron emission. Interestingly, the variability in the optical band is the same as that in the γ-rays. Recently, Goyal et al. (2017) found that the γ-ray PDS in PKS 0735+178 is somewhat flatter than the corresponding PDS in the optical and radio bands. They speculate that this discrepancy is due to additional stochastic processes which only affect the inverse Compton component. We will investigate this interesting observation in a future work.

5.5 Summary and Discussion

As a step towards understanding the origin of variability in blazars, we calculated the temporal dependence of optical and γ-ray radiation from the jet launching region in a MAD accretion flow. In this work, we are concerned with two main

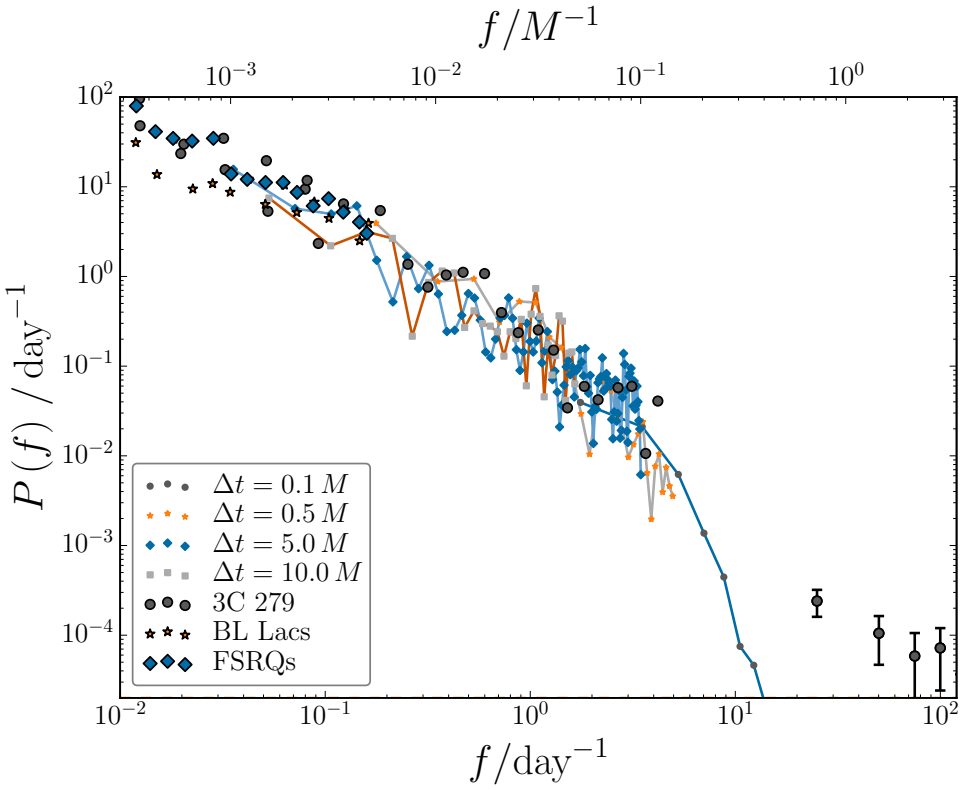

FIGURE 5.5: Same as Figure 5.3 but showing the simulated PDS for the optical band. In this case, the lightcurves are dominated by synchrotron emission. The observational data again corresponds to energies $> 100\,\mathrm{MeV}$. It is clear that optical PDS shows a similar power-law behaviour to that in the γ-rays.

properties of the observed variability. Namely, (i) that the variability can be described by a PDS of power-law shape across the entire observed frequency range, and (ii) the very fast variability observed in some sources, which can be significantly shorter than the light-crossing time of the supermassive black hole. We argue that turbulence in the highly-magnetized plasma of a relativistic jet can plausibly account for both of these properties.

The radiation from our model is dominated by turbulent plasma close to the black hole. The optical band is dominated by synchrotron emission, while the γ-rays are produced by inverse-Compton scattering from hot electrons. Both the optical and γ-ray lightcurves show variability which can be characterized by a PDS with a power-law shape below $f \sim$ few day^{-1}. Remarkably, the power-law section of our simulated PDS quantitatively reproduces the PDS observed in both BL Lacs and FSRQs. This is suggestive of a connection between turbulent processes in

MADs and the observed variability properties of blazars. Furthermore, we find the same power-law index for both the optical and γ-ray lightcurves, implying that the variability properties should not be particularly sensitive to the underlying emission mechanism.

We also showed that the turbulent flow in the jet launching region naturally produces structures on spatial scales much smaller than the horizon radius. Such small scale structures, if produced at large distances in the highly-magnetized, relativistic jet, would likely produce significant short timescale variability, although it is indeed possible that the extremely fast variability in some sources might require additional microphysics to inject energy into the plasma on small scales (e.g., Giannios et al., 2009; Narayan & Piran, 2012). Based on these results, and assuming that the turbulence in the jet launching region persists to large radii, we argue that turbulence in the relativistic jet is responsible for the observed variability in blazars over many orders of magnitude in frequency.

While we have focussed on blazars, we expect the results presented here to also be applicable in a range of systems that can be modelled as a radiatively inefficient accretion flow. In particular, our results could be appropriate for Sgr A* and the low-hard state in XRBs, although observing variability in XRBs on timescales comparable to the light-crossing time of the black hole would be extremely challenging. It would also be interesting to see how our results might change in the super-Eddington MAD regime, which could be important for describing ultra-luminous X-ray sources (Sądowski et al., 2013; McKinney et al., 2014, 2015; Sądowski & Narayan, 2015; Narayan et al., 2017).

Our model has some limitations which prevent direct application in general, especially to systems with large luminosities. Firstly, while our model might be applicable in its current form to some low-luminosity systems, the fact that the radiation originates from close to the black hole means that it is likely inappropriate for directly explaining the observed γ-rays from high-luminosity sources. As discussed in appendix A, the γ-ray radiation from high-luminosity systems (such as 3C 279) cannot originate from close to the black hole since this region is too

compact. Such a compact region would be subject to a very large pair opacity and so the emitted γ-rays would not escape to infinity. This implies that the γ-rays likely originate from a region with a significant bulk Lorenz factor Γ i.e., a relativistic jet. If we assume that the intrinsic variability in the jet at large radii matches our results for the inner jet launching region, then the observed variability should follow the same power-law, although shifted to higher frequencies by the Doppler factor $\mathcal{D} = (\Gamma\,(1 - \beta\cos\theta))^{-1}$. The Lorentz boosting would also affect the overall normalization of the PDS, which we have not considered here since the scaling of the y-axes in Figures 5.3 and 5.5 is arbitrary.

Secondly, the current work is limited by our assumption of a thermal distribution of electrons and by our simplified treatment of the electron thermodynamics. In reality, the electron distribution in highly-magnetized regions of the plasma likely has a high-energy non-thermal tail due to acceleration either by shock waves (e.g., Sironi et al., 2015) or magnetic reconnection (e.g., Sironi & Spitkovsky, 2014). These non-thermal electrons would contribute significantly to the observed radiation at very high energies. Furthermore, the details of the electron physics in radiatively inefficient accretion flows (e.g., Narayan & McClintock, 2008; Yuan & Narayan, 2014) remains a highly active area of research (Ressler et al., 2015; Foucart et al., 2016; Sądowski et al., 2017). We will incorporate more complicated models of the electron physics in a future work. Therefore, although our model reproduces the variability properties quite well, the lack of non-thermal particles and large bulk Lorentz factor means that we cannot quantitatively reproduce the wide range of observed blazar spectra.

As mentioned previously, we have used a "fast-light" approximation in which the snapshots of the fluid data are treated as time-independent during the radiative transport calculation. We will relax this approximation in a future work in order to study variability on shorter timescales in greater detail.

We conclude by noting that a thorough investigation of the γ-ray zone in blazars will require more detailed microphysical modelling for treating the electrons, as

well as global GRMHD simulations of self-consistent jet launching and propagation to large distances, with sub-M grid resolution at large radii. Recent MHD simulations investigated the large scale structure of galactic jets propagating in an ambient medium (Tchekhovskoy & Bromberg, 2016; Barniol Duran et al., 2017), however, resolving small scale structures in both the inner accretion flow and the jet at large distances is currently too computationally expensive.

Chapter 6

Observational Signatures of Mass-Loading in Jets Launched by Rotating Black Holes

6.1 Overview

It is widely believed that relativistic jets in X-ray binaries and active-galactic nuclei are powered by the rotational energy of black holes. This idea is supported by GRMHD simulations of accreting black holes, which demonstrate efficient energy extraction via the BZ mechanism. However, due to uncertainties in the physics of mass-loading, and the failure of GRMHD numerical schemes in the highly-magnetized funnel region, the matter content of the jet remains poorly constrained. In this chapter, we investigate the observational signatures of mass-loading in the funnel by performing general-relativistic radiative transfer calculations on a range of 3D GRMHD simulations of accreting black holes. We find significant observational differences between cases in which the funnel is empty and cases where the funnel is filled with plasma, particularly in the optical and X-ray bands. In the context of Sgr A*, current spectral data constrains the jet filling only if the black hole is rapidly rotating with $a \gtrsim 0.9$. In this case, the limits on the infrared

flux disfavour a strong contribution from material in the funnel. We comment on the implications of our models for interpreting future Event Horizon Telescope observations. We also scale our models to stellar-mass black holes, and discuss their applicability to the low-luminosity state in X-ray binaries.

This chapter is based on work published in O' Riordan et al. (2018).

6.2 Introduction

GRMHD simulations of highly-magnetized, accreting black hole systems typically show the formation of a tenuous, force-free funnel region aligned with the spin axis of the black hole. As discussed in chapter 1, however, due to well-known problems with GRMHD codes in this region, the resulting particle mass and internal energy densities cannot be accurately determined by the simulations. Although the particle content of the force-free funnel does not affect the dynamics, it might have important radiative contributions and so must be considered when comparing GRMHD models with observations.

In this chapter, we investigate the observational effects of mass-loading in the force-free jet. We restrict our analysis to the case where the funnel material is highly-magnetized with $\sigma \gtrsim 10$ (recall that the magnetization σ is defined to be the ratio of the magnetic energy density to the mass energy). In the opposite regime where the inertia of the funnel plasma cannot be neglected ($\sigma \lesssim 1$), Globus & Levinson (2013) showed that mass and energy loading of the field lines can strongly suppress or even switch off energy extraction from the black hole. This case would therefore involve significant modifications to the dynamical GRMHD models. We will study the observational consequences of this regime in a future work.

The structure of this chapter is as follows. In section 6.3 we briefly describe our GRMHD models, radiative transport code, and prescriptions for treating the electrons in the jet. In section 6.4 we show the spectra from our GRMHD models

and describe the observational effects of mass-loading the funnel. In section 6.5 we summarise and discuss our findings. Throughout this chapter we use units where $G = c = 1$, which implies that the gravitational radius r_g and light-crossing time $t_g = r_g/c$ become $r_g = t_g = M$. We will occasionally reintroduce factors of c for clarity.

6.3 Models

6.3.1 GRMHD Simulations

We consider six MAD accretion flows from Tchekhovskoy et al. (2011) and McKinney et al. (2012), and a SANE accretion flow from McKinney & Blandford (2009). Five of our MAD models have a scale height of $H/R \approx 0.2$ and spins of $a = \{0.1, 0.2, 0.5, 0.9, 0.99\}$. These are called A0.1N100, A0.2N100, A0.5N100, A0.9N100, and A0.99N100 in McKinney et al. (2012). We will refer to these as our "thin-MAD" models. We also consider a very geometrically-thick MAD model with $H/R \approx 1$ and a spin of $a = 0.9375$, called A0.94BfN40 in McKinney et al. (2012). We will refer to this model as "thick-MAD". Finally, we consider a SANE model with $H/R \approx 0.2$ and a spin of $a = 0.92$, called MB09D in McKinney et al. (2012).

In Figure 6.1 we show snapshots of our MAD and SANE models. The colour shows the mass density and the black contours show the structure of the poloidal magnetic field (from the ϕ-integrated vector potential). The top panel shows the thin-MAD model with $a = 0.99$, the middle panel shows the thick-MAD model with $a = 0.9375$, and the bottom panel shows the SANE model with $a = 0.92$. The MAD models have large-scale, ordered poloidal fields in the disk and jet, while the disk in the SANE model has a more disordered field. In all models, we remove material from cells near the poles as coordinate singularities can cause numerical issues here. This is indicated as an excised region along the z-axis in Figure 6.1. Detailed descriptions of these models can be found in McKinney &

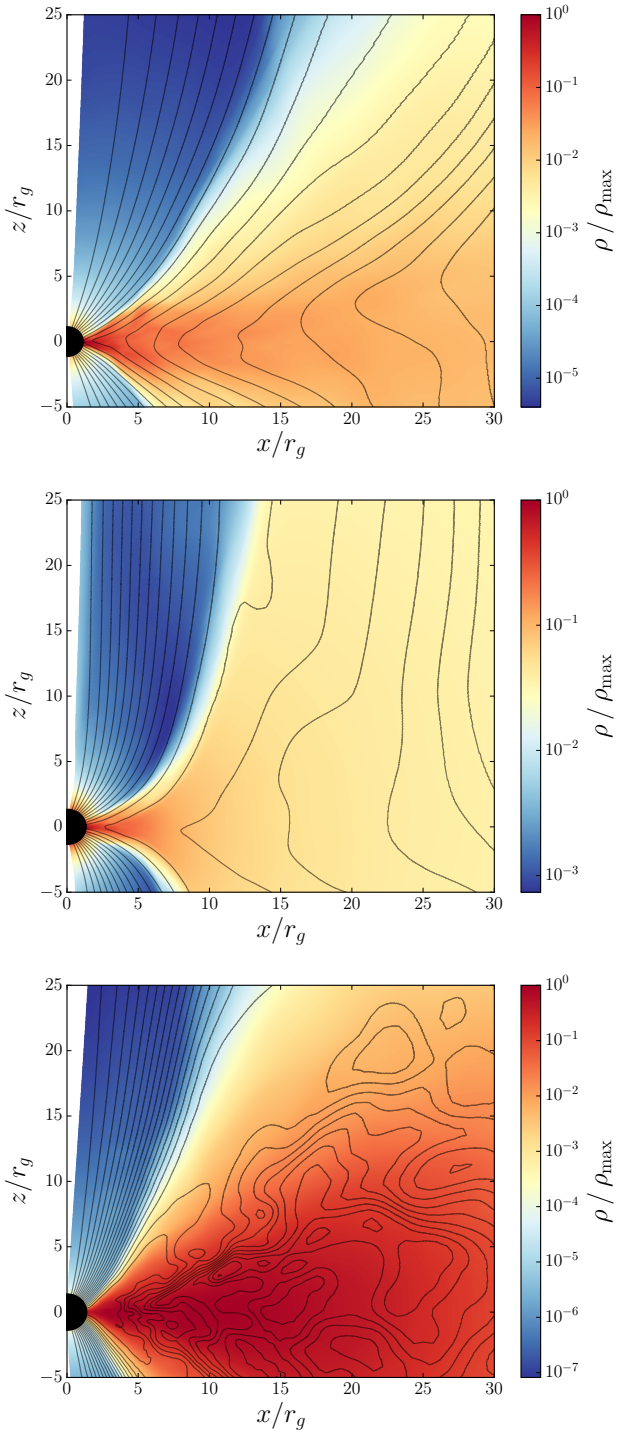

FIGURE 6.1: Snapshots of our MAD and SANE GRMHD models. The colour shows the mass density and the poloidal magnetic field lines are represented by the black contours. The top panel shows the thin-MAD model with $H/R \approx 0.2$ and $a = 0.99$. The middle panel shows the thick-MAD model with $H/R \approx 1$ and $a = 0.9375$. The bottom panel shows the SANE model with $H/R \approx 0.2$ and $a = 0.92$. Both MAD models have large-scale ordered poloidal fields in the disk and jet. The white regions along the z-axis correspond to material that has been removed to avoid numerical issues due to coordinate singularities. The blue regions roughly correspond to the numerical density floors, which are removed in our "empty" funnel models.

Blandford (2009); Tchekhovskoy et al. (2011); McKinney et al. (2012); O' Riordan et al. (2016b,a).

6.3.2 Electron Temperature Prescription

We calculate the spectra from these models in a post-processing step using a general-relativistic radiative transport code based on `grmonty` (Dolence et al., 2009). We use snapshots from the GRMHD simulations as input, and include contributions to the spectra from synchrotron emission, absorption, and Compton scattering from relativistic thermal electrons. The mass accretion rates in our low-luminosity target applications of Sgr A* and the low/hard state in XRBs are expected to be well below the corresponding Eddington rate, which justifies treating the radiation in a post-processing step. The Eddington rate is defined as $\dot{M}_{\rm Edd}c^2 \equiv 10\,L_{\rm Edd} \approx 10^{39}\left(\frac{M}{M_\odot}\right)\,{\rm erg\ s^{-1}}$ (Narayan & McClintock, 2008). Since differences in mass density and magnetization can cause different heating and cooling rates for the protons and electrons in the disk and jet (e.g., Ressler et al., 2015; Foucart et al., 2016), we specify the proton-to-electron temperature ratio $\mathcal{T} \equiv T_p/T_e$ as a function of the plasma $\beta \equiv p_{\rm gas}/p_{\rm mag}$. Here, $p_{\rm gas}$ is the thermal pressure of the fluid, and $p_{\rm mag}$ is the magnetic pressure. In order to maximize the potential contributions from the highly-magnetized funnel material, unless otherwise specified, we choose a critical value of $\beta_c = 0.2$ and set $\mathcal{T} = \mathcal{T}_{\rm disk} = 30$ in regions where $\beta > \beta_c$, and $\mathcal{T} = \mathcal{T}_{\rm jet} = 3$ in regions where $\beta \leq \beta_c$. For simplicity, we will refer to regions with $\beta \leq \beta_c$ as the "jet", and regions with $\beta > \beta_c$ as the "disk". In particular, the "jet" includes both the funnel wall and central funnel matter. Although the choice of β_c is somewhat arbitrary, we find that using $\beta_c = 0.2$ gives a reasonable distinction between the disk and jet, and our results are largely unaffected by small changes in β_c up to a factor of a few. We impose a smooth, exponential transition between the temperature ratios in the disk and jet by setting $\mathcal{T} = \mathcal{T}_{\rm jet}\,e^{-\beta/\beta_c} + \mathcal{T}_{\rm disk}\left(1 - e^{-\beta/\beta_c}\right)$.

6.3.3 Empty Funnel Prescription

To maintain numerical stability, GRMHD codes must inject material into the low-density, highly-magnetized, funnel region. In particular, numerical errors accumulate when the magnetization becomes large $\sigma = b^2/\rho \gg 1$. Here, $b^2 = b^\mu b_\mu$, b^μ is the magnetic four-field, and ρ is the rest-mass density. The magnetic four-field can be written in terms of the lab-frame 3-field B^i as $b^\mu = h^\mu_\nu B^\nu / u^t$, where u^μ is the fluid four-velocity and $h^\mu_\nu = \delta^\mu_\nu + u^\mu u_\nu$ is a projection tensor. In our units, the magnetic pressure is related to the magnetization by $p_{\rm mag} = \sigma\rho/2$. The injected floor material roughly corresponds to the blue regions in Figure 6.1. Although the injected numerical density floors do not affect the dynamics, they can be artificially hot and so might affect the resulting spectra. In O' Riordan et al. (2016b,a), we considered the case where material from the central regions of the funnel doesn't contribute significantly to the observed spectrum. That is, we removed the floor material such that the middle of the funnel region was empty. In this chapter, we follow the same procedure for removing the floor material and will refer to the resulting models as "empty". For removing the floors, we set the density to zero in regions where $\sigma > \sigma_c\,(r)$. We use $\sigma_c = 20$ at the horizon, and linearly interpolate to $\sigma_c = 10$ at $r = 10\,r_g$. For larger radii, we use a fixed value of $\sigma_c = 10$. This ensures that the injected floors are removed, without removing material close to the black hole which naturally becomes highly magnetized. Using this prescription, the centre of the funnel region is removed while the disk and funnel wall are not affected. The dashed lines in Figure D.1, which we will refer to as the "edge" of the funnel wall, show the regions that are removed using this prescription.

6.3.4 Filled Funnel Prescription

We also consider the case where the funnel is mass-loaded and will refer to these models as "filled". When modelling the filled funnel, we restrict our attention to the regime in which the mass-loading of the jet doesn't affect the magnetic field

in the funnel. In covariant form, the energy and momentum exchange between an electromagnetic field and charged matter can be written as $\nabla_\mu T^{\mu\nu}_{\rm EM} = -F^{\mu\nu} j_\nu$, where ∇_μ is the covariant derivative, $T^{\mu\nu}_{\rm EM} = F^{\mu\alpha} F^{\nu}{}_{\alpha} - \frac{1}{4} g^{\mu\nu} F_{\alpha\beta} F^{\alpha\beta}$ is the electromagnetic stress-energy tensor, $F^{\mu\nu}$ is the electromagnetic field tensor, j^μ is the electric four-current density, and $g_{\mu\nu}$ is the metric. In the case where the plasma energy-momentum is many orders of magnitude less than that of the electromagnetic field, the energy and momentum exchange can be neglected. In this case, the electromagnetic stress-energy tensor is conserved by itself $\nabla_\mu T^{\mu\nu}_{\rm EM} = 0$. Such a situation is referred to as force-free because of the vanishing of the Lorentz four-force density $f^\mu = F^{\mu\nu} j_\nu$. The approximately force-free solution in the funnel will be preserved as long as the injected matter has $\sigma \gg 1$ (McKinney & Gammie, 2004). In this regime we can treat the funnel mass-loading in a post-processing step. More significant mass-loading with $\sigma \lesssim 1$ would affect the fluid dynamics and could even quench the BZ jet (Globus & Levinson, 2013). In the case of a strongly mass-loaded funnel, the resulting GRMHD solution may deviate significantly from the models described here.

Various processes have been proposed which act to fill the funnel with electron-positron ($e^\pm$) or electron-proton (e-p) pairs, however the physical mechanism which operates in nature to mass-load jets remains an open problem. GRMHD simulations typically show the formation of a surface near the black hole which separates the inflowing and outflowing plasmas. This "stagnation" surface is continuously evacuated, resulting in large unscreened electric fields. Therefore, the stagnation surface might be the location of $e^\pm$ pair formation and subsequent acceleration (Levinson & Rieger, 2011; Broderick & Tchekhovskoy, 2015). Furthermore, depending on the radiation field produced by the inner regions of the accretion flow, the funnel might be filled with $e^\pm$ pairs via photon annihilation (Mościbrodzka et al., 2011). While these mechanisms both result in $e^\pm$ jets, there are also magnetohydrodynamic processes which might fill the jet with e-p pairs. These include magnetic Rayleigh-Taylor instabilities in the funnel wall (McKinney et al., 2012, and appendix D), and magnetic field polarity inversions in the disk Dexter et al. (2014). Both of these processes inject matter from the disk into the centre of the

funnel. In this work, we do not specify a mass-loading mechanism, but instead consider the limiting cases of an empty funnel and a funnel filled with constant profiles of mass and internal energy density. We set the density and internal energy to be as large as possible, while still satisfying the force-free condition. Therefore, we expect the spectra from mass-loaded force-free jets to fall between the extremes considered here.

For our filled models, we first remove the floor material using the procedure described above, and then fill the empty funnel cells at each radius with constant mass and internal energy densities, equal to their corresponding values at the edge of the funnel wall (denoted by the dashed lines in Figure D.1). We then re-scale the material in the funnel and funnel wall to conserve energy. In practice, this re-scaling has little effect on the resulting spectra. Using this procedure, the properties of the plasma in the funnel are determined by the self-consistent material in the funnel wall. The resulting matter distribution in the funnel is in fact similar to the original floor material shown in Figure 6.1. However, we choose to manually fill the funnel to avoid any potential issues with artificially hot cells, which would otherwise have to be checked and removed as in Chan et al. (2015b). We show the mass and internal energy density distributions in our empty and filled models in Figure D.1.

6.4 Results

6.4.1 Predictions for Spectra of Sgr A*

To scale our GRMHD models to Sgr A*, we set the black hole mass to be $M = 4 \times 10^6 M_\odot$ (Gillessen et al., 2009) and adjust the mass accretion rate so that the resulting flux at 230 GHz is roughly consistent with the observational data. This emission likely originates from within a few Schwarzschild radii of the supermassive black hole (Doeleman et al., 2008), a region which is well resolved by the GRMHD simulations and has reached a quasi-steady state. In Figure 6.2 we show spectra

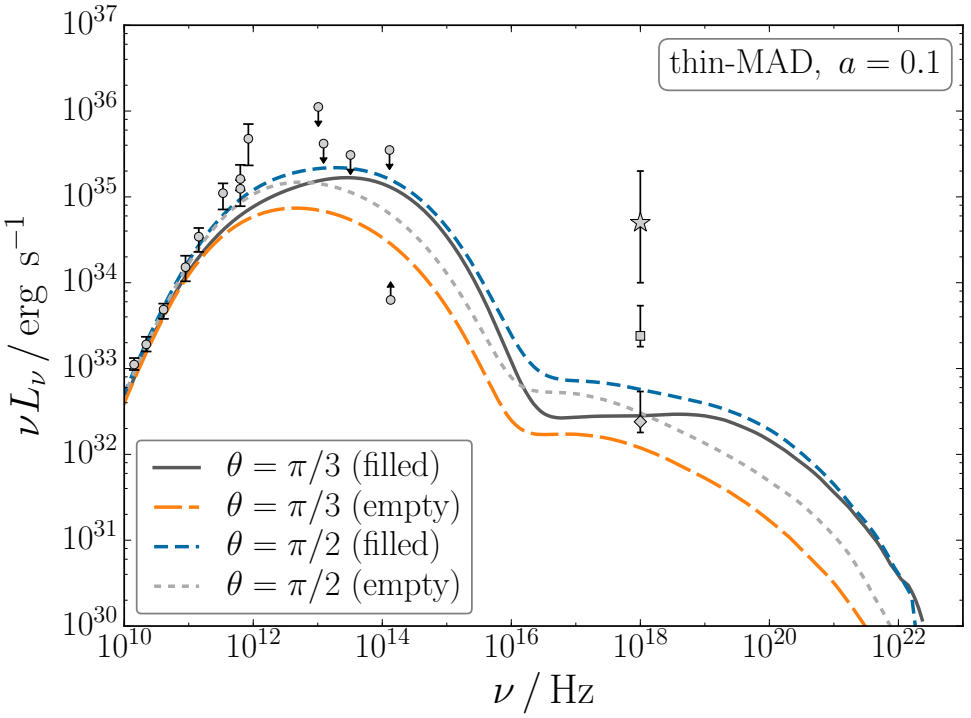

FIGURE 6.2: Comparison of the spectra for the empty and filled funnel thin-MAD models with $a = 0.1$. The radio data points and IR limits are the same as those considered by Chan et al. (2015b). The X-ray flux during quiescence is marked by the square data point (Baganoff et al., 2003), while the diamond marks 10% of the quiescent X-ray flux (Neilsen et al., 2013). The range of observed X-ray flares is represented by the star Neilsen et al. (2013). The radio emission originates in the funnel wall and so is not sensitive to the mass-loading of the funnel. The funnel material primarily contributes to the IR and optical bands, with a corresponding increase in the synchrotron self-Compton component. In this low-spin case, both the empty and filled funnel models are largely consistent with the data.

from the thin-MAD model with a black hole spin of $a = 0.1$, for two different observer inclinations of $\theta = \pi/2$ (perpendicular to the spin axis), and $\theta = \pi/3$. The "empty" model corresponds to the case where the funnel material does not contribute significantly to the observed spectra. In this case, we have removed all the plasma from the centre of the funnel and so the emission originates in the accretion disk and in the funnel wall. The "filled" model corresponds to the extreme case where the funnel is filled with constant profiles of mass and internal energy densities. The values are chosen to be equal to those at the edge of the funnel wall.

The radio data points and IR limits are the same as those considered by Chan et al.

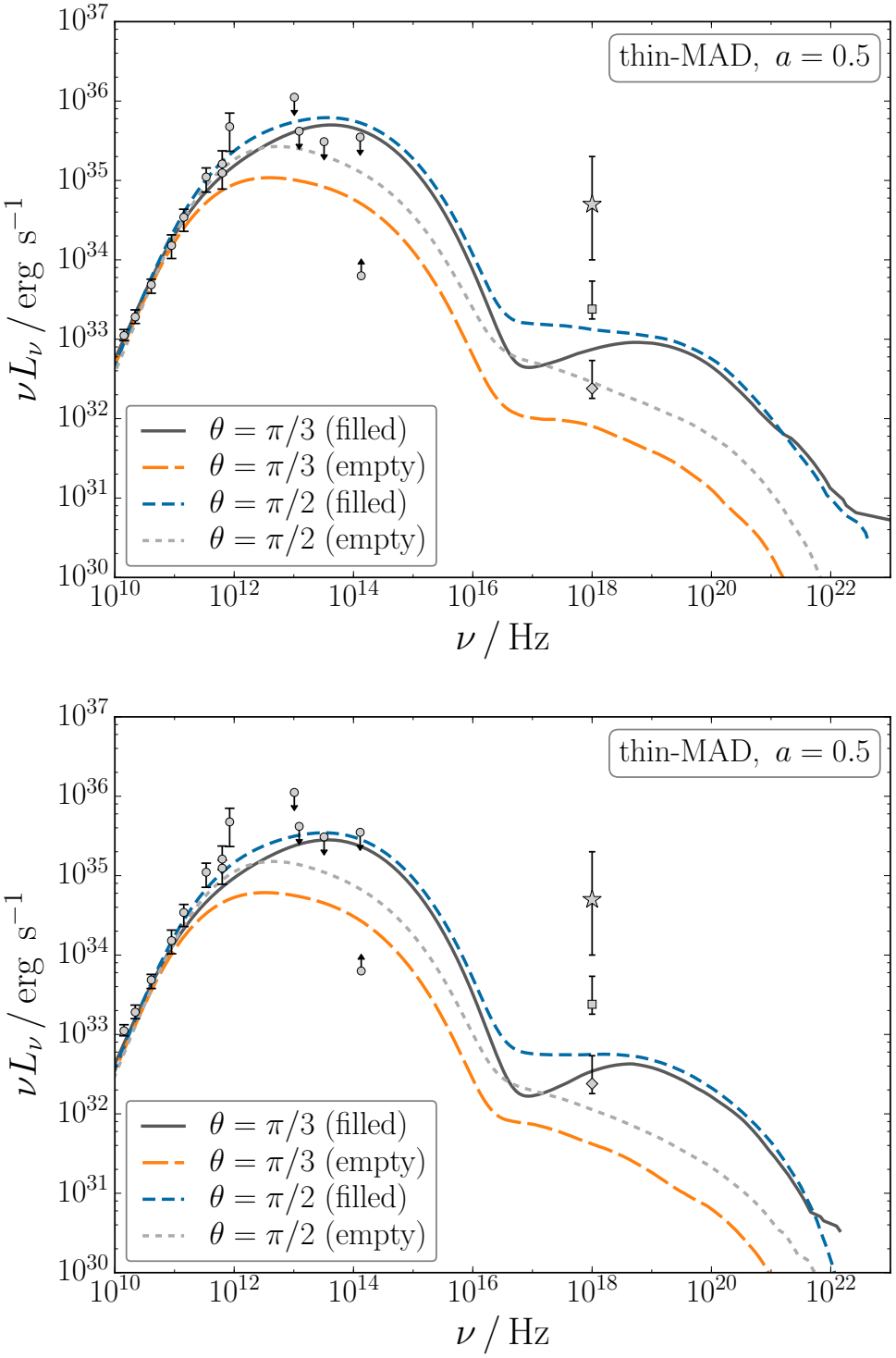

FIGURE 6.3: Spectra for the thin-MAD model with $a = 0.5$. The spectra are qualitatively similar to the $a = 0.1$ case, but with a larger contribution from the funnel material. To obtain better fits with the filled model, the accretion rate in the bottom panel has been decreased by a factor of ~ 1.5 relative to that in the top panel. Although both the empty and filled funnel models are consistent with the data, the IR emission in the filled funnel case is close to the maximum flux allowed by observations.

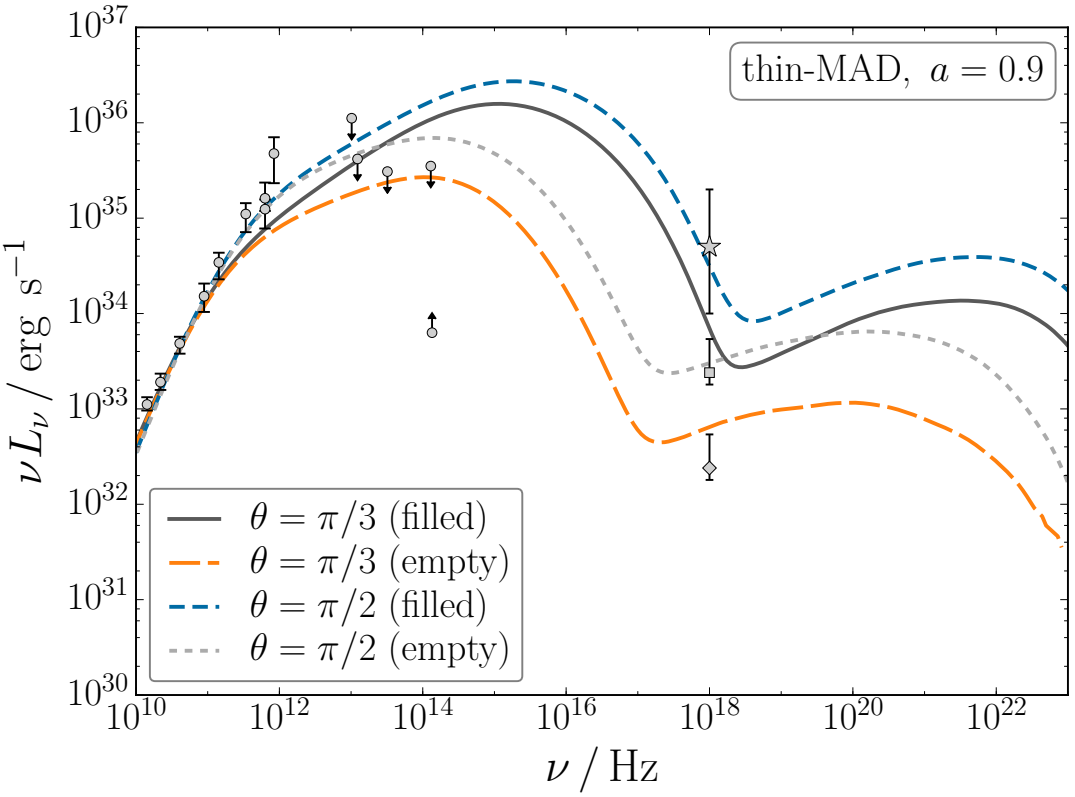

FIGURE 6.4: Spectra for the thin-MAD model with $a = 0.9$. In this case the IR limits and X-ray estimates disfavour a filled funnel component. Even the empty funnel case is approaching the limits of the observations. While a lower accretion rate would decrease the IR and X-ray flux towards values more consistent with the data, the radio flux would then be missed by a large amount.

(2015b). In particular, the IR limits represent the highest and lowest observed fluxes. The X-ray flux during quiescence is marked by the square data point (Baganoff et al., 2003). The diamond marks 10% of the quiescent X-ray flux, which is the estimated contribution from the inner accretion flow (Neilsen et al., 2013). The range of observed X-ray flares is represented by the star and corresponding error bars Neilsen et al. (2013).

The mass accretion rate in Figure 6.2 is set such that the average rate at the horizon is $\dot{M} \approx 10^{-7}\dot{M}_{\rm Edd}$. Interestingly, the radio emission at frequencies $\nu \lesssim 10^{12}$ Hz is not sensitive to the mass-loading of the funnel. This is because this emission is dominated by the funnel wall. This is consistent with the findings of Mościbrodzka et al. (2014), who refer to this region as the "jet sheath". Although there is a clear increase at IR and optical frequencies relative to the empty funnel case, both the

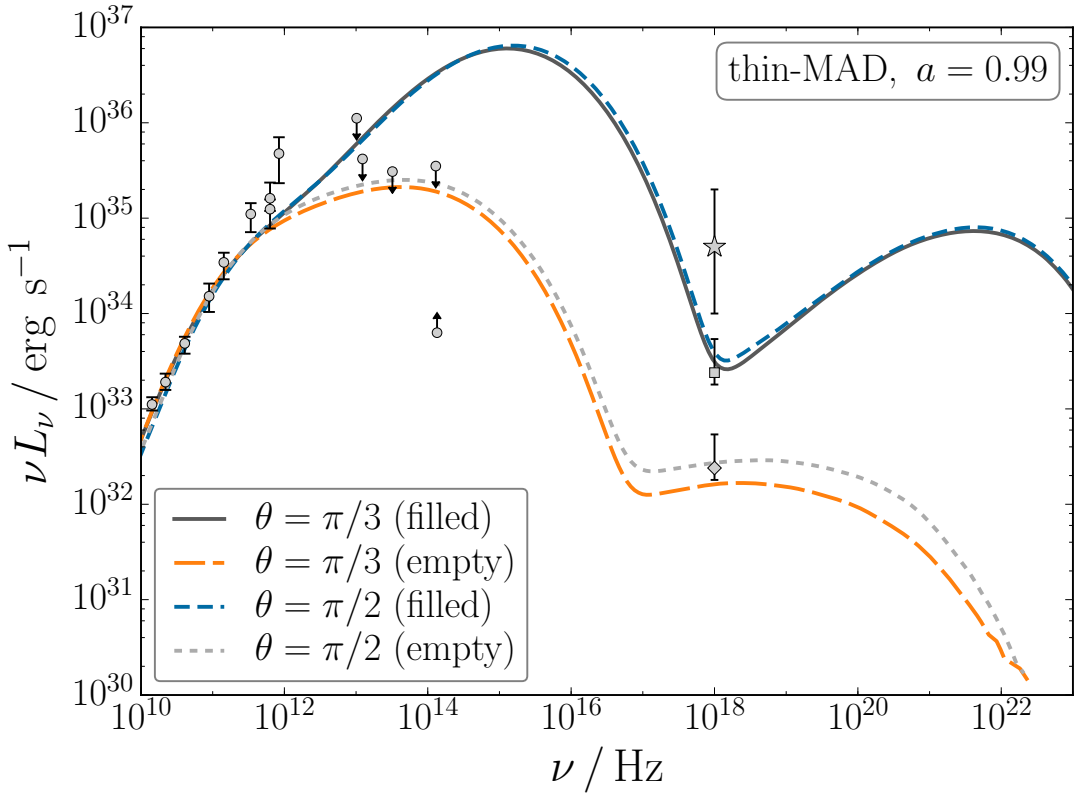

FIGURE 6.5: Spectra for the thin-MAD model with $a = 0.99$. As with the $a = 0.9$ case, the IR and X-ray data disfavour the filled funnel model. Furthermore, fitting the empty funnel model to the data requires suppressing the emission from close to the horizon by increasing the proton-to-electron temperature ratio of the inflowing material.

empty and filled funnel models are largely consistent with the data.

In Figure 6.3 we show the spectra for the higher-spin case of $a = 0.5$. The spectra are qualitatively similar to those in Figure 6.2, however the enhancement at IR and optical frequencies is larger. To obtain better fits with the filled model, we reduced the accretion rate by a factor of ~ 1.5 in the bottom panel relative to the top panel. The increase in this synchrotron component causes a corresponding increase in synchrotron self-Compton emission in the hard X-rays. As with the $a = 0.1$ model, both the empty and filled funnel cases fit the data reasonably well, however, the IR flux in the filled model is very close to the upper limits on the observed flux.

In Figure 6.4 we show the thin-MAD model with $a = 0.9$. The IR and X-ray limits clearly disfavour the case where the funnel material contributes significantly

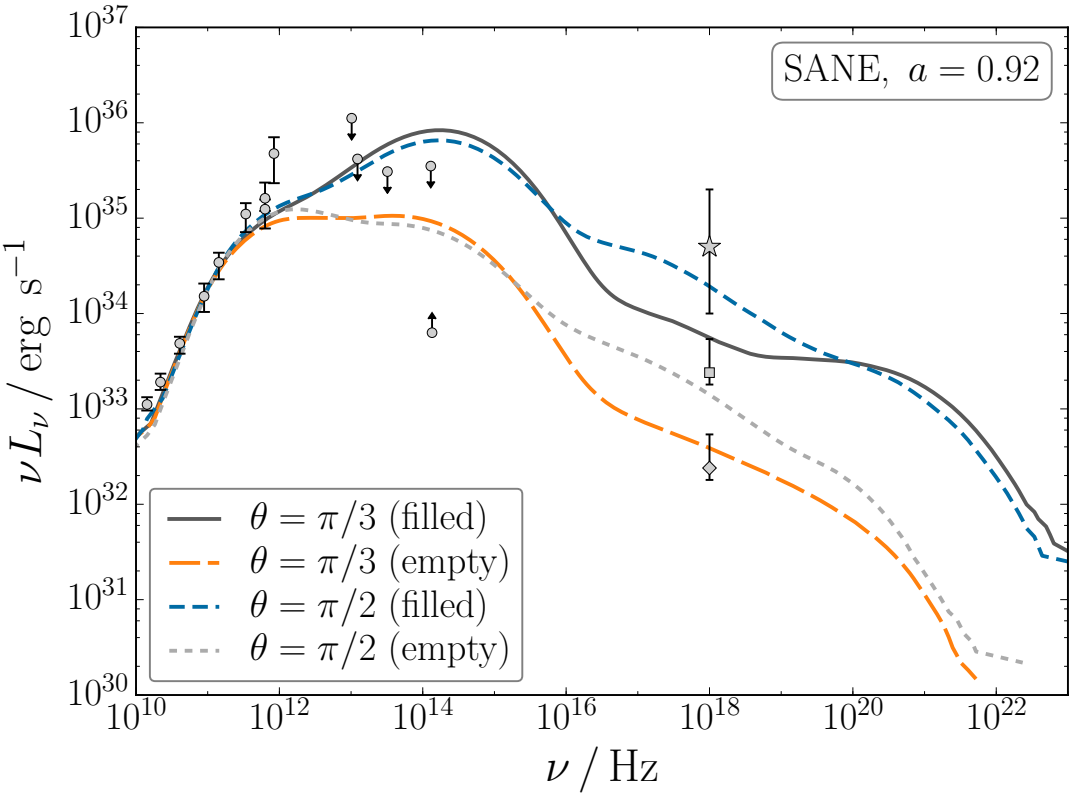

FIGURE 6.6: Spectra for the SANE model with $a = 0.92$. As in the high-spin MAD models, the IR limits disfavour models with strong funnel emission.

to the emission. Although the X-ray and IR emission can be brought within the limits by adjusting the mass accretion rate, this would also significantly reduce the radio flux which originates in the funnel wall and which is independent of the mass-loading. The difference between the empty and filled models is even more dramatic in the extreme $a = 0.99$ case, which we show in Figure 6.5. As discussed in O' Riordan et al. (2016b), the emission from this model is strongly dominated by the near-horizon plasma. In order to give reasonable fits to the data, even in the empty funnel case, we suppressed this near-horizon radiation by imposing a temperature ratio of $\mathcal{T} = 300$ on the inflowing material. A similar result was found by Chan et al. (2015b), whose best-fit MAD models have very large proton-to-electron temperature ratios in the disk.

In Figure 6.6 we show the spectra calculated from our SANE model with $a = 0.92$ and a mass accretion rate of $\dot{M} \approx 10^{-6}\dot{M}_{\rm Edd}$. This model has the same scale height of $H/R \approx 0.2$ as our thin-MAD models. As in the thin-MAD case, the radio

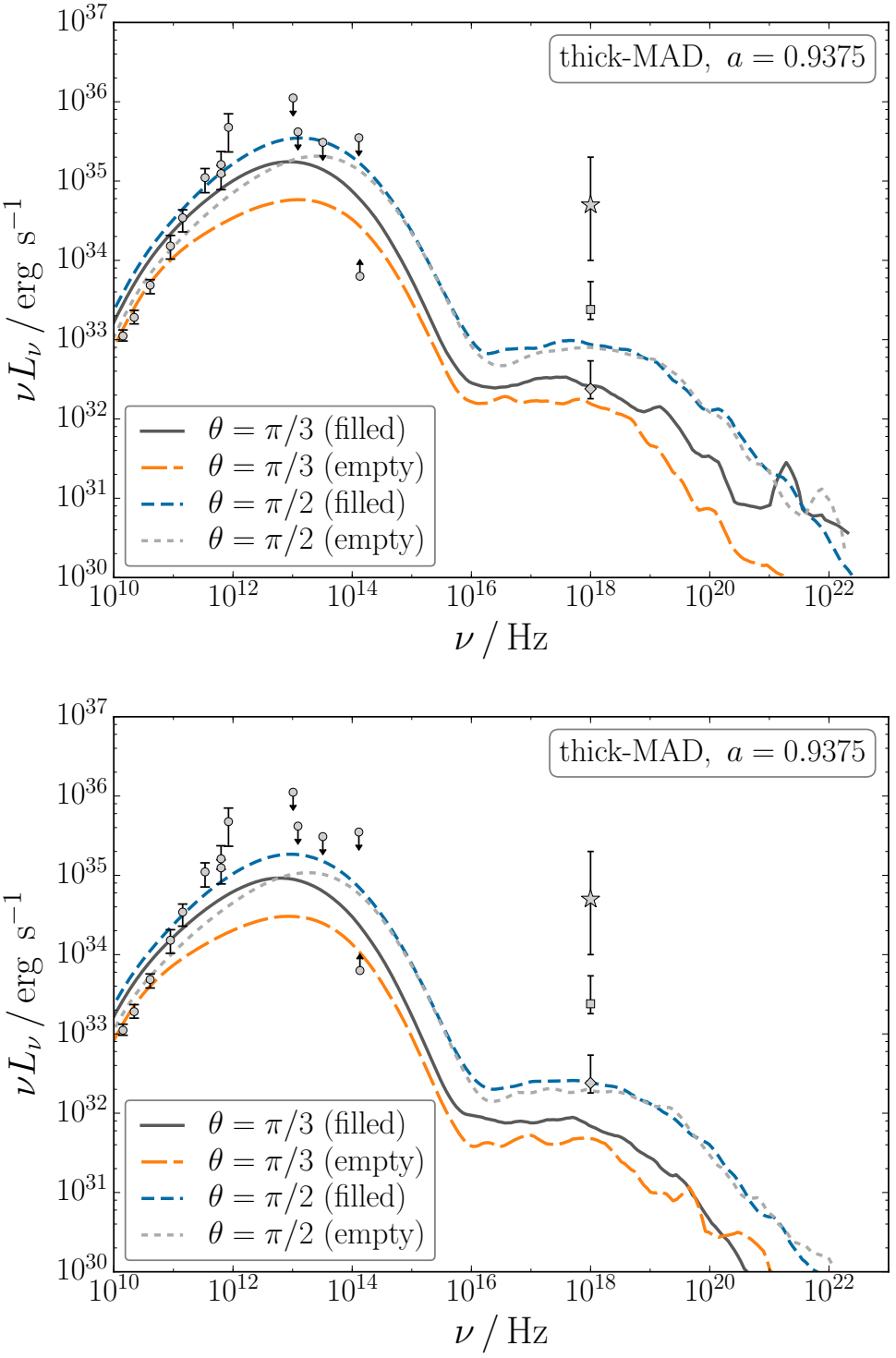

FIGURE 6.7: Spectra for the geometrically-thick ($H/R \approx 1$) MAD model with $a = 0.9375$. The accretion rate in the top panel is larger than that in the bottom panel by a factor of ~ 1.5. This model gives a poorer fit to the radio data than the geometrically thinner models. In this case, although the black hole is rotating rapidly, both the empty and filled models provide reasonably similar fits to the data. This is because the funnel emission is somewhat suppressed relative to the other models and so the difference between empty and filled funnels is less extreme.

emission is insensitive to the mass loading of the funnel. The higher mass accretion rate results in a larger optical depth, which is clearly reflected in the high-energy parts of the spectra that show multiple Compton scatterings. Interestingly, as in the high-spin MAD models, the filled funnel model significantly over-produces IR emission and so an empty funnel is favoured by the data.

To conclude, for all our thin-MAD models and our SANE model, we find that the radio flux is dominated by the funnel wall and is largely independent of the mass-loading of the jet. We also find a significantly larger IR flux in the filled models than in the empty models. From this, we expect that the ratio of the IR flux and 230 GHz flux could be used as a probe of mass-loading processes in the funnel. Furthermore, in the context of Sgr A*, although our low-spin models are consistent with the data in both empty and filled funnel cases, the higher-spin models only fit the data provided the funnel material does not contribute significantly to the observed spectrum.

In Figure 6.7 we show the spectra calculated from our thick-MAD model which has a black hole spin of $a = 0.9375$ and a very geometrically-thick disk ($H/R \approx 1$). As in Figure 6.3, the accretion rate in the bottom panel is ~ 1.5 times lower than that in the top panel. Although the emission from our thin-MAD and SANE models is dominated by the region $r \lesssim 30M$, which has reached a quasi-steady state, the outer radii of our thick-MAD model can contribute significantly to the emission. The outer radii of our GRMHD models have not had enough time to reach a steady state and so the plasma properties depend strongly on the initial conditions in the torus. Furthermore, the 230 GHz flux which we have been using to normalise our models likely originates in the inner few r_g of the accretion flow (Doeleman et al., 2008). Therefore, we follow the procedure of Shcherbakov et al. (2012) to analytically extend the fluid quantities to large radii. We extend the fluid properties at $r = 30M$ as power-laws out to the Bondi radius in order to match the estimated density and temperature for Sgr A* at this radius. We further assume an isothermal jet with electron temperature $\Theta = kT/mc^2 = 50$ (Mościbrodzka et al., 2014; Chan et al., 2015b; Gold et al., 2017), which provides a better fit to the radio emission than a constant temperature ratio for this model. The difference

between the empty and filled funnel models is smaller than in the high-spin thin-MAD and SANE cases and so both provide similar fits to the data. Contrary to the previous cases, the funnel filling primarily affects the lower-frequency emission. This is consistent with Gold et al. (2017), who found that the 230 GHz images of their models were affected by the funnel filling. We will perform a more thorough investigation of the dependence on the disk scale height and prescriptions for extending the data to the Bondi radius in a future work.

6.4.2 Predictions for Spectra of the Low/Hard State in XRBs

In this section we scale our thin-MAD models to the low luminosity state in XRBs by setting the black hole mass to $M = 10M_{\odot}$. For comparing the different GRMHD models, we fix the mass accretion rate to be $\dot{M} \approx 10^{-6}\,\dot{M}_{\rm Edd}$. To maximize the potential effects of the funnel emission, we again consider the case where the proton-to-electron temperature ratios in the disk and jet are $\mathcal{T}_{\rm disk} = 30$ and $\mathcal{T}_{\rm jet} = 3$.

In Figure 6.8 we show the spectra for the low-spin models with $a = 0.1$ and $a = 0.5$. The results are qualitatively similar to the corresponding spectra for Sgr A*, with differences in the peak frequencies and overall luminosity due to changes in the black hole mass and accretion rate. In particular, we find that the filled funnel models show enhanced hard UV/soft X-ray emission, while the optical and lower-frequency fluxes are unaffected by the mass-loading.

In Figure 6.9 we show the spectra for the high-spin models with $a = 0.9$ and $a = 0.99$. We find very large differences between the empty and filled funnel models, with the funnel contribution shifting to higher frequencies. In this case, the X-rays and γ-rays are significantly modified by the funnel matter, while frequencies below $\sim 10^{16}$ Hz are unaffected by the funnel contribution. In the $a = 0.99$ case, the radiative efficiency is large, approaching values $\gtrsim 10\%$, especially in the filled funnel model. A similar result was reported by Ryan et al. (2017), who found

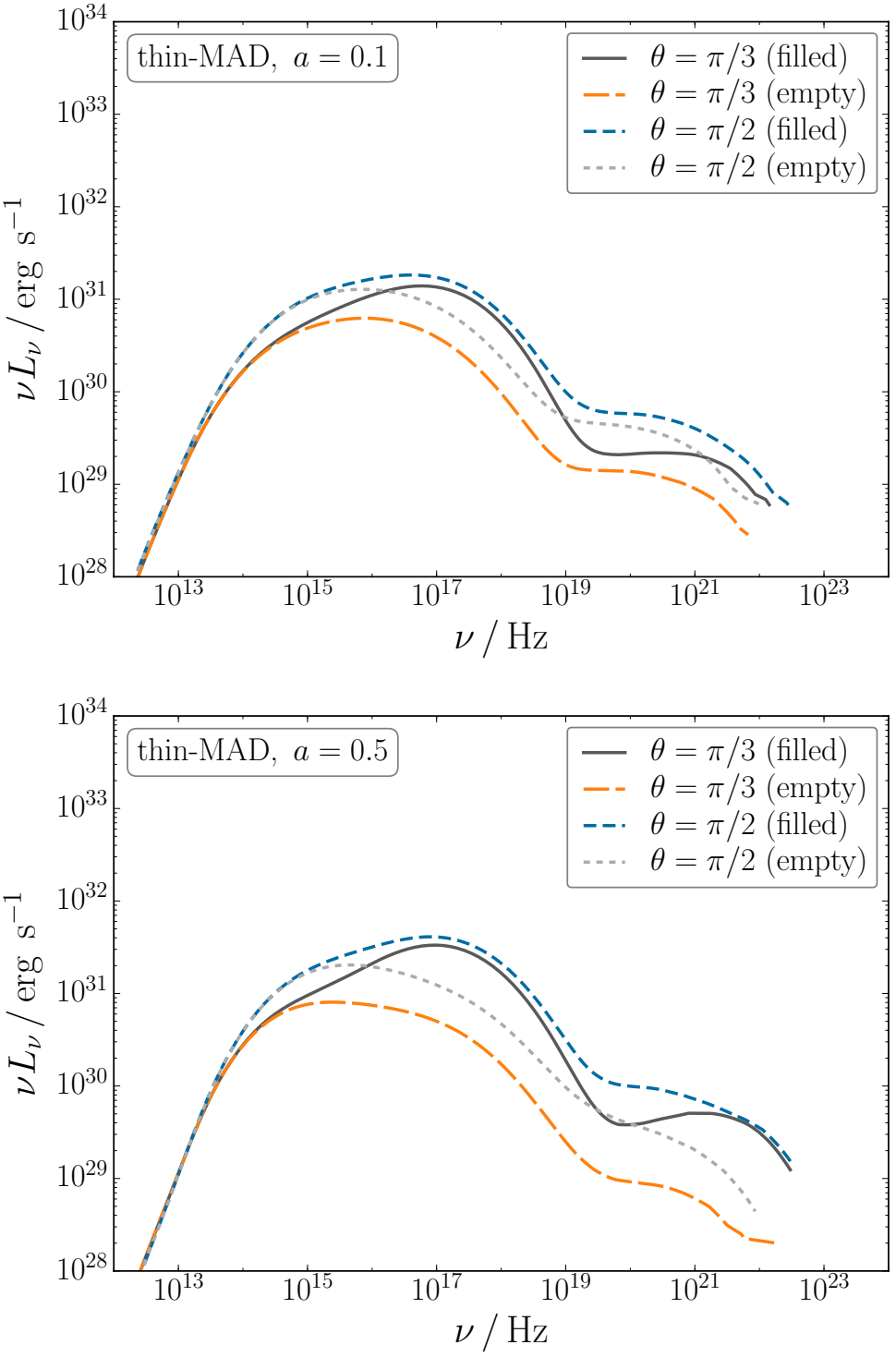

FIGURE 6.8: Spectra for thin-MAD models with $a = 0.1$ (top), and $a = 0.5$ (bottom). The black hole mass has been set to $M = 10M_\odot$. The spectra are qualitatively similar to the results for Sgr A*. The optical and lower frequency emission is insensitive to the funnel material, while the hard UV and soft X-rays are significantly enhanced relative to the empty funnel case.

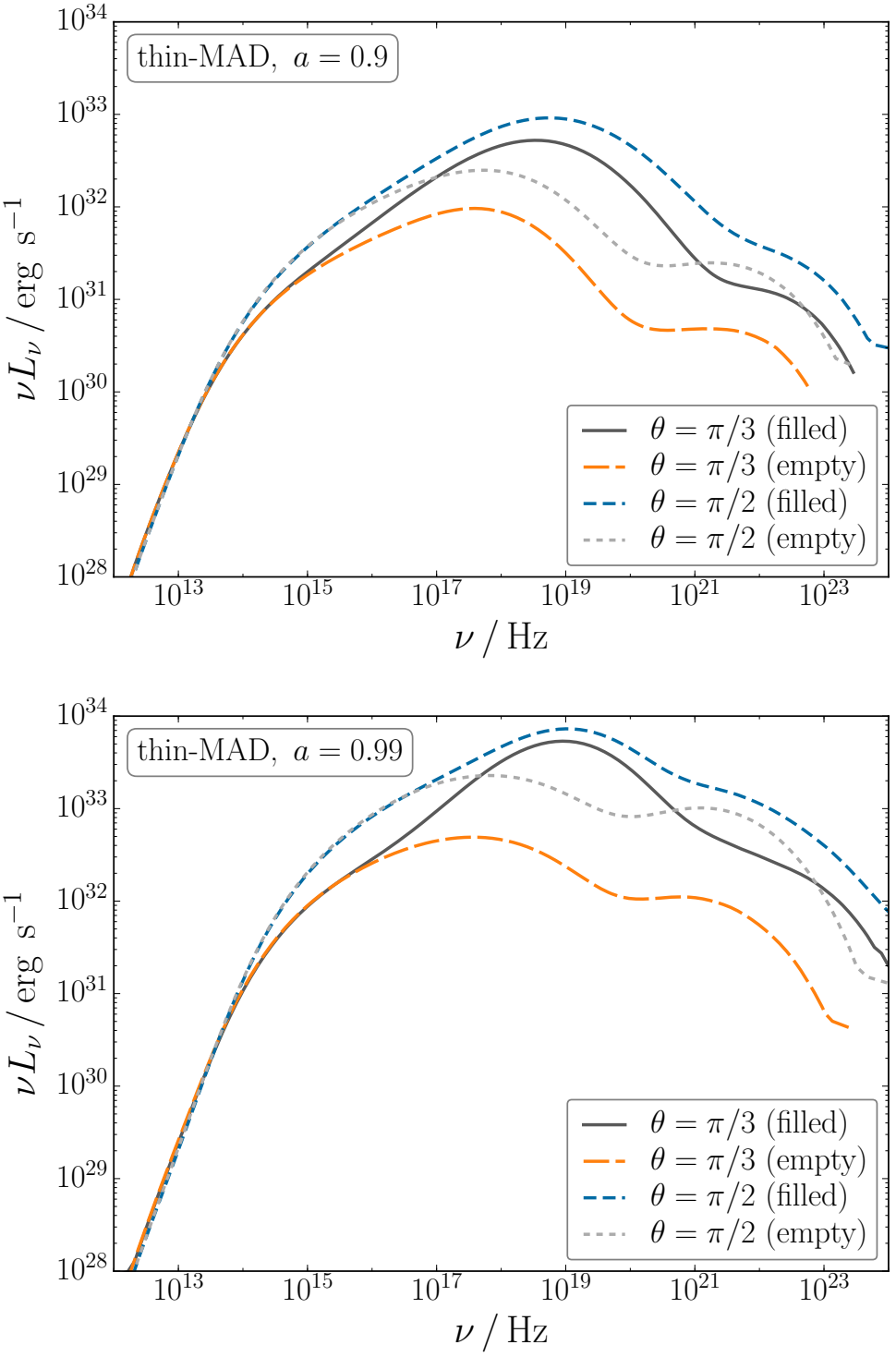

FIGURE 6.9: Spectra for the thin-MAD models with $a = 0.9$ (top), and $a = 0.99$ (bottom). The X-ray flux is significantly higher in the filled funnel models, while emission at frequencies $\lesssim 10^{16}$ Hz is unaffected by the funnel matter.

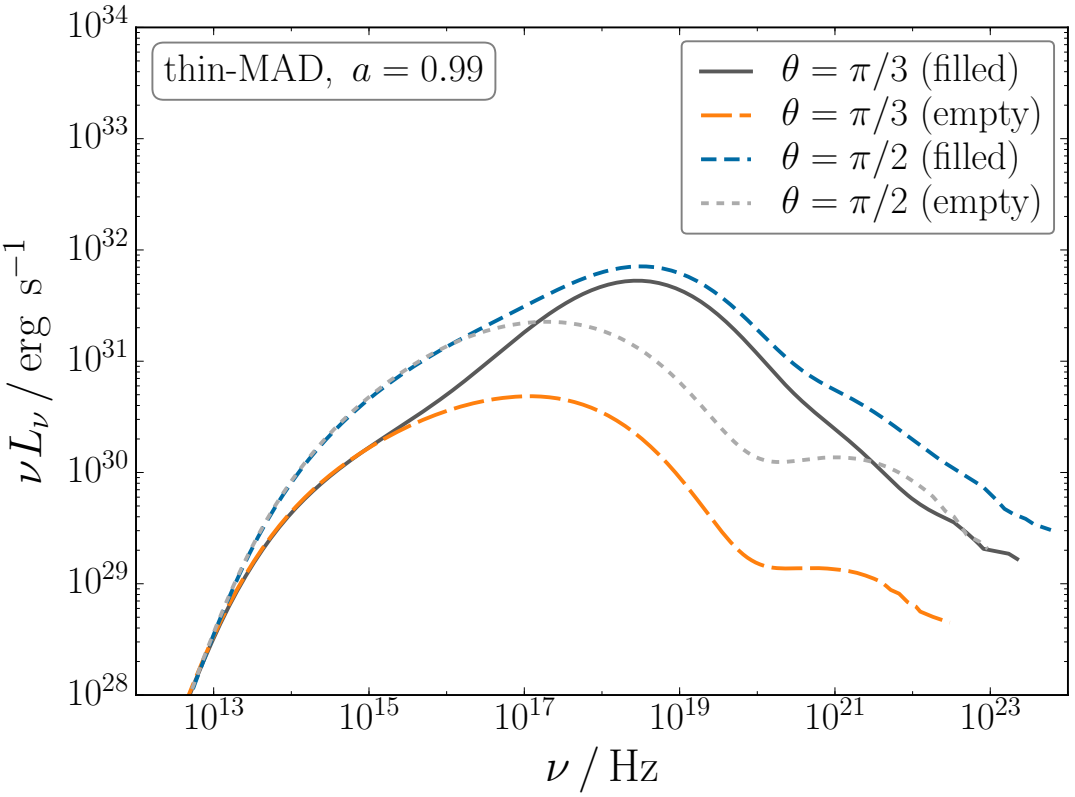

FIGURE 6.10: Same as the bottom panel of Figure 6.9, but with a lower accretion rate of $\dot{M} \approx 10^{-7}\dot{M}_{\rm Edd}$. Although the luminosity is significantly lower than in the previous case, the frequencies at which the emission is enhanced are similar. This is due to the reasonably weak dependence of the frequency on the accretion rate.

that accretion flows with $a = 0.5$ can approach 1% radiative efficiency by $\dot{M} \sim 10^{-5}\dot{M}_{\rm Edd}$. To avoid complications due to radiative cooling, we investigate a lower accretion rate of $\dot{M} \approx 10^{-7}\dot{M}_{\rm Edd}$, and show the resulting spectra in Figure 6.10. The spectra in the hard X-rays and below are qualitatively similar to those in Figure 6.9, and so our conclusions about the effects of the funnel mass-loading still hold. This is not surprising since, as shown in appendix C, although the luminosity depends very strongly on the accretion rate $L_{\rm syn} \sim \dot{M}^2$, the frequency depends only weakly on $\dot{M}$ as $\nu_{\rm syn} \sim \dot{M}^{1/2}$. There is a larger difference in the synchrotron self-Compton component due to the linear dependence of the Compton y parameter on $\dot{M}$ (see appendix C).

6.5 Summary and Discussion

In this chapter, we investigated the observational effects of mass-loading in BZ jets. We considered the case in which the plasma in the funnel remains force-free, which allowed us to treat the mass-loading in a post-processing step. We found significant differences between models with an empty funnel and models where the funnel was filled with highly-magnetized plasma. In particular, in the context of Sgr A* the IR and optical flux is enhanced relative to the empty funnel case. Interestingly, the radio emission from our thin-MAD and SANE models is dominated by the funnel wall and so is largely unaffected by the mass-loading. We identify the ratio of the IR and 230 GHz flux as a potential observational probe of the filling factor of the funnel.

As argued by Gold et al. (2017), understanding the contribution from the funnel material will be extremely important for interpreting future EHT observations of the black hole shadow in Sgr A*. They showed that the absence of significant 230 GHz emission from the funnel can appear as a "hole" in the images, mimicking features of the black hole shadow. Since the radio emission from our models is not affected by the funnel material, we expect that the mass-loading of the BZ jet will not have a large impact on images from the EHT (unless the disk is very thick with $H/R \sim 1$, as shown in Figure 6.7). This means that even mass-loaded BZ jets may appear as "holes" in images from the EHT.

We find qualitatively similar results in the context of XRBs, although shifted to higher frequencies due to changes in the black hole mass and accretion rate. It is often argued that inverse Compton emission from a corona of hot electrons surrounding the inner accretion flow is responsible for the X-ray emission observed in XRBs (e.g., Titarchuk, 1994; Magdziarz & Zdziarski, 1995; Gierlinski et al., 1997; Esin et al., 1997, 2001; Poutanen, 1998; Cadolle Bel et al., 2006; Yuan et al., 2007; Narayan & McClintock, 2008; Niedźwiecki et al., 2012, 2014; Qiao & Liu, 2015). However, there is significant degeneracy between these models and ones in which a large fraction of the X-ray emission originates in the base of the jet (e.g., Mirabel & Rodríguez, 1994; Markoff et al., 2001, 2003, 2005; Falcke et al.,

2004; Bosch-Ramon et al., 2006; Kaiser, 2006; Gupta et al., 2006; Kylafis et al., 2008; Maitra et al., 2009; Pe'er & Casella, 2009; Pe'er & Markoff, 2012; Markoff et al., 2015; O' Riordan et al., 2016a). Understanding the funnel mass-loading could be crucial for breaking this degeneracy and constraining the role of the jet in producing the observed high-energy X-ray emission in the low/hard state.

Our results have interesting implications for explaining the scatter in the fundamental plane of black hole activity (Merloni et al., 2003; Falcke et al., 2004). The fundamental plane is an empirical correlation between black hole mass, radio luminosity, and X-ray luminosity which spans the mass scale from XRBs to active galaxies. This correlation suggests that low-luminosity accreting black hole systems are scale invariant. Our results imply that differences in the jet mass-loading could contribute to the scatter about the best-fit correlation. In particular, at high black hole spin the X-ray emission can vary by more than two orders of magnitude between the empty and filled models, while the radio emission remains constant. Therefore, in addition to variations in quantities such as the mass accretion rate, black hole spin, and viewing angle, the mass-loading of the jet could play a significant role in producing the observed scatter.

For our empty funnel models, we set the plasma density in the funnel to zero. However, this case represents a wider class of models in which the funnel contains material that does not contribute significantly to the emission. For example, models in which the proton-to-electron temperature ratio in the jet is comparable to that in the disk result in similar spectra to the empty funnel cases. This is because the denser funnel wall dominates the jet component unless the plasma in the centre of the funnel is hot enough. For similar assumptions about the electron temperatures, the spectra from more complicated matter profiles in force-free jets should fall within the limits considered here. In a future work, we will investigate observational signatures of the regime where the force-free approximation breaks down. As shown by Globus & Levinson (2013), in this case the solution in the funnel can deviate significantly from the BZ funnel solutions in our dynamical models.

We have not specified a mass-loading mechanism, but have simply compared spectra from the empty funnel case to the extreme case of a steady, force-free funnel with constant mass and internal energy density profiles. As well as spectral properties, we expect that variability studies will play a key role in constraining the mass-loading physics systems such as Sgr A*. Importantly, many of the proposed mass-loading mechanisms operate on very different time-scales, and so could in principle be distinguished by the EHT. For example, pair production by vacuum gaps in the black hole magnetosphere is expected to be intermittent, and vary on timescales comparable to the light-crossing time of the black hole (Levinson & Rieger, 2011; Broderick & Tchekhovskoy, 2015). This timescale is extremely short in Sgr A*, roughly equal to one minute. However, it might be possible with the EHT to study structures in the accretion flow that vary on minute timescales (Doeleman et al., 2009a,b). This could provide valuable constraints on the physics of near-horizon mass-loading. Other mass-loading processes may operate on timescales significantly longer than the light-crossing time. For example, pairs may be produced by photon annihilation (Mościbrodzka et al., 2011) on timescales determined by radiation field of the disk. Furthermore, magnetohydrodynamic processes such as magnetic Rayleigh-Taylor instabilities in the funnel wall (McKinney et al., 2012, and appendix D), or magnetic field polarity inversions in the disk Dexter et al. (2014) can inject matter from the disk into the centre of the funnel. These processes operate on spatial scales much larger than the Schwarzschild radius, and so the corresponding variability could be resolved by future observations.

A significant limitation of the current work is our simplified treatment of the emitting electrons. In particular, we neglect the contribution from non-thermal electrons which might be present due to acceleration by shock waves (e.g., Sironi et al., 2015), magnetic reconnection (e.g., Sironi & Spitkovsky, 2014), or due to the injection process itself (e.g., Levinson & Rieger, 2011). Although these non-thermal electrons would likely affect the high-frequency emission in our spectra, including these processes would introduce additional poorly-constrained free parameters into our models, and so we neglect this contribution as a first step. We

also use a simple prescription for calculating the electron temperature by varying the proton-to-electron temperature ratio as a function of the plasma β. This ratio is a free parameter which is poorly constrained both by theory and observations. We choose values consistent with the findings of recent, sophisticated models of the electron thermodynamics in collisionless accretion flows (Ressler et al., 2015; Foucart et al., 2016; Sądowski et al., 2017), which show that the electron temperature is comparable to the proton temperature in highly-magnetized regions of the flow. Modelling the electron physics in accretion disks and jets remains an active area of research, which will hopefully be informed further by upcoming observations with the EHT.

Chapter 7

Summary and Outlook

In this thesis, we investigated the spectral and temporal radiative properties of the jet launching region in a range of accreting black hole systems. In particular, we used a general-relativistic radiative transport code to calculate the radiation resulting from state-of-the-art ideal GRMHD simulations.

In chapter 3, we studied the high-energy signatures of jets from close to the black hole in XRBs. We found clear spectral signatures of jets in the produced by overlapping jet and disk contributions. We also investigated the temporal evolution of the X-ray and γ-ray emission during a large-scale plasmoid ejection event expected during state transitions.

In chapter 4 we showed that, even in MAD systems where the BZ mechanism is operating, the resulting radiated power can deviate significantly from the predicted correlation between power radiated and black hole spin. This deviation results from the strong gravitational effects experienced by photons emitted close to the horizon of rapidly rotating black holes. We also identified the ratio of the X-ray and near-infrared power as a potential observational signature of black hole spin in the low/hard state in XRBs.

In chapter 5, we investigated the origin of blazar variability in terms of turbulence in the jet launching region of a MAD accretion flow. We found a power spectrum consistent with the observed power-law spectrum, over many decades in frequency.

Since turbulence in the flow naturally produces fluctuations in the plasma properties on scales smaller than the horizon radius, we argued that this might also explain the ultra-fast variability.

In chapter 6, we examined the observational effects of mass-loading in BZ jets. We found large spectral differences between the empty and filled funnel cases. The main effect was an enhancement in the optical and X-ray bands, while the radio emission was largely independent of the mass-loading. We discussed the implications of these results for interpreting future observations of the jet launching region in Sgr A* and M87 with the EHT.

The recent ground-breaking detection of gravitational waves from merging neutron stars (Abbott et al., 2017a), and subsequent observations of broad-band electromagnetic counterparts (Abbott et al., 2017b), makes studying the jet-launching region extremely timely for two reasons. Firstly, relativistic jets are expected to be one of the primary sources of electromagnetic radiation from binary mergers, providing important information about the immediate environment of the merging objects. Therefore, an understanding of the basic physical mechanisms operating in jets complements information obtained by modeling the gravitational wave signals, and could enhance our understanding of the formation channels and evolution of binary neutron star and black hole systems. Secondly, gravitational waves carry information about the masses and spins of the merging compact objects and post-merger system. Since these are expected to be the central engines for powering jets, independent constraints on the properties of these objects would be extremely valuable for informing theoretical models of the jet-launching process. Furthermore, breakthroughs in VLBI astronomy with the EHT, which is expected to resolve the inner accretion flows of Sgr A* and M87 on event-horizon scales next year, will probe the very heart of the jet-launching region in these systems. Combined with future high-resolution near-infrared observations of Sgr A* with the GRAVITY instrument at the Very Large Telescope (VLT), these observational advances will revolutionize our understanding of the near-horizon behaviour of accretion flows and jets in the coming years.

Appendix A

Pair Opacity

Here, we estimate constraints on the luminosity from the pair opacity. The following applies in the comoving frame of the source and follows closely the treatment of Dondi & Ghisellini (1995). High-energy γ-rays can collide with softer radiation to produce $e^{\pm}$ pairs. The cross section for this process is maximized for collisions between γ-rays of energy $x = h\nu/mc^2$ and target photons of energy $x_t = 1/x$. This maximum cross section is $\sigma = 3\sigma_T/16$ (e.g., Lang, 1980), where σ_T is the Thomson cross section. Assuming that the source is spherical and emits isotropically, the corresponding optical depth can be written in terms of the luminosity as

$$\tau_{\gamma\gamma}(x) = \frac{3\sigma_T}{16}\frac{L(x_t)}{4\pi mc^3 R} \tag{A.1}$$

Therefore, the condition that $\tau_{\gamma\gamma}(x) \lesssim 1$ constrains the luminosity of the soft radiation field to be

$$L(x_t) \lesssim 3 \times 10^{43}\, M_8 \left(\frac{R}{r_g}\right) \text{erg s}^{-1} \tag{A.2}$$

where we have written the luminosity in terms of the gravitational radius $r_g \approx 1.5 \times 10^{13}\, M_8\, \text{cm}$, and M_8 is the black hole mass in units of $10^8\, M_\odot$.

In the case of 3C 279, the observed γ-rays primarily interact with a soft (X-ray) radiation field of luminosity $L \sim 3 \times 10^{47}\, \text{erg s}^{-1}$ (Ackermann et al., 2016).

Adopting a black hole mass of $M = 5 \times 10^8\, M_\odot$ and an emission region of size $R = 5\, r_g$, we find that the luminosity of the target radiation is constrained to be below $L \lesssim 10^{45}\, \mathrm{erg\ s^{-1}}$. The obsereved luminosity is more than two orders of magnitude larger than this. Combined with the short variability timescale, we are forced to to conclude that the source of emission is strongly Doppler boosted and so likely originates in a relativistic jet.

Appendix B

Effects of Spin on the Redshift Profiles

B.1 Analytic Expression for the Redshift Factor

To understand the dependence of the redshift factor on spin, we focus on the simple case of circular motion in the r–ϕ plane. In what follows, we denote quantities in the coordinate (lab) frame with no primes on the index, in the orthonormal "zero angular momentum observer" (ZAMO) frame with one prime, and in the orthonormal fluid frame with two primes. The Killing vectors associated with stationarity and axisymmetry are $\xi^\mu = \delta^\mu_t$, and $\chi^\mu = \delta^\mu_\phi$. For circular motion, the 4-velocity can be written as $u^\mu = u^t\left(\xi^\mu + v^\phi \chi^\mu\right)$, where $v^\phi = u^\phi/u^t$. The condition that the 4-velocity be timelike, $g_{\mu\nu}u^\mu u^\nu = -1$, gives

$$u^t = \left(-g_{tt} - 2g_{t\phi}v^\phi - g_{\phi\phi}\left(v^\phi\right)^2\right)^{-1/2} \tag{B.1}$$

Defining $\mathcal{P}_i = p_i/p_t$, we can write the redshift for circular motion as (Cunningham & Bardeen, 1972, 1973; Fanton et al., 1997)

$$\mathcal{R} = \frac{1}{u^t\left(1 + v^\phi \mathcal{P}_\phi\right)} \tag{B.2}$$

The photon 4-momentum is a null vector and so, in the fluid frame, we have

$$\mathcal{P}_{r''}^2 + \mathcal{P}_{\theta''}^2 + \mathcal{P}_{\phi''}^2 = 1 \tag{B.3}$$

Therefore, $\mathcal{P}_{\phi''}$ is bounded by ± 1, corresponding to photons emitted in the $\mp\phi$ directions. The ZAMO and fluid frames are simply related by a Lorentz transformation, and so

$$\mathcal{P}_{\phi'} = \frac{\mathcal{P}_{\phi''} - v^{\phi'}}{1 - v^{\phi'}\,\mathcal{P}_{\phi''}} \tag{B.4}$$

The transformations from the Boyer-Lindquist coordinate basis to the orthonormal ZAMO basis are given by Bardeen et al. (1972)

$$e_{\nu'} = e^{\mu}{}_{\nu'}\,\partial_\mu, \qquad e^{\nu'} = e_{\mu}{}^{\nu'}\,\mathrm{d}x^\mu \tag{B.5}$$

The only non-zero components are

$$e^{t}{}_{t'} = \frac{1}{\alpha}, \quad e^{r}{}_{r'} = \frac{1}{\sqrt{g_{rr}}}, \quad e^{\theta}{}_{\theta'} = \frac{1}{\sqrt{g_{\theta\theta}}}, \quad e^{\phi}{}_{\phi'} = \frac{1}{\sqrt{g_{\phi\phi}}}, \quad e^{\phi}{}_{t'} = \Omega/\alpha \tag{B.6}$$

$$e_{t}{}^{t'} = \alpha, \quad e_{r}{}^{r'} = \sqrt{g_{rr}}, \quad e_{\theta}{}^{\theta'} = \sqrt{g_{\theta\theta}}, \quad e_{\phi}{}^{\phi'} = \sqrt{g_{\phi\phi}}, \quad e_{t}{}^{\phi'} = -\Omega\sqrt{g_{\phi\phi}} \tag{B.7}$$

where

$$\Omega = -\frac{g_{t\phi}}{g_{\phi\phi}}, \qquad \alpha = \sqrt{-g_{tt} + \Omega^2 g_{\phi\phi}} \tag{B.8}$$

Transforming from the ZAMO frame to the coordinate frame gives

$$\mathcal{P}_{\phi} = \frac{\sqrt{g_{\phi\phi}}\,\mathcal{P}_{\phi'}}{\alpha - \Omega\sqrt{g_{\phi\phi}}\,\mathcal{P}_{\phi'}} \tag{B.9}$$

$$v^{\phi} = \frac{\alpha}{\sqrt{g_{\phi\phi}}}\,v^{\phi'} + \Omega \tag{B.10}$$

Finally, the redshift for circular motion is given by equation (B.2), with $\mathcal{P}_\phi$ related to the fluid frame $\mathcal{P}_{\phi''}$ by equations (B.4) and (B.9), and v^ϕ related to the ZAMO frame $v^{\phi'}$ by equation (B.10).

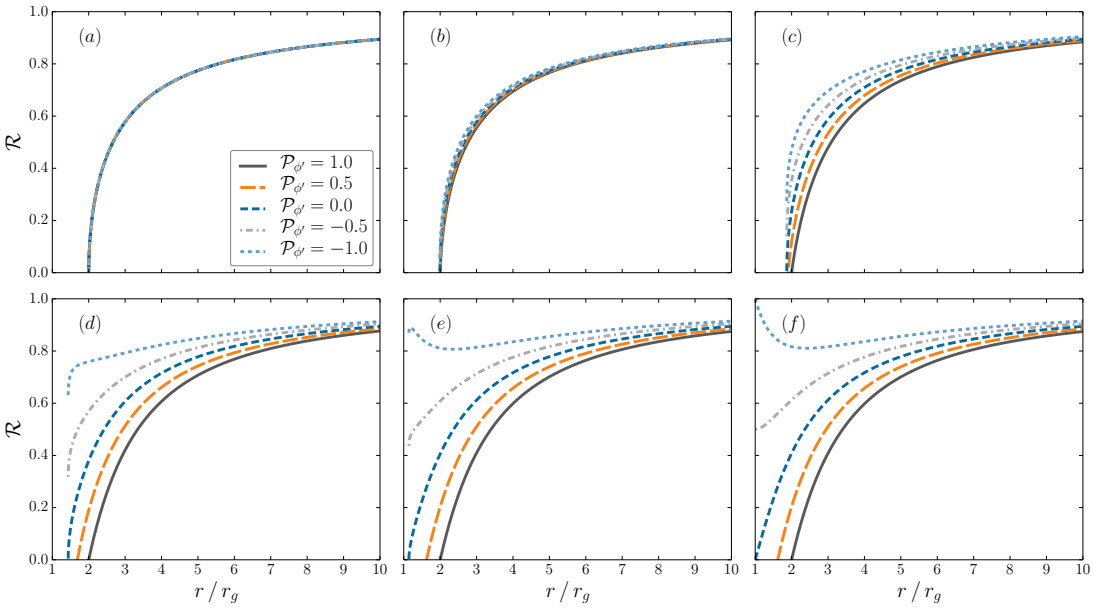

FIGURE B.1: Redshifts for a source with $v^{\phi} = \Omega$ (equation B.11). (a) : $a = 0.1$, (b) : $a = 0.2$, (c) : $a = 0.5$, (d) : $a = 0.9$. (e) : $a = 0.99$, (f) : $a = 1.0$. For high spins, photons emitted in the ϕ direction in the ZAMO frame suffer little redshift until very close to the horizon.

In the special case of a source with zero angular momentum, $v^{\phi'} = 0 \Rightarrow v^{\phi} = \Omega$, and equation (B.2) becomes

$$\mathcal{R} = \alpha - \Omega \sqrt{g_{\phi\phi}}\, \mathcal{P}_{\phi'} \tag{B.11}$$

which is simply the transformation $p_t = e_t{}^{\nu'}\, p_{\nu'}$. In Figure B.1 we show the redshift for a ZAMO (equation B.11), as a function of $\mathcal{P}_{\phi'}$, for different spins. For high spins, photons emitted in the ϕ direction (those with $\mathcal{P}_{\phi'} = -1$) suffer little redshift until right outside the horizon. In fact, for a maximally spinning black hole, $\mathcal{R} \to 1$ as $r \to r_H$. On average, observers with $\theta = \pi/2$ receive photons with larger ϕ momentum than observers located at $\theta = 0$. Therefore, observers perpendicular to the spin axis experience a flatter redshift profile and so see closer to the horizon.

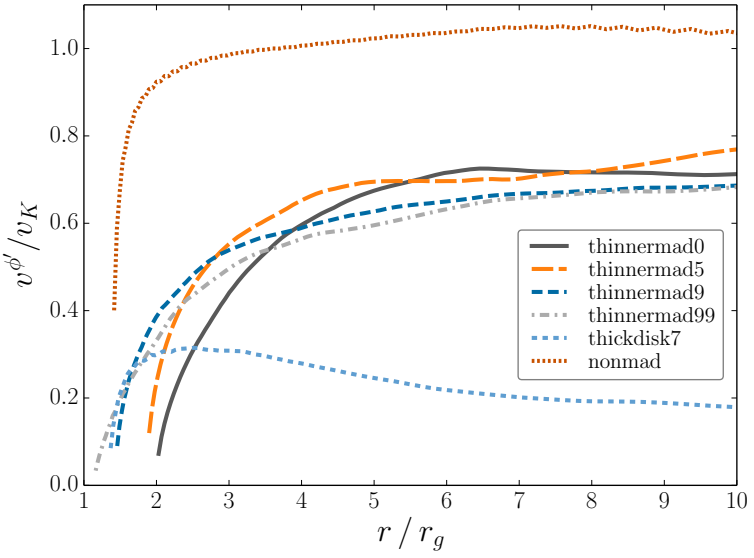

FIGURE B.2: $v^{\phi'}$ in units of v_K for different accretion models. The SANE model is roughly Keplerian, while the MAD models are all sub-Keplerian. The velocity is approximately a constant fraction of the Keplerian speed until close to the horizon. In the lab frame, frame dragging forces the fluid rotate with $v^{\phi} \to \Omega_H$ as $r \to r_H$.

B.2 Dependence on the Fluid Velocity

In general, the fluid will have a non-zero ϕ velocity in the ZAMO frame. In Figure B.2 we show $v^{\phi'}$ for different models from McKinney et al. (2012). We give the velocity in units of the Keplerian speed $v_K = 1/\sqrt{r}$. The "thinnermadx" models are those considered here (where the number x gives the spin), while the "thickdisk7" and "nonmad" models are the MAD and SANE models considered in O' Riordan et al. (2016a). These models have $a = 0.9375$ and $a = 0.92$, respectively. In all models, the ϕ velocity is approximately a constant fraction of the Keplerian speed until close to the horizon (where $v^{\phi'} \to 0$ since $v^{r'} \to 1$ in this frame). Motivated by this, we choose $v^{\phi'}$ to be proportional to v_K, and set $v^{\phi'} = 0$ at the horizon with a smooth transition at $r = r_{\rm ISCO}$. In Figure B.3 we show the effects of varying $v^{\phi'}$ for a black hole with $a = 0.9$. The difference between the observed and comoving power is a factor of $\mathcal{R}^2$. Therefore, for photons emitted in the ϕ direction in the fluid frame, the ϕ velocity contributes to a maximum factor of ~ 3. Since observed photons will have a spread of $\mathcal{P}_{\phi''}$, the average difference in power will likely be much smaller than this.

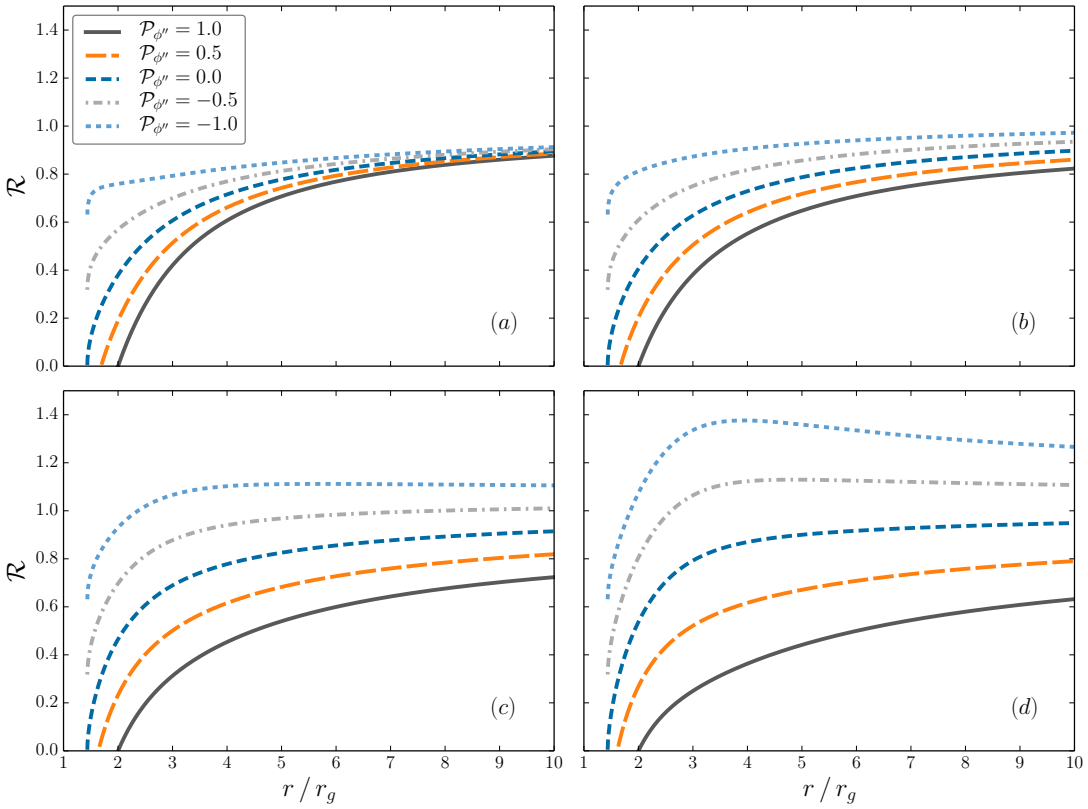

FIGURE B.3: Redshifts for a source with $a = 0.9$, and $v^{\phi'} = \epsilon\, v_K$. We set $v^{\phi'} = 0$ at the horizon, with a transition at $r = r_{\rm ISCO}$. (a) : $\epsilon = 0.0$, (b) : $\epsilon = 0.2$, (c) : $\epsilon = 0.6$, (d) : $\epsilon = 1.0$.

To test the sensitivity of the redshift factor to the accretion model, we numerically calculate redshift profiles for the "thinnermad9", "thickdisk7", and "nonmad" models. These have similar spin, but have different velocity fields (see Figure B.2 for the ϕ velocity). In Figure B.4 we show the radial velocity profiles. The radial velocities are comparable in the MAD models, however these differ significantly from the SANE case. In Figure B.5 we show the redshift profiles from the different models, for observers located at $\theta = 0$ and $\theta = \pi/2$. The $\theta = \pi/2$ case should maximize potential deviations. Despite differences in the fluid velocity, the resulting profiles are remarkably similar. In particular, the redshift is reasonably flat until very close to the horizon. Therefore, we conclude that the model-dependent velocity contribution to the described redshift effect is minor, while the main contributions are the spin and viewing angle.

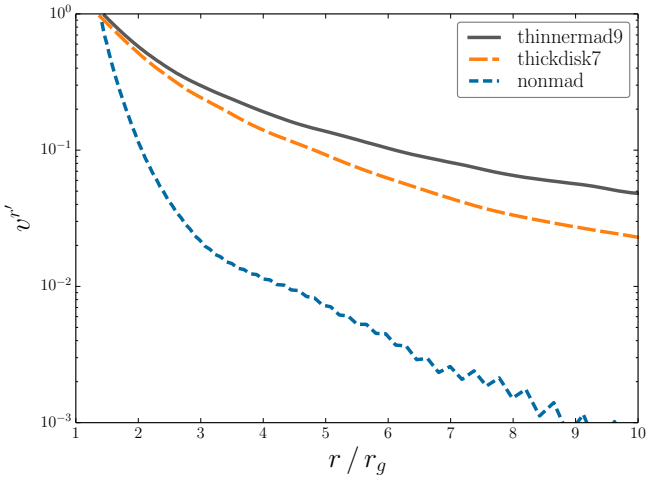

FIGURE B.4: Radial velocity in the ZAMO frame for the MAD and SANE models with similar spin. The radial velocities are comparable in the MAD case, but the velocity profile is significantly different in the SANE case.

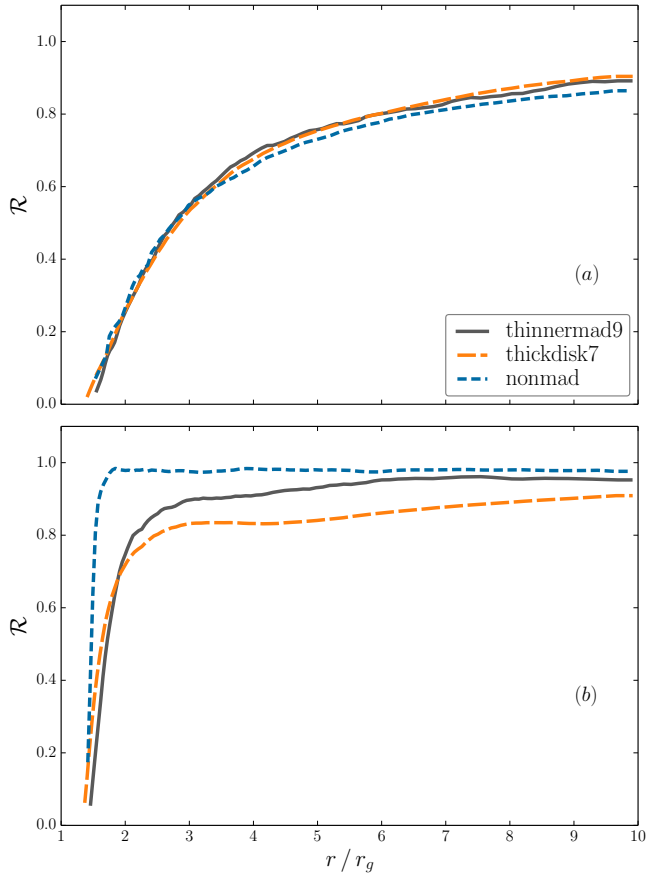

FIGURE B.5: Redshift profiles for different accretion models. The observer is located at (a) : $\theta = 0$, (b) : $\theta = \pi/2$. Although these models have different velocity fields, the resulting redshift profiles are similar. In particular, for $\theta = \pi/2$ the profiles are reasonably flat until close to the horizon. Therefore, the contributions from spin and viewing angle are more important than the model-dependent fluid velocity.

Appendix C

Dependence of the Spectra on the Black Hole Mass and on the Mass Accretion Rate

The GRMHD simulations are scale free, however, introducing radiation forces us to specify length, time, and mass/energy scales. The length and time scales are set by the black hole mass M. These are the gravitational radius $r_g = GM/c^2$, and light crossing time $t_g = r_g/c$. Since the fluid mass is $\ll M$, we set the mass/energy scale via the mass accretion rate

$$\dot{M} = \left| \int \mathrm{d}A \, \rho \, u^r \right| \tag{C.1}$$

where $\mathrm{d}A = \sqrt{-g} \, \mathrm{d}x^\theta \, \mathrm{d}x^\phi$, $g = \det(g_{\mu\nu})$ is the metric determinant, ρ is the mass density, and u^r is the radial component of the fluid four-velocity.

The synchrotron luminosity scales with the fluid properties as $L_{\mathrm{syn}} \sim \rho B^2 \Theta^2 V$, where B is the magnetic field strength, $\Theta = kT/mc^2$ is the electron temperature, and V is the volume of the emitting region. The mass density scales with the black hole mass and accretion rate as $\rho \sim \dot{M} t_g / V \sim \dot{M}/M^2$, where we have used that $t_g = r_g/c \sim M$ and $V \sim M^3$. The magnetic energy density scales in the same way. Since we are neglecting radiation pressure, the electron temperature is

simply proportional to the ratio of the internal and mass energy densities and so is independent of M and $\dot{M}$. Therefore, the luminosity scales as $L_{\rm syn} \sim \dot{M}^2/M$. It is convenient to write the accretion rate as a fraction η of the Eddington rate $\dot{M}_{\rm Edd}$. Since $\dot{M}_{\rm Edd}$ is proportional to the black hole mass, we find that $\rho \sim \eta/M$ and so $L_{\rm syn} \sim \eta^2 M$. We can follow the same procedure to find scalings for the synchrotron frequency $\nu_{\rm syn} \sim B\Theta^2 \sim \sqrt{\eta/M}$, the optical depth $\tau = n\sigma_T R \sim \eta$, and the Compton y parameter $y = 16\Theta^2\tau \sim \eta$ (Rybicki & Lightman, 1979). We conclude that the luminosities of the synchrotron and Compton spectral components depend strongly on the mass accretion rate as $L_{\rm syn} \sim \dot{M}^2$ and $L_{\rm Compton} = yL_{\rm syn} \sim \dot{M}^3$, while the frequencies of these components depend only weakly on $\dot{M}$ as $\nu_{\rm syn} \sim \dot{M}^{1/2}$ and $\nu_{\rm Compton} \sim \Theta^2\nu_{\rm syn} \sim \dot{M}^{1/2}$. Although we have neglected synchrotron self-absorption in these simple analytic scalings, we include this process in our numerical calculations of the spectra.

Appendix D

Mass and Internal Energy Densities in the GRMHD Models

In Figure D.1 we show (ϕ-averaged) snapshots of our MAD and SANE GRMHD models. The left panels show the mass density, and the right panels show the internal energy density. As in Figure 6.1, the top panel shows the thin-MAD model with $H/R \approx 0.2$ and $a = 0.99$, the middle panel shows the thick-MAD model with $H/R \approx 1$ and $a = 0.9375$, and the bottom panel shows the SANE model with $H/R \approx 0.2$ and $a = 0.92$. In these plots, the funnel regions have been filled with constant profiles of mass and internal energy according to the prescription described in section 6.3. The dashed lines represent the regions affected by the numerical floor material (prior to the manual filling of the funnel), which are removed in the "empty" funnel models. The jet in the thick-MAD model (middle panel) has a region near $r \approx 20\, r_g$ which is not affected by the numerical density floors. Instead, this is material which has moved from the disk into the funnel due to instabilities at the jet-disk interface (McKinney et al., 2012). This is a transient feature, which has little effect on the spectra in this case. However, such disk-jet instabilities are a possible physical mechanism for mass-loading the jet.

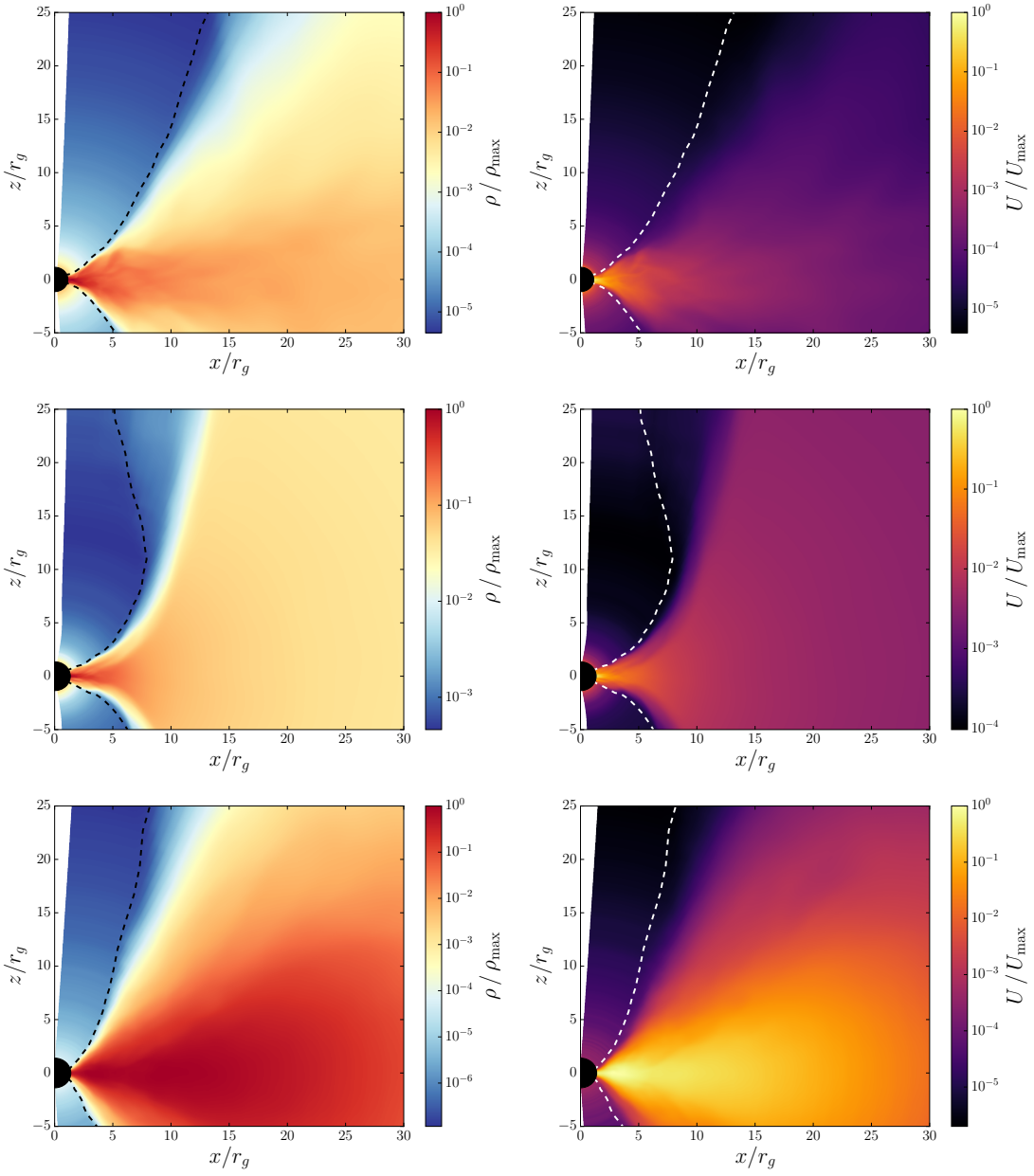

FIGURE D.1: Snapshots of our MAD and SANE GRMHD models. The left panels show the mass density, and the right panels show the internal energy density. The top panel shows the thin-MAD model with $H/R \approx 0.2$ and $a = 0.99$. The middle panel shows the thick-MAD model with $H/R \approx 1$ and $a = 0.9375$. The bottom panel shows the SANE model with $H/R \approx 0.2$ and $a = 0.92$. The funnel regions are manually filled with constant profiles of mass and internal energy densities, according to the prescription described in section 6.3. The dashed lines represent the region which is removed in the "empty" funnel models. In the text, we refer to the surface represented by the dashed lines as the "edge" of the funnel wall.

Bibliography

Abbott, B. P. et al. 2017a, Phys. Rev. Lett., 119, 161101, 1710.05832

——. 2017b, ApJL, 848, L12, 1710.05833

Abdo, A. A., Ackermann, M., Ajello, M., et al. 2010, ApJ, 722, 520, 1004.0348

Abramowicz, M. A., Chen, X., Kato, S., Lasota, J.-P., & Regev, O. 1995, ApJL, 438, L37, astro-ph/9409018

Ackermann, M., Anantua, R., Asano, K., et al. 2016, ApJL, 824, L20, 1605.05324

Aharonian, F., Akhperjanian, A. G., Bazer-Bachi, A. R., et al. 2007, ApJL, 664, L71, 0706.0797

Aharonian, F. A. 2000, NewA, 5, 377, arXiv:astro-ph/0003159

Albert, J., Aliu, E., Anderhub, H., et al. 2007, ApJ, 669, 862, arXiv:astro-ph/0702008

Aleksić, J., Antonelli, L. A., Antoranz, P., et al. 2011, ApJL, 730, L8, 1101.4645

Avara, M. J., McKinney, J. C., & Reynolds, C. S. 2016, MNRAS, 462, 636, 1508.05323

Baganoff, F. K., Maeda, Y., Morris, M., & et. al. 2003, ApJ, 591, 891, astro-ph/0102151

Ball, D., Özel, F., Psaltis, D., & Chan, C.-k. 2016, ApJ, 826, 77, 1602.05968

Bardeen, J. M., Press, W. H., & Teukolsky, S. A. 1972, ApJ, 178, 347

Barkov, M. V., Aharonian, F. A., Bogovalov, S. V., Kelner, S. R., & Khangulyan, D. 2012, ApJ, 749, 119, 1012.1787

Barniol Duran, R., Tchekhovskoy, A., & Giannios, D. 2017, MNRAS, 469, 4957, 1612.06929

Belloni, T., Homan, J., Casella, P., van der Klis, M., Nespoli, E., Lewin, W. H. G., Miller, J. M., & Méndez, M. 2005, A&A, 440, 207, astro-ph/0504577

Bettoni, D., Falomo, R., Fasano, G., & Govoni, F. 2003, A&A, 399, 869, astro-ph/0212162

Blandford, R. D., & Konigl, A. 1979, ApJ, 232, 34

Blandford, R. D., & Payne, D. G. 1982, MNRAS, 199, 883

Blandford, R. D., & Znajek, R. L. 1977, MNRAS, 179, 433

Bosch-Ramon, V., Aharonian, F. A., & Paredes, J. M. 2005, A&A, 432, 609, astro-ph/0411508

Bosch-Ramon, V., Romero, G. E., & Paredes, J. M. 2006, A&A, 447, 263, arXiv:astro-ph/0509086

Böttcher, M. 2010, ArXiv e-prints, 1006.5048

Böttcher, M., Reimer, A., Sweeney, K., & Prakash, A. 2013, ApJ, 768, 54, 1304.0605

Boyer, R. H., & Lindquist, R. W. 1967, Journal of Mathematical Physics, 8, 265

Broderick, A. E., Johannsen, T., Loeb, A., & Psaltis, D. 2014, ApJ, 784, 7, 1311.5564

Broderick, A. E., & Tchekhovskoy, A. 2015, ApJ, 809, 97, 1506.04754

Cadolle Bel, M., Sizun, P., Goldwurm, A., Rodriguez, J., et al. 2006, A&A, 446, 591, arXiv:astro-ph/0509851

Carroll, S. M. 2004, Spacetime and geometry. An introduction to general relativity

Chan, C.-k., Liu, S., Fryer, C. L., Psaltis, D., Özel, F., Rockefeller, G., & Melia, F. 2009, ApJ, 701, 521

Chan, C.-k., Psaltis, D., & Özel, F. 2013, ApJ, 777, 13, 1303.5057

Chan, C.-k., Psaltis, D., Özel, F., Medeiros, L., Marrone, D., Saḍowski, A., & Narayan, R. 2015a, ApJ, 812, 103, 1505.01500

Chan, C.-K., Psaltis, D., Özel, F., Narayan, R., & Saḍowski, A. 2015b, ApJ, 799, 1, 1410.3492

Corbel, S. 2011, in IAU Symposium, Vol. 275, Jets at All Scales, ed. G. E. Romero, R. A. Sunyaev, & T. Belloni, 205–214

Corbel, S., Fender, R. P., Tzioumis, A. K., Nowak, M., McIntyre, V., Durouchoux, P., & Sood, R. 2000, A&A, 359, 251, arXiv:astro-ph/0003460

Corbel, S., Nowak, M. A., Fender, R. P., Tzioumis, A. K., & Markoff, S. 2003, A&A, 400, 1007, arXiv:astro-ph/0301436

Cowling, T. G. 1933, MNRAS, 94, 39

Cunningham, C. T., & Bardeen, J. M. 1972, ApJL, 173, L137

——. 1973, ApJ, 183, 237

Dexter, J., McKinney, J. C., & Agol, E. 2012, MNRAS, 421, 1517, 1109.6011

Dexter, J., McKinney, J. C., Markoff, S., & Tchekhovskoy, A. 2014, MNRAS, 440, 2185, 1312.1691

Dibi, S., Drappeau, S., Fragile, P. C., Markoff, S., & Dexter, J. 2012, MNRAS, 426, 1928

Doeleman, S., Agol, E., Backer, D., Baganoff, F., & et. al. 2009a, in ArXiv Astrophysics e-prints, Vol. 2010, astro2010: The Astronomy and Astrophysics Decadal Survey, 0906.3899

Doeleman, S. S., Fish, V. L., Broderick, A. E., Loeb, A., & Rogers, A. E. E. 2009b, ApJ, 695, 59, 0809.3424

Doeleman, S. S., Weintroub, J., Rogers, A. E. E., & et. al. 2008, Nature, 455, 78, 0809.2442

Dolence, J. C., Gammie, C. F., Mościbrodzka, M., & Leung, P. K. 2009, ApJS, 184, 387

Dondi, L., & Ghisellini, G. 1995, MNRAS, 273, 583

Esin, A. A., McClintock, J. E., Drake, J. J., Garcia, M. R., Haswell, C. A., Hynes, R. I., & Muno, M. P. 2001, ApJ, 555, 483, arXiv:astro-ph/0103044

Esin, A. A., McClintock, J. E., & Narayan, R. 1997, ApJ, 489, 865, arXiv:astro-ph/9705237

Etienne, Z. B., Paschalidis, V., Haas, R., Mösta, P., & Shapiro, S. L. 2015, Classical and Quantum Gravity, 32, 175009, 1501.07276

Falcke, H., Körding, E., & Markoff, S. 2004, A&A, 414, 895, arXiv:astro-ph/0305335

Fanton, C., Calvani, M., de Felice, F., & Cadez, A. 1997, PASJ, 49, 159

Fender, R. 2010, in Lecture Notes in Physics, Berlin Springer Verlag, Vol. 794, Lecture Notes in Physics, Berlin Springer Verlag, ed. T. Belloni, 115, 0909.2572

Fender, R., & Gallo, E. 2014, SSRv, 183, 323, 1407.3674

Fender, R. P., Belloni, T. M., & Gallo, E. 2004, MNRAS, 355, 1105, arXiv:astro-ph/0409360

Fender, R. P., Gallo, E., & Russell, D. 2010, MNRAS, 406, 1425, 1003.5516

Fishbone, L. G., & Moncrief, V. 1976, ApJ, 207, 962

Fossati, G., Maraschi, L., Celotti, A., Comastri, A., & Ghisellini, G. 1998, MNRAS, 299, 433, arXiv:astro-ph/9804103

Foucart, F., Chandra, M., Gammie, C. F., & Quataert, E. 2016, MNRAS, 456, 1332, 1511.04445

Gallo, E., Fender, R. P., & Pooley, G. G. 2003, MNRAS, 344, 60, arXiv:astro-ph/0305231

Gammie, C. F., McKinney, J. C., & Tóth, G. 2003, ApJ, 589, 444, arXiv:astro-ph/0301509

Ghisellini, G., Righi, C., Costamante, L., & Tavecchio, F. 2017, MNRAS, 469, 255, 1702.02571

Giacomazzo, B., & Rezzolla, L. 2007, Classical and Quantum Gravity, 24, 235, gr-qc/0701109

Giannios, D., Uzdensky, D. A., & Begelman, M. C. 2009, MNRAS, 395, L29, 0901.1877

Gierlinski, M., Zdziarski, A. A., Done, C., Johnson, W. N., Ebisawa, K., Ueda, Y., Haardt, F., & Phlips, B. F. 1997, MNRAS, 288, 958, arXiv:astro-ph/9610156

Gillessen, S., Eisenhauer, F., Trippe, S., Alexander, T., Genzel, R., Martins, F., & Ott, T. 2009, ApJ, 692, 1075, 0810.4674

Globus, N., & Levinson, A. 2013, PhRvD, 88, 084046, 1310.0360

Gold, R., McKinney, J. C., Johnson, M. D., & Doeleman, S. S. 2017, ApJ, 837, 180, 1601.05550

Goyal, A. et al. 2017, ApJ, 837, 127, 1702.02504

Gupta, S., Böttcher, M., & Dermer, C. D. 2006, ApJ, 644, 409, arXiv:astro-ph/0602439

Igumenshchev, I. V. 2009, ApJL, 702, L72, 0908.0431

Jackson, J. D. 1975, Classical Electrodynamics (New York: Wiley)

Jones, E., Oliphant, T., Peterson, P., et al. 2001, SciPy: Open source scientific tools for Python

Kaiser, C. R. 2006, MNRAS, 367, 1083, arXiv:astro-ph/0601103

Kylafis, N. D., Papadakis, I. E., Reig, P., Giannios, D., & Pooley, G. G. 2008, A&A, 489, 481, 0807.2910

Landau, L. D., & Lifshitz, E. M. 1959, Fluid Mechanics, Vol. 6 (New York: Pergamon)

Landau, L. D., & Lifshitz, E. M. 1975, The classical theory of fields

Lang, K. R. 1980, Astrophysical Formulae. A Compendium for the Physicist and Astrophysicist. (Springer-Verlag Berlin Heidelberg New York), 46

Lasota, J.-P., Gourgoulhon, E., Abramowicz, M., Tchekhovskoy, A., & Narayan, R. 2014, PhRvD, 89, 024041, 1310.7499

Leung, P. K., Gammie, C. F., & Noble, S. C. 2011, ApJ, 737, 21

Levermore, C. D. 1984, JQSRT, 31, 149

Levinson, A., & Rieger, F. 2011, ApJ, 730, 123, 1011.5319

Livio, M., Ogilvie, G. I., & Pringle, J. E. 1999, ApJ, 512, 100, arXiv:astro-ph/9809093

MacDonald, D., & Thorne, K. S. 1982, MNRAS, 198, 345

Madejski, G., & Sikora, M. 2016, ARA&A, 54, 725

Magdziarz, P., & Zdziarski, A. A. 1995, MNRAS, 273, 837

Maitra, D., Markoff, S., Brocksopp, C., Noble, M., Nowak, M., & Wilms, J. 2009, MNRAS, 398, 1638, 0904.2128

Mannheim, K., & Biermann, P. L. 1992, A&A, 253, L21

Markoff, S., Falcke, H., & Fender, R. 2001, A&A, 372, L25, arXiv:astro-ph/0010560

Markoff, S., Nowak, M., Corbel, S., Fender, R., & Falcke, H. 2003, A&A, 397, 645, arXiv:astro-ph/0210439

Markoff, S., Nowak, M. A., Gallo, E., et al. 2015, ApJL, 812, L25, 1510.02244

Markoff, S., Nowak, M. A., & Wilms, J. 2005, ApJ, 635, 1203, arXiv:astro-ph/0509028

Max-Moerbeck, W., Hovatta, T., Richards, J. L., et al. 2014, MNRAS, 445, 428, 1408.6264

McClintock, J. E., Narayan, R., Davis, S. W., et al. 2011, Classical and Quantum Gravity, 28, 114009

McKinney, J. C. 2004, PhD thesis, University of Illinois at Urbana-Champaign

——. 2006, MNRAS, 368, 1561, arXiv:astro-ph/0603045

McKinney, J. C., & Blandford, R. D. 2009, MNRAS, 394, L126, 0812.1060

McKinney, J. C., Dai, L., & Avara, M. J. 2015, MNRAS, 454, L6, 1508.02433

McKinney, J. C., & Gammie, C. F. 2004, ApJ, 611, 977, arXiv:astro-ph/0404512

McKinney, J. C., Tchekhovskoy, A., & Blandford, R. D. 2012, MNRAS, 423, 3083, 1201.4163

——. 2013, Science, 339, 49, 1211.3651

McKinney, J. C., Tchekhovskoy, A., Sadowski, A., & Narayan, R. 2014, MNRAS, 441, 3177

Meier, D. L. 2001, ApJL, 548, L9, arXiv:astro-ph/0010231

Merloni, A., Heinz, S., & di Matteo, T. 2003, MNRAS, 345, 1057, arXiv:astro-ph/0305261

Mihalas, D., & Mihalas, B. W. 1984, Foundations of radiation hydrodynamics

Mirabel, I. F., & Rodríguez, L. F. 1994, Nature, 371, 46

Mościbrodzka, M., & Falcke, H. 2013, A&A, 559, L3

Mościbrodzka, M., Falcke, H., & Shiokawa, H. 2016, A&A, 586, A38, 1510.07243

Mościbrodzka, M., Falcke, H., Shiokawa, H., & Gammie, C. F. 2014, A&A, 570, A7

Mościbrodzka, M., Gammie, C. F., Dolence, J. C., & Shiokawa, H. 2011, ApJ, 735, 9, 1104.2042

Mościbrodzka, M., Gammie, C. F., Dolence, J. C., Shiokawa, H., & Leung, P. K. 2009, ApJ, 706, 497

Mücke, A., & Protheroe, R. J. 2001, Astroparticle Physics, 15, 121, astro-ph/0004052

Mücke, A., Protheroe, R. J., Engel, R., Rachen, J. P., & Stanev, T. 2003, Astroparticle Physics, 18, 593, arXiv:astro-ph/0206164

Narayan, R., Igumenshchev, I. V., & Abramowicz, M. A. 2003, PASJ, 55, L69, astro-ph/0305029

Narayan, R., & McClintock, J. E. 2008, NewAR, 51, 733, 0803.0322

——. 2012, MNRAS, 419, L69, 1112.0569

Narayan, R., & Piran, T. 2012, MNRAS, 420, 604, 1107.5812

Narayan, R., Sadowski, A., Penna, R. F., & Kulkarni, A. K. 2012, MNRAS, 426, 3241, 1206.1213

Narayan, R., Sadowski, A., & Soria, R. 2017, MNRAS, 469, 2997, 1702.01158

Narayan, R., & Yi, I. 1994, ApJL, 428, L13, astro-ph/9403052

——. 1995a, ApJ, 444, 231, astro-ph/9411058

——. 1995b, ApJ, 452, 710, astro-ph/9411059

Narayan, R., Zhu, Y., Psaltis, D., & Saḍowski, A. 2016, MNRAS, 457, 608, 1510.04208

Neilsen, J., Nowak, M. A., Gammie, C., & et. al. 2013, ApJ, 774, 42, 1307.5843

Niedźwiecki, A., Xie, F.-G., & Stępnik, A. 2014, MNRAS, 443, 1733, 1406.6003

Niedźwiecki, A., Xie, F.-G., & Zdziarski, A. A. 2012, MNRAS, 420, 1195, 1107.0860

Noble, S. C., Krolik, J. H., & Hawley, J. F. 2009, ApJ, 692, 411, 0808.3140

Novikov, I. D., & Thorne, K. S. 1973, in Black Holes (Les Astres Occlus), ed. C. Dewitt & B. S. Dewitt (New York: Gordon & Breach), 343–450

O' Riordan, M., Pe'er, A., & McKinney, J. C. 2016a, ApJ, 819, 95, 1510.08860

——. 2016b, ApJ, 831, 62, 1607.01060

——. 2017, ApJ, 843, 81, 1704.05882

——. 2018, ApJ, 853, 44, 1711.04691

Özel, F., Psaltis, D., & Narayan, R. 2000, ApJ, 541, 234, astro-ph/0004195

Pe'er, A., & Casella, P. 2009, ApJ, 699, 1919, 0902.2892

Pe'er, A., & Markoff, S. 2012, ApJ, 753, 177, 1105.4896

Penrose, R. 1969, Nuovo Cimento Rivista Serie, 1

Poisson, E. 2004, A relativist's toolkit : the mathematics of black-hole mechanics

Poutanen, J. 1998, in Theory of Black Hole Accretion Disks, ed. M. A. Abramowicz, G. Bjornsson, & J. E. Pringle (Cambridge University Press), 100–122, arXiv:astro-ph/9805025

Press, W. H., Flannery, B. P., Teukolsky, S. A., & Vetterling, W. T. 1986, Numerical Recipes: The art of scientific computing (Cambridge: Cambridge University Press)

Psaltis, D., Özel, F., Chan, C.-K., & Marrone, D. P. 2015, ApJ, 814, 115, 1411.1454

Qiao, E., & Liu, B. F. 2015, MNRAS, 448, 1099, 1501.03565

Ramakrishnan, V., Hovatta, T., Nieppola, E., Tornikoski, M., Lähteenmäki, A., & Valtaoja, E. 2015, MNRAS, 452, 1280, 1507.04287

Remillard, R. A., & McClintock, J. E. 2006, ARA&A, 44, 49, arXiv:astro-ph/0606352

Ressler, S. M., Tchekhovskoy, A., Quataert, E., Chandra, M., & Gammie, C. F. 2015, MNRAS, 454, 1848, 1509.04717

Ressler, S. M., Tchekhovskoy, A., Quataert, E., & Gammie, C. F. 2017, MNRAS, 467, 3604, 1611.09365

Romero, G. E., Boettcher, M., Markoff, S., & Tavecchio, F. 2017, SSRv, 207, 5, 1611.09507

Romero, G. E., Torres, D. F., Kaufman Bernadó, M. M., & Mirabel, I. F. 2003, A&A, 410, L1, astro-ph/0309123

Russell, D. M., Russell, T. D., Miller-Jones, J. C. A., et al. 2013, ApJL, 768, L35, 1304.3510

Ryan, B. R., Dolence, J. C., & Gammie, C. F. 2015, ApJ, 807, 31, 1505.05119

Ryan, B. R., Ressler, S. M., Dolence, J. C., Tchekhovskoy, A., Gammie, C., & Quataert, E. 2017, ApJL, 844, L24, 1707.04238

Rybicki, G. B., & Lightman, A. P. 1979, Radiative Processes in Astrophysics (New York, Wiley-Interscience)

Sądowski, A., & Gaspari, M. 2017, MNRAS, 468, 1398, 1701.07033

Sądowski, A., & Narayan, R. 2015, MNRAS, 453, 3213, 1503.00654

Sądowski, A., Narayan, R., Tchekhovskoy, A., Abarca, D., Zhu, Y., & McKinney, J. C. 2015, MNRAS, 447, 49, 1407.4421

Sądowski, A., Narayan, R., Tchekhovskoy, A., & Zhu, Y. 2013, MNRAS, 429, 3533, 1212.5050

Sądowski, A., Wielgus, M., Narayan, R., Abarca, D., McKinney, J. C., & Chael, A. 2017, MNRAS, 466, 705, 1605.03184

Shakura, N. I., & Sunyaev, R. A. 1973, A&A, 24, 337

Shcherbakov, R. V., & Huang, L. 2011, MNRAS, 410, 1052, 1007.4831

Shcherbakov, R. V., & McKinney, J. C. 2013, ApJL, 774, L22

Shcherbakov, R. V., Penna, R. F., & McKinney, J. C. 2012, ApJ, 755, 133, 1007.4832

Sironi, L., Keshet, U., & Lemoine, M. 2015, SSRv, 191, 519, 1506.02034

Sironi, L., & Spitkovsky, A. 2014, ApJL, 783, L21, 1401.5471

Tchekhovskoy, A., & Bromberg, O. 2016, MNRAS, 461, L46, 1512.04526

Tchekhovskoy, A., & McKinney, J. C. 2012, MNRAS, 423, L55, 1201.4385

Tchekhovskoy, A., McKinney, J. C., & Narayan, R. 2012, Journal of Physics Conference Series, 372, 012040, 1202.2864

Tchekhovskoy, A., Narayan, R., & McKinney, J. C. 2010, ApJ, 711, 50, 0911.2228

——. 2011, MNRAS, 418, L79, 1108.0412

Titarchuk, L. 1994, ApJ, 434, 570

Ulrich, M.-H., Maraschi, L., & Urry, C. M. 1997, ARA&A, 35, 445

Urry, C. M., & Padovani, P. 1995, PASP, 107, 803, arXiv:astro-ph/9506063

Wellons, S., Zhu, Y., Psaltis, D., Narayan, R., & McClintock, J. E. 2014, ApJ, 785, 142, 1312.3333

White, C. J., Stone, J. M., & Gammie, C. F. 2016, ApJS, 225, 22, 1511.00943

Yuan, F., & Narayan, R. 2014, ARA&A, 52, 529, 1401.0586

Yuan, F., Zdziarski, A. A., Xue, Y., & Wu, X.-B. 2007, ApJ, 659, 541, arXiv:astro-ph/0608552

Zhu, Y., Narayan, R., Sadowski, A., & Psaltis, D. 2015, MNRAS, 451, 1661, 1505.04838